8-2012

Characterization of Wetting Front Geometry and Fluid Migration in the Vadose Zone Using Surface Time-Lapse Seismic First-Arrival Tomography

Rachel Elizabeth Storniolo
rstornio@utk.edu

To the Graduate Council:

I am submitting herewith a thesis written by Rachel Elizabeth Storniolo entitled "Characterization of Wetting Front Geometry and Fluid Migration in the Vadose Zone Using Surface Time-Lapse Seismic First-Arrival Tomography." I have examined the final electronic copy of this thesis for form and content and recommend that it be accepted in partial fulfillment of the requirements for the degree of Master of Science, with a major in Geology.

Gregory S. Baker, Major Professor

We have read this thesis and recommend its acceptance:

Ed Perfect, Jaehoon Lee

Accepted for the Council:
Carolyn R. Hodges

Vice Provost and Dean of the Graduate School

(Original signatures are on file with official student records.)

To the Graduate Council:

I am submitting herewith a thesis written by Rachel Elizabeth Storniolo entitled "Characterization of Wetting Bulb Geometry and Fluid Migration in the Vadose Zone Using Surface Time-Lapse Seismic First-Arrival Tomography" I have examined the electronic copy of this thesis for form and content and recommend that it be accepted in partial fulfillment of the requirements for the degree of Master of Science, with a major in Geology.

_____
Gregory S. Baker
Major Professor

We have read this thesis and recommend
its acceptance:

_____
Ed Perfect

_____
Jaehoon Lee

Accepted for the Council:

_____
Carolyn R. Hodges
Vice Provost and Dean
of the Graduate School

Characterization of Wetting Front Geometry and Fluid Migration in the Vadose Zone Using Surface Time-Lapse Seismic First-Arrival Tomography

A Thesis Presented for the
Master of Science
Degree
The University of Tennessee, Knoxville

Rachel Elizabeth Storniolo
August 2012

DEDICATION

In dedication to my family and friends, without their support and motivation throughout my academic pursuits, I could not have accomplished what I have today. To my mother in particular who has always been there for me, encouraging me to follow my dreams and ambitions. Additionally, my undergraduate advisor and mentor at Appalachian State University, William P. Anderson, who is responsible for capturing my interest in geology and pushing me to pursue a graduate degree. To you all…. thank you for your motivation, support, and generosity.

ACKNOWLEDGEMENTS

I would like to acknowledge my advisor Gregory S. Baker for giving me the boundless opportunities to explore geophysics. I am so thankful for the knowledge and experiences I have gained in the past two years that are unavailable to most graduate students. Furthermore, my committee members Ed Perfect and Jaehoon Lee who were not only incredible instructors but kind and generous committee members, that devoted their valuable time and insight into my project. I would also like to acknowledge Oak Ridge National Laboratory for funding my research assistantship at the University of Tennessee and the opportunity to be involved with several unique research projects, many of which were in conjunction with Lawrence Berkeley National Laboratory and the brilliant scientists working for them.

ABSTRACT

Characterizing and quantifying vadose zone parameters and processes are critical for assessing environmental, agricultural, and engineering problems. The shallow subsurface is essential to the geologic and hydrologic cycles because it supports agriculture and ecosystems, influences water resources, and acts as a repository for contaminants. Fluid migration in the vadose zone is dependent on a number of soil characteristics (e.g. soil type and saturation). Quantifying parameters is often the primary goal of hydrological fluid-flow investigations; however, the values calculated can be misrepresentative of the subsurface due to anisotropic features. Hydraulic conductivity (K), the most common quantitative parameter used to describe fluid flow through a porous medium, is complicated in the vadose zone due to spatial and temporal variations at many scales. Many *in-situ* methods for calculating K (i.e. constant head permeameter method) use surface measurements to quantify subsurface fluid flow. However, the geometry and distribution of the fluid migrating through the subsurface is not determinable from surface measurements, and therefore these techniques may not provide a comprehensive understanding of field-scale fluid flow. In this study, a more robust non-invasive method to image a migrating wetting front in the vadose zone is developed using time-lapse seismic first-arrival tomography (TLSFT). The TLSFT method is based on the concept that variations in seismic compressional wave (*P*-wave) arrival times are used as a proxy for the relative saturation changes due to an advancing wetting front generated from surface infiltration. Two constant flux

applicator infiltration experiments were conducted at the East Tennessee Research and Education Center B-4 plot, while simultaneously collecting TLSFT data to image a migrating wetting front. The TLSFT infiltration method successfully images a migrating wetting front through the vadose zone at different time steps to visually characterize the geometry and distribution of water. Calculated K values using TLSFT infiltration data with an empirical formula are within one to two orders of magnitude of calculated K from an Amoozemeter experiment and known K of the Sequatchie soil series at the B-4 plot. TLSFT calculated ranges of K values are reasonable when considering the spatial and temporal extent of K at a single site.

TABLE OF CONTENTS

Section Page

LIST OF TABLES

Table Page

LIST OF FIGURES

Figure Page

1. INTRODUCTION

1.1. Motivation

Near-surface problems are generally investigated by hydrogeologists, soil scientists, agronomists, and engineers who attempt to quantify, characterize, or monitor subsurface materials and/or processes. Environmental problems can include modeling and predicting contaminant flow and transport from a buried tank. An engineering problem could include determining the material properties necessary to design a liner for waste ponds in order to minimize the seepage into the surrounding materials.

Understanding and characterizing vadose zone hydrology is not only important for a variety of scientific disciplines and engineering applications, the vadose zone also influences the infiltration of surface water to ground water which is the primary source of drinking water for millions of people throughout the world. However, estimating parameters in the vadose zone is difficult due to the heterogeneous and anisotropic nature of the subsurface. Additionally, many variables that influence vadose zone parameters are time-dependent and require installation of sensors to monitor temporal variations to more accurately define subsurface processes. Most fluid parameters in the vadose zone are dependent on water content and/or tension. Unfortunately, water content and tension are highly variable both spatially and temporally. In field-scale applications, estimating these variables require extensive sensor installation or collection of data at the surface. Soils in the vadose zone can range from unsaturated to variably saturated

depending on a variety of factors (i.e. grain size distribution, shape, degree of pore size connectedness, etc.), and it is often difficult or unrealistic to obtain accurate measurements at the field scale.

Often, quantifications of fluid flow in the vadose zone are obtained by in-situ surface infiltration measurements (e.g. ring infiltrometer and constant head permeameter) that are unable to evaluate the geometric distribution of water as it migrates through the subsurface. Infiltration from the surface generates a wetting front that is generally in the shape of an ellipse or sphere when subsurface materials are relatively homogeneous and isotropic. As infiltration into the subsurface continues with time, we know the soil is accommodating the volume of water; however, the geometry in unknown unless one is able to image the subsurface (Figure 1). The geometric distribution of a wetting front (i.e. how the soil spatially accommodates infiltrated water) is critical and can describe anisotropic and heterogeneous conditions in the subsurface (e.g. fracture networks or animal burrows) that may generate significant errors in groundwater models if unaccounted for in parameterization.

1.2. Objective

The objective of the project is to first develop an *in-situ* method to image the migration of a wetting front generated from surface infiltration using time-lapse seismic first-arrival tomography (TLSFT). The second objective of the project is to

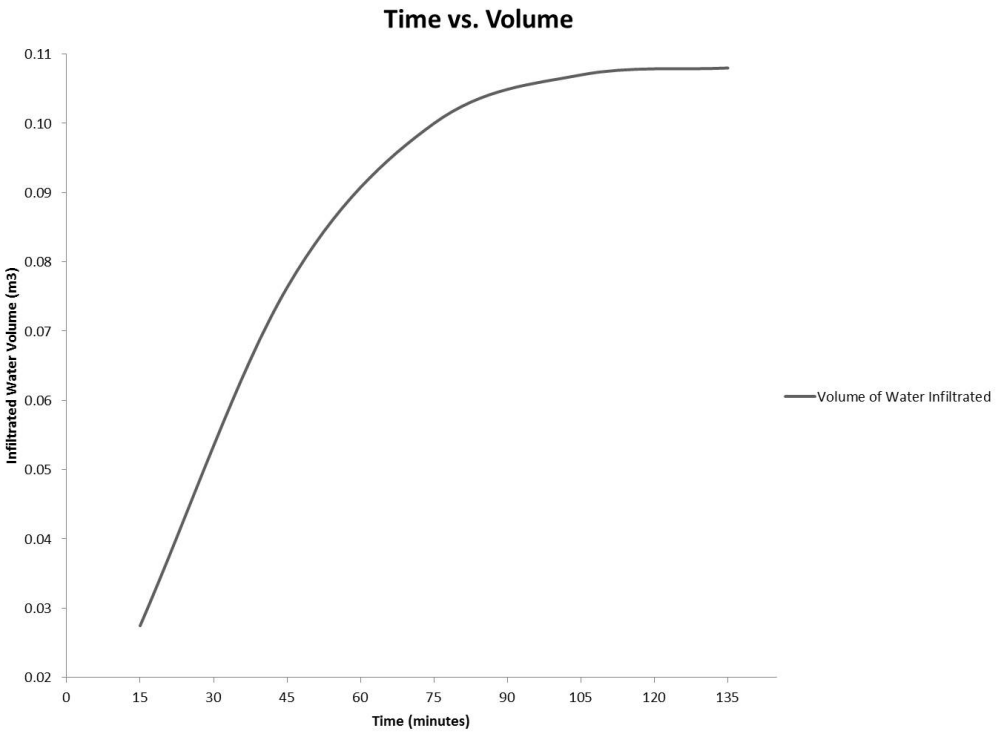

Figure 1: Graph showing water infiltration with time.

calculate the rate of fluid migration using TLSFT for a quantitative comparison of the TLSFT method to *in-situ* surface methods that are commonly used for quantifying fluid flow parameters in the vadose zone (i.e. hydraulic conductivity). Ideally, the proposed method can provide a visual characterization of wetting front geometry and distribution which will be used to infer information regarding anisotropy and presence of soil structure in the vadose zone. Secondly, we use wetting front geometry obtained by TLSFT to calculate hydraulic conductivity, which is a common parameter used in the vadose zone to quantify the rate and movement of water through a porous media. The objective for calculating values of hydraulic conductivity is to quantitatively compare the TLSFT method with standard methods used to investigate fluid flow in the vadose zone.

1.3. Overview of Experimental Design

The first experiment used a constant flux applicator to infiltrate water into the vadose zone in order to generate a wetting front. A series of surface seismic data was acquired at different time intervals during infiltration to image the migration of the wetting front both spatially and temporally. The infiltration experiment was first conducted in the fall of 2010 for proof of method, which was to determine whether time-lapse seismic first-arrival tomography could resolve the migrating wetting front by using *P*-wave velocities as a proxy for relative saturation changes in the area of infiltration. Furthermore, we investigate the use of TLSFT to produce an isolated image of the wetting front at different time-steps throughout

infiltration to provide a visual characterization of the wetting front geometry and distribution of infiltrated water. In the summer of 2012, an experiment was conducted to reproduce TLSFT profiles of a wetting front from surface infiltration and to calculate hydraulic conductivity from the TLSFT profiles for quantitative comparison of the TLSFT method to common methods used for characterization and quantification of fluid movement in the vadose zone. A compact constant head permeameter (Amoozemeter) infiltration experiment was conducted in the summer of 2012 to obtain calculations of hydraulic conductivity, which are used for comparison to the TLSFT method.

The two infiltration experiments using a constant flux applicator were conducted simultaneously with the collection of surface time-lapse seismic first-arrival data. Seismic velocity variations observed in tomographic *P*-wave velocity models were used as a proxy for the relative changes in water saturation, as water was infiltrated from the surface into a partially saturated porous soil. As the ellipsoidal wetting front advanced, a series of time-lapse seismic profiles were collected to observe the velocity perturbations in the area of infiltration. The TLSFT profiles are used to visually characterize the geometry and distribution of the wetting front. Using the TLSFT profiles obtained during the second constant flux applicator experiment, hydraulic conductivity values were calculated using an empirical formula (Schwartzman and Zur, 1987), measured field parameters (i.e. outflow rate and infiltrated water volume), and the geometry of the velocity perturbation (i.e. wetting front).

The first *in-situ* infiltration experiment was conducted using a constant flux applicator with a relatively controlled rate of water discharged into the subsurface. The constant flux applicator apparatus contained a valve to constrict the outflow rate of water. The valve on the apparatus was positioned such that the outflow rate was at its slowest. Details of water volume in the constant flux applicator reservoir, as well as small changes in outflow rate were not recorded throughout the experiment. The initial infiltration experiment produced five profiles at different time-steps during infiltration imaging the migration of a wetting front with time.

The second *in-situ* infiltration experiment also used a constant flux applicator for infiltration; however, during the second experiment, volume and discharge rates were monitored and recorded to calculate hydraulic conductivity at five time-steps throughout the infiltration experiment. Additionally, a compact constant head permeameter (CCHP), called an Amoozemeter, was used in and employed at the field site to obtain hydraulic conductivity calculations. The Amoozemeter instrument uses the constant head permeameter method, and is a field instrument designed for calculating saturated hydraulic conductivity *in-situ.* The hydraulic conductivity calculations from the Amoozemeter were obtained to quantitatively compare the TLSFT method to a standard method used for characterizing fluid flow in the vadose zone.

The Amoozemeter is a common field method used to estimate K_s, and a suitable method for comparing the calculations generated using our TLSFT method. The primary objective of the TLSFT method is the visual characterization of wetting

front geometry and distribution of infiltrated volume. The calculations of hydraulic conductivity using Schwartzman and Zur (1987) were investigated in order to quantitatively compare the proposed TLSFT method to existing methods commonly used to investigate fluid flow in the vadose zone. The newly developed method will provide an improved understanding of subsurface fluid migration in the presence of heterogeneities and anisotropic features, where current *in-situ* surface infiltration methods (e.g. Amoozemeter) fail to provide.

2. BACKGROUND

2.1. Study Area

The study area is located in Knox County in the Valley and Ridge physiographic province of East Tennessee along an alluvial terrace of the Tennessee River, locally known as Loudoun Reservoir (Figure 2). The Valley and Ridge province is comprised of ridges trending northeast and southwest with valleys separating them.

The field site is located at one of The University of Tennessee's Agriculture Experiment Stations known as East Tennessee Research and Education Center (ETREC) at the B-4 plot (Figure 3). The ETREC is located approximately two miles south of the main campus of The University of Tennessee in Knoxville, TN off of Alcoa Highway. The experiments were all conducted at the B-4 plot at the ETREC. The B-4 plot is situated on the t-1 alluvial terrace of the Tennessee River. An alluvial terrace is created as a river ages and erodes into the landscape, where the youngest alluvial terrace (t-1) can be within a few meters from the local water table. Additionally, the B-4 plot is used for undergraduate and graduate courses in geology and hydrology through the University of Tennessee, as well as the TINGS (Tennessee Intensive Near-Surface Geophysics Study) course offered selectively in the summer mini-term session.

The Tennessee River Quaternary alluvial terrace deposits generally exhibit coarse gravel materials at depth and display a grading upward to finer textured sands and silts (Roberts, 1955). The site contains soil from the Sequatchie series,

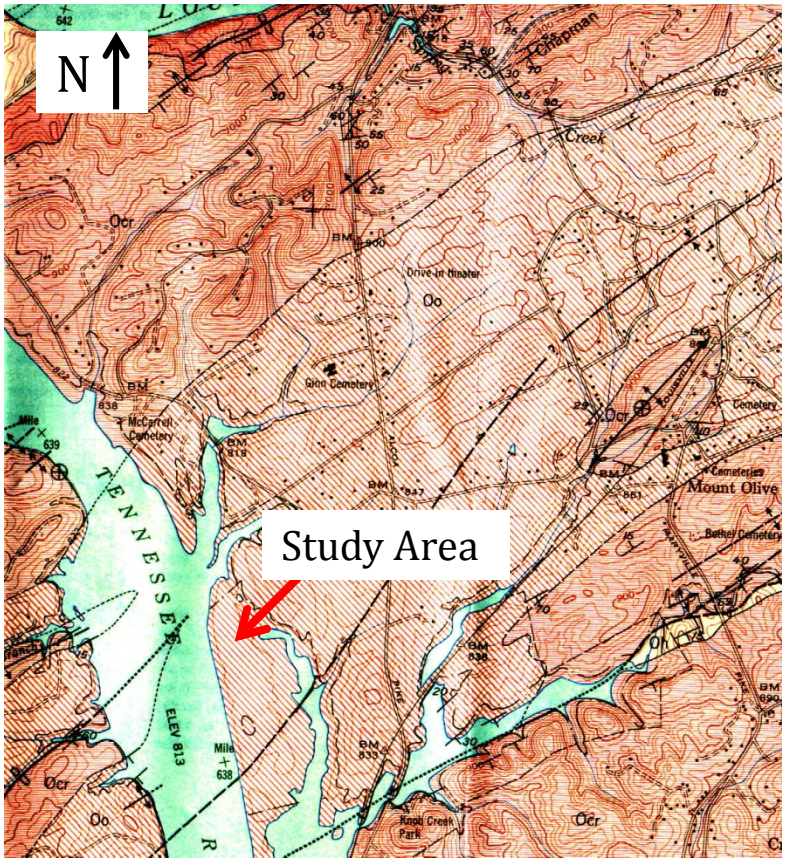

Figure 2: USGS Geologic Map of the Knoxville Quadrangle (Cattermole, 1958) showing the general area of the ETREC plot B-4

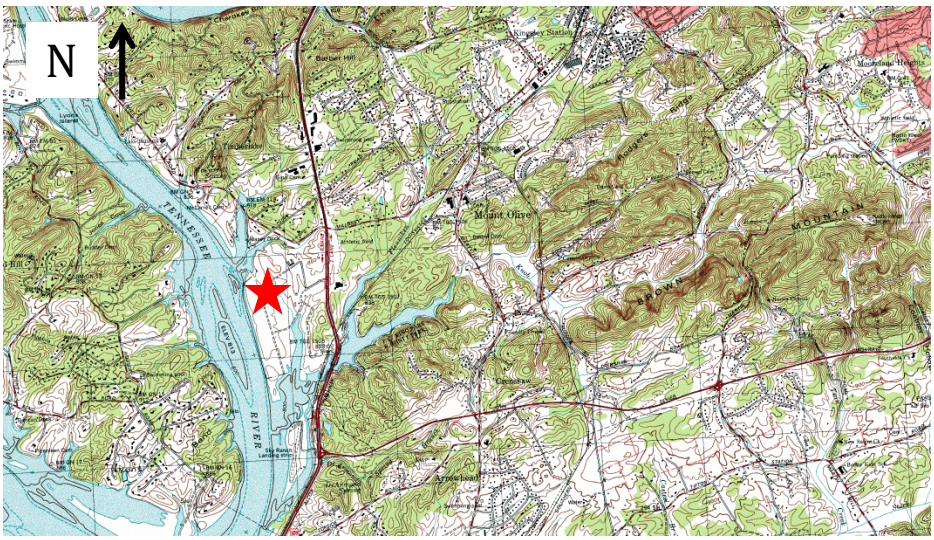

Figure 3: Topographic Map of Knoxville Quadrangle (obtained from www.TNGIS.org). The general location of the B-4 plot at the ETREC is highlighted by a red star.

based on soil studies from Elder and Springer (1963) and Leao (2009). The Sequatchie series (S_A) is comprised of very deep, well drained, moderately permeable soils that formed in loamy alluvium (Leao, 2009). Underlying the soil profile is the Ordovician Ottosee Shale which is composed of claystone, shale, limestone, and sandstone depositional sequences (Roberts, 1955). Based on well borings, the water table lies at approximately 2 meters at depth.

The profile transects were all located in the same region within the B-4 plot. The transects ran north to south along the western border of the B-4 plot approximately 2 m from the dirt road and adjacent to the fenced hydrological study area (Figure 4). The relative location of the profile transect at the B-4 plot was chosen based on the consistent elevation and soil type. The consistency of soil type was determined from past geophysical surveys conducted at the B-4 plot that are sensitive to changes in soil type (i.e. GPR, electrical resistivity, and electromagnetic methods). Additionally, the location of the profile transect contained a greater vadose zone thickness (i.e. greater depth to water table) relative to other areas on the B-4 plot. A greater area of unsaturated soil was desirable for the infiltration experiments due to the complexities that arise when the wetting front interacts with the water table The water table not only changes the seismic response, it distorts the wetting front geometry. In other words, the greater thickness of vadose zone results in a greater depth for the wetting front to migrate over.

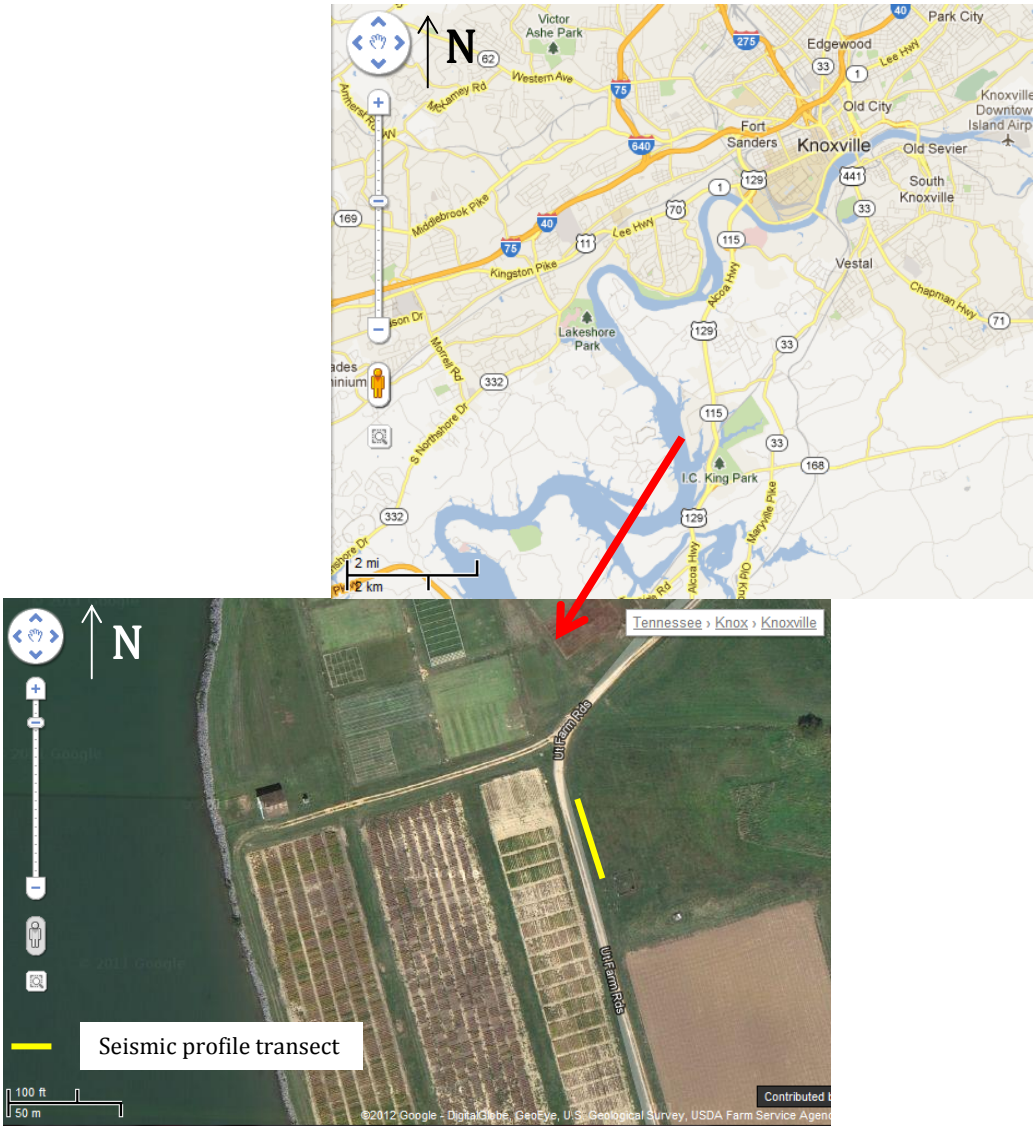

Figure 4: Google Earth™ Image of Knoxville, TN with an inset of a Google Earth™ satellite image of the B-4 plot at ETRC. The seismic profile transect used for all infiltration experiments is highlighted in yellow.

2.2. Geophysical Methods

Geophysical investigations attempt to characterize or identify changes in the Earth's subsurface using physical measurements collected at or near the earth's surface. The variations in the measurements obtained can provide information about subsurface material characteristics (i.e. rock, soil, fluids, etc.) in a relatively non-invasive manner (i.e. without drilling or trenching). Traditionally, geophysical investigations were used to examine deep earth properties that generally related to hydrocarbon exploration and other mining applications. Near-surface geophysics has become an emerging sub-discipline in geophysics over the past few decades which primarily focuses on earth materials and processes within the upper 200 meters of the subsurface.

A variety of geophysical methods can be applied to near-surface and environmental applications (e.g. electrical resistivity, seismic methods, magnetic and electromagnetic methods, micro-gravity, and ground penetrating radar) that are sensitive to small changes in observed measurements and provide a detailed understanding of the shallow subsurface. Seismic methods are used in our investigation, where the propagation of elastic waves traveling through the subsurface and later measured at the surface, allow us to reconstruct an image of the soil profile based on the velocity of seismic compressional waves.

2.2.1. Seismic First-Arrival Tomography

Seismic tomography is the geophysical processing technique used to generate the velocity profiles used in our investigation to monitor an infiltration experiment. Seismic first-arrival tomography shows the positional changes of ray-path velocities in the subsurface. SFT is the process of building an image of the subsurface velocity distribution using travel-time information that is measured on the surface via very high frequency seismometers (geophones).

Seismic first-arrival tomography generates a velocity model of the subsurface using the first-arrival times of seismic waves that geophones record at the surface. The seismic elastic waves are generally emitted from an impulsive source at a known location and measured by geophones along a profile or transect. Repeated impulsive sources or "shot points" can be taken incrementally along a profile to obtain detailed travel-time information that will be later used for tomography processing.

Reconstructing an image of the subsurface can be executed using a variety of methods including least-squares approaches (Aki et al., 1997), back-projection (Humphreys and Clayton, 1988), and variations on the preceding two techniques (Schuster and Quintus-Bosz, 1993; Zhang and Toksoz, 1998).

Figure 5: Field image of profile transect with seismic equipment employed. The red geophones can be seen in the foreground and the green plastic barrel is located in the middle of the profile transect.

2.2.1.1. Seismic Equipment

The surface seismic equipment used for each of the three experiments was uniform in both hardware and software. We used a serially modular seismograph system (Geode ™, made by Geometrics, Inc.). The system was able to support a varying number of channels depending on the number of Geodes or portable seismographs employed. Each seismograph can support 24-channels of 24-bit analog-to-digital converted data sampled up to 1/32 ms. The seismographs collect arrival time data from 40 Hz vertical geophones planted at regular intervals along the survey transect through a series of cables (Figure 5). The geophones used for our study are traditional coil and magnet devices which convert displacements in the ground into an electrical signal. The measured deviation from a base line is the seismic response recorded. The frequency response of the geophone is controlled by the spring which attaches coil and magnet and describes the corner frequency. The corner frequency is proportional to the inverse root of the moving mass surrounded by the coil inside the device. Therefore, in a response curve from 40 Hz geophones, frequencies less than 40 Hz are attenuated.

Geophones are passive devices that are constantly generating an electrical signal; therefore, the impact of the seismic source needs to be recorded as "time zero". The geophones have a microsecond accuracy that will record the time of impact from the source. The geophones were connected to "take-out" cables that link to the Geodes™, which were networked in a series (when more than 24

channels are employed), by data cables (Figure 6). The impact of an 8 pound sledge hammer on a metal plate was the transmission source used for all experiments (Figure 7). The sledge hammer was connected to the seismograph by a cable which triggers initial time as the contact pressure of the hammer hitting the plate occurs. The source was noninvasive and provides sufficient frequency content and signal-to-noise ratio for reliable data. Additionally, the sledge hammer and metal strike-plate was a convenient pair to generate the seismic source because it was not only easily stored in a field vehicle, they could be easily replaced at most hardware stores (with the exception of the trigger cable). The hammer and plate source could also be used by untrained field assistants and/or anyone who could physically swing the weight of the hammer and generate a contact with the strike plate.

2.2.1.2. Seismic Acquisition

The seismic acquisitions of all three experiments were equal in most parameters; however, small variations were made between the three experiments in order to refine methodology for optimal results. The non-uniform parameters were number of "shot-points" and number of stacks at each shot. We increased the number of "shot-points" from 12 in the first infiltration experiment to 13 in the second infiltration experiment, in an attempt to increase resolution and investigation depth of the seismic profile. The number of stacks refers to the number of times the hammer strikes the metal plate at each shot location. Determining the number of stacks needed at each shot location was determined in

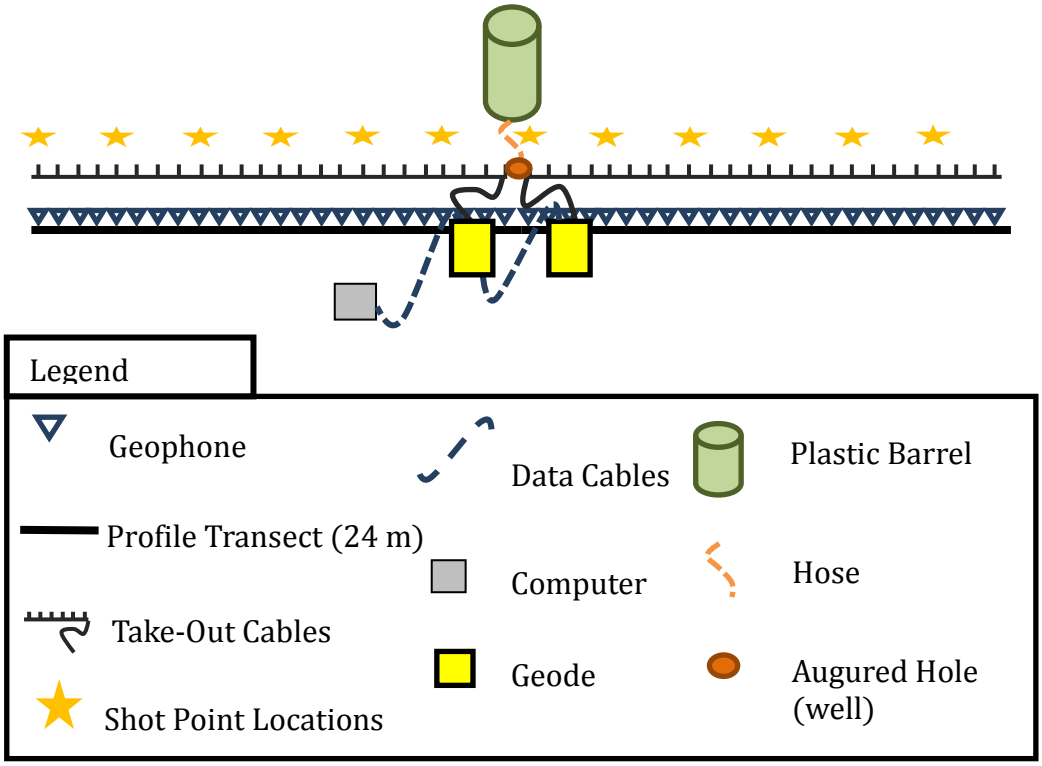

Figure 6: Schematic of profile transect at the ETREC B-4 plot.

Figure 7: Image displaying the seismic source used for each seismic profile collected. At each shot point within the seismic profiles, a sledge hammer and metal strike-plate were used to generate a manual seismic source.

the field at the time of acquisition depending on the quality of the data (i.e. signal-to-noise ratio). The number of stacks for both infiltration experiments ranged between two and four at each shot location. At each shot location, a standard of two stacks was employed and if necessary additional stacks were acquired if data appeared noisy. It took approximately 10 minutes to 15 minutes to acquire a surface seismic profile (i.e. 12 – 13 shot-points along the 24 m profile transect).

The uniform parameters include; transect length, number of geodes, number of geophones and geophone spacing, record interval, sample interval, and number of channels. The profile transect was located on the boundary of the B-4 Plot at the ETREC site running approximately north to south (Figure 8). The profile transect was located parallel to the dirt road running along the B-4 plot north of the fenced area known as the Hydrological site used by the Geology Department at The University of Tennessee. The topography was consistent over the length of the profile transect as well as depth to the water table. The profile transects were 24 m in length, with 48 geophones planted at 0.5 m increments which began at 0 m and ended at 23.5 m. Each profile contained 48 channels, therefore two geodes supporting 24 channels each. The first infiltration experiment contained a total of 12 shot points and they were taken at 2 m increments along the profile, which began at 0 m and ended at 22 m. The second infiltration experiment and constant head infiltration experiment were collected with a total of 13 shot points also at a 2 m interval which began at -0.5 m and ended at 23.5 m along the profile. An additional "shot-point" was added to the second infiltration experiment in an attempt to

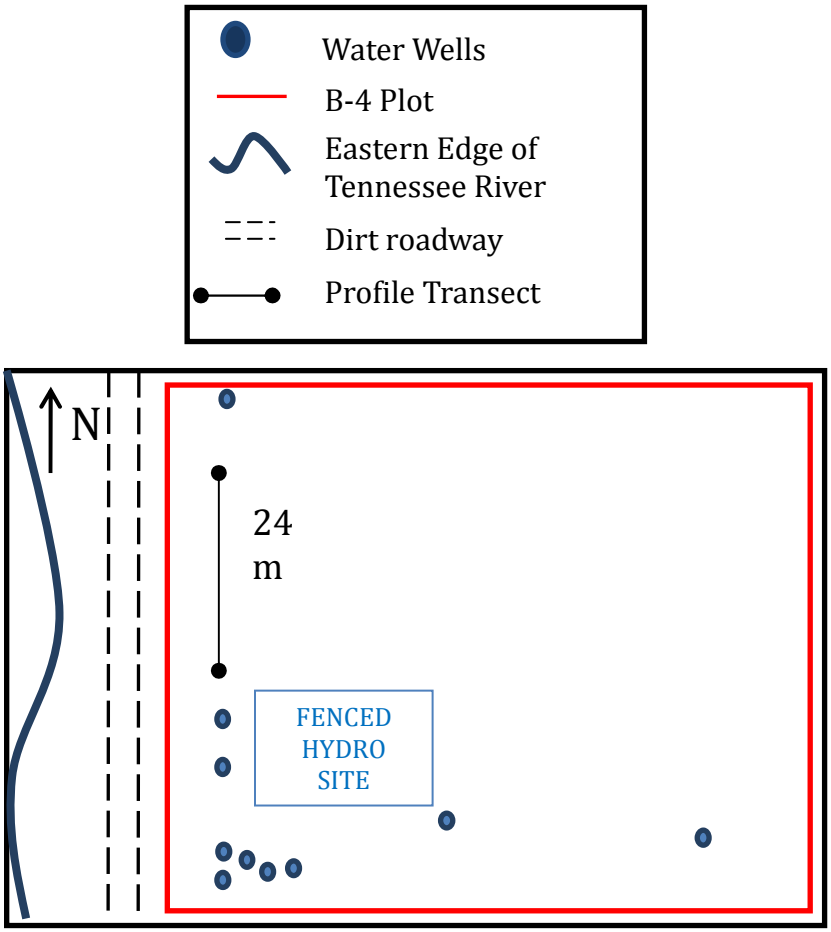

Figure 8: Schematic representation of the ETREC B-4 plot. Relative locations of the profile transect, dirt road, fenced hydro site, water wells, and the Tennessee River are shown in the image.

increase resolution and depth of investigation for monitoring the infiltration. An additional "shot-point" did not show any noticeable changes in resolution of the low-velocity anomaly. For all experiments the shot points were taken perpendicular to geophone locations (within 0.20 m) along the profile transect, to optimize accuracy of shot point location for later inversion of data.

The seismic record details the geometry of the geophones and shot point locations along the profile. As a general rule, the depth constraint of the seismic data is approximately equal to a fourth of the largest shot-receiver offset. The depth constraint of the seismic investigation is also largely dependent on the propagation velocity distribution in the subsurface. The geophone spacing controls the spatial resolution of the survey, when small geophone spacing generally results in greater resolution. The number of geophones and length of profile were greater than the necessary number of geophones and profile length to image the depth of expected infiltration depth, however, the equipment was readily available and we consider the greater resolution and profile length to provide additional information whether it was within the investigation area or not.

The seismic data collected in the field was subject to minimal processing, where no filters are applied and only a low pre-amplifier gain is used. The program used to manage the collection of seismographs in the field was Seismodular Controller™. For each of the three experiments, all acquisition parameters were kept uniform for later data comparison (stack number, sampling interval, record

interval, etc.). Stacking shot points is the process of acquiring the same shot location multiple times and summing the records together to increase signal-to-noise ratio. The stack number is determined subjectively by observing the noise window and strength of transmission source (i.e. some strike the metal plate with hammer harder and cleaner than others). A "cleaner" contact between the metal strike plate and sledge hammer generates a higher amplitude response on the seismic record. Although this creates an overall higher signal-to-noise ratio, we are only interested with the first-arrival times, not their amplitudes.

The sample interval is the length of time between recorded measurement points (voltages) at each geophone and is set at 0.125 microseconds (or 8000 Hz). This particular sampling interval allows for reconstruction of frequencies up to 4000 Hz according to Nyquist sampling theory; however, most frequencies associated with seismic traveltime data range from ~50-150 Hz. Although our investigation did not require this extensive range of data sampling, we chose this parameter because the memory associated with this sampling interval was not a concern. Most first arrival data was contained within the first ~0.05 seconds.

The record length is the time recorded after the sensor is triggered (i.e. time zero) and is 0.512 sec. The preamplifier gains are all set at a low gain and positive stack polarity. The start channel was at 1 with a t_0=0 sec and an end channel of 48 with t_{end}=0.08 sec. The noise monitor parameters were set at 0.1 mV. The infiltration for both the constant flux applicator and the constant head permeameter

test were conducted at the center of the profile transect at 12 m. A borehole was augured to a depth of 0.5 m and a diameter of 0.05 m.

2.2.1.3. Seismic Processing

Seismic tomography processing is a specific type of inversion processing. Inversion processing begins with an initial estimate for a model and proceeds with a forward calculation of the model to predict what the measurements would yield if the survey were conducted using those initial model parameters. The observed and predicted are updated until a specified residual convergence. Also referred to as refraction tomography, this method is able to resolve velocity gradients and lateral velocity variations where conventional refraction techniques fail, such as karst topography, areas of compaction, and fault zones (Zhang and Toksoz, 1998). In the case of our experiment, the inversion problem was used to take surface seismic travel-time measurements and with them we generate a velocity structure of the subsurface. Because we estimated a solution based on data that may contain noise or uncertainties, tomography processing does not create a unique solution (Jones, 2010). The problem is non-linear in that there is one known variable, the measured travel-times, and two unknowns, the pathway of the seismic energy and the propagation velocity associated with that pathway. In other words, we known the arrival-times recorded are associated with the fastest traveling rays. Therefore, the first part of the inversion processes is to generate a ray path model that represents

the shortest and fastest paths at which the rays travel to match the arrival times that are measured at the surface.

An initial gradient velocity model was then generated from seismic data. Raypaths from the initial velocity model were calculated. The initial velocity model was updated using measured travel times according to a specific tomographic algorithm employed, until the difference between the simulated travel times and measured travel times were minimized. The algorithm used for our seismic inversion scheme is the wavepath eikonal traveltime (WET) algorithm (Schuster and Quintus-Bosz, 1993).

The general flow of data processing for each of our experiments consisted of picking first arrivals off the seismographs, generating an initial model and solving the eikonal equation to estimate raypaths (Lecomte et al., 2000), and finally iteratively updating the model with arrival time data based on a specified convergence criterion. First-arrivals were manually picked in each seismograph for each of the shot points taken along the profile (i.e. all sources and receivers) using SeisImager Pickwin95™. The travel times for the entire experiment profile were saved into a single file that was imported into Rayfract™ software.

2.2.1.3.1. Picking first arrivals

The software used to import the collected seismographs in the field and manually pick first arrivals was SeisImager Pickwin95™ (Figure 9). No frequency filters were applied to the data aside from normalizing amplitude and clipping. For

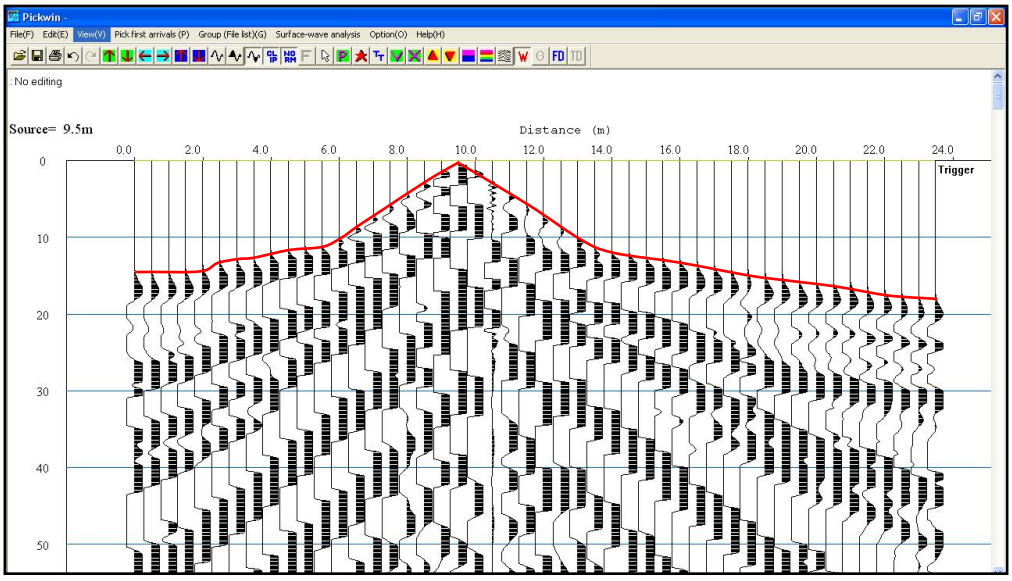

Figure 9: Seismic record example containing first-arrival picks (in red) on a single shot-point using SeisImager Pickwin95™ software

each of the seismic records and each shot point location within, the magnitude of normalization was consistent in order to pick the first arrivals as precisely as possible. Additionally, the time window (i.e. y-axis along the page, which is shown in Figure 8) was constrained to show arrivals between 0 ms and 50 ms, and the length of the profile was entirely visible on the screen, which aided in the visualization of the shot traces as a whole. Maintaining a consistent "view" of the seismic record at each shot location provided a controlled method to make first picks and ensure a certain consistency between the first arrivals picks for all profiles in each of the infiltration experiments.

2.2.1.3.2. Data Inversion Processing

The first arrivals chosen for all traces at each shot point along the profile were imported into Rayfract™ software for generating the initial model and subsequent iterative updating. The *P*-wave propagation was modeled with wave paths (known as Fresnel volumes) rather than conventional rays, which increased the numerical robustness of the method. The initial model could be generated using a variety of techniques. In Rayfract™ there are two options to create the initial model, the Delta-t-V method and the smooth inversion method.

The Delta-t-V method (Gebrande and Miller, 1985) generates an initial model that can be gridded using Surfer 8. The advantage of the Delta-d-V method is its ability to identify small features and velocity inversions; however, it can produce artifacts that may not be removed by the subsequent tomography algorithm

(Sheehan et al., 2005). The second option is the "smooth inversion" algorithm, which automatically creates a one dimensional (1-D) model based on the Delta-t-V results and further expands the 1-D model to cover the two dimensional (2-D) study area (Sheehan et al., 2005). The "smooth inversion" algorithm option begins with a simple smooth model; therefore, there are no artifacts in the initial gradient model to be concerned with in later tomography processing. In each of our experiments, the initial model was generated by using the "smooth inversion" algorithm, where the final product was a simple 2-D initial gradient model (Figure 10).

The initial gradient model was then updated using the wavepath eikonal traveltime (WET) method (Shuster and Quintus-Bosz, 1993; Woodward and Rocca, 1989). The eikonal equation relates the gradient of the travel-time to the slowness and is solved by a finite-difference method. The finite-difference method is used to determine modeled travel-times associated with shots located at points in the model coincident with the actual locations. Back projection is used in the WET algorithm and is the process of distributing observed travel time residuals along raypaths. Again, the back projection is the processes of generating the shortest and fastest paths at which the rays travel in order to arrive at the surface at the times that are observed in the field (i.e. first-arrival times).

The WET inversion algorithm utilizes the Fresnel volume approach (Spetzler and Snieder, 2004); where the Fresnel volume describes the finite area encompassing the high-frequency approximation of the raypath. The Fresnel

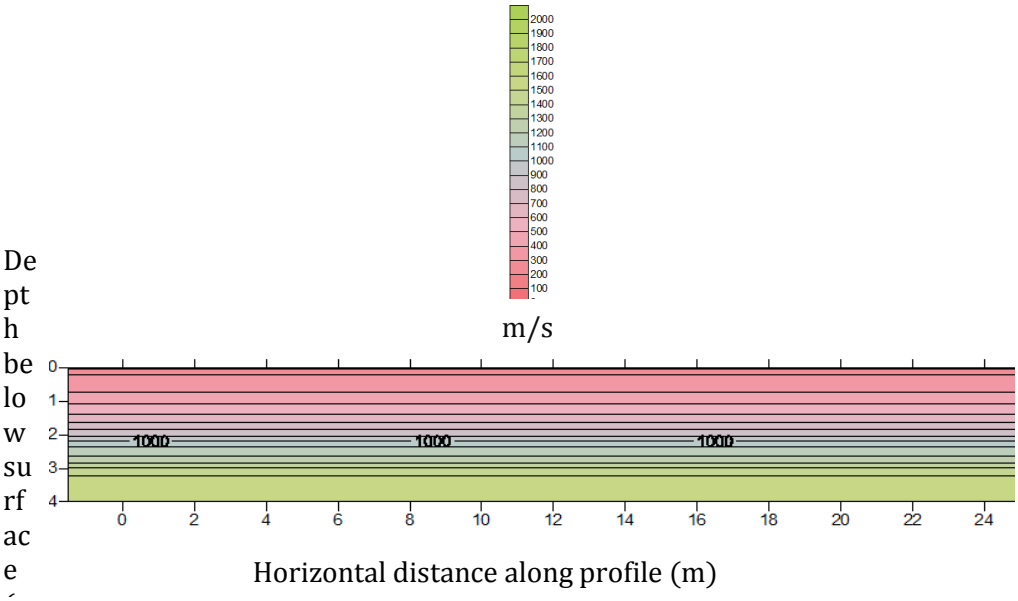

Figure 10: Example of an initial smooth gradient model generated using Rayfract™ Software.

volume is defined by a set of waveforms that arrive within a half period of the fastest traveling waveform (Sheehan et al., 2005). In heterogeneous materials, the Fresnel volume can result in subtle effects on observed travel times. This method is desirable because it accounts for wave propagation over a finite region in space which is dependent on its frequency. Many ray approximation algorithms do not address this issue.

The WET algorithm partially accounts for band-limited source and shadow effects in the data by back-projecting traveltime residuals to update the slowness field (Schuster and Quintus-Bosz, 1993). As the model is updated, the difference between the simulated and the measured arrival times are minimized to a specified convergence value defined by the user. The final product of the WET inversion algorithm tomographic processing is a gridded velocity model that represents the velocity distribution of the study area.

The Rayfract™ refraction tomography software allows for reliable imaging of subsurface velocity structure including faults, strong lateral velocity variation, and other velocity anomalies that are associated with geologic problems. We use seismic tomography to investigate hydrologic processes in the shallow subsurface. The final velocity tomograms are able to resolve an ellipsoidal low-velocity anomaly associated to a wetting front generated from the infiltration of water. By capturing velocity profiles at different time-steps during the infiltration experiment, the

spatial and temporal variation of the anomaly provides useful information regarding the soil's ability to transmit water.

2.3. Hydrogeology of the Vadose Zone

Flow and transport theory govern the processes within the vadose zone, and provide a quantitative framework and parameters that can be used to make informed predictions (Stephens, 1995). The vadose zone is broadly defined as the soil and geologic material between the ground surface and the regional water table at depth. The uppermost part of the vadose zone can include the root zone and weathered soil horizons. Materials (i.e. soils and bedrock) within the vadose zone are typically unsaturated or partially saturated if the material's pores are partially filled with water. There is an intermediate region just above the water table referred to as the capillary fringe, where materials are essentially saturated due to tension. The thickness of the capillary fringe can be less than 10 cm for gravels and up to 2 m for clays (Stephens, 1995).

2.3.1. Hydrogeologic Parameters

Understanding the dynamics of saturated fluid flow will aid in the understanding of unsaturated (or partially saturated) fluid flow dynamics in the vadose zone, also referred to as the unsaturated zone. Henry Darcy, a French engineer, designed and conducted a revolutionary infiltration experiment in the 19th century in order to purify a local water supply that had become contaminated in the city of Dijon. Darcy investigated seepage rates through sand filters to purify the

water, where he unintentionally discovered his astounding contribution (Equation 1) to the field of soil physics and hydrology, known as Darcy's Law (Darcy, 1856; Hubbert, 1956; Philip, 1995):

$$q = K\Delta H/L \qquad \text{(Equation 1)}$$

where q(L/T) is the flux density or simply flux (i.e. the volume of water flowing through a unit cross-sectional area per unit time *t*), K(L/T) is hydraulic conductivity, and ΔH/L is the change in height per unit distance in the direction of flow known as the hydraulic gradient. Darcy's law in effect, describes the transmission of water through a granular porous media. In the presence of layered soils, the effective hydraulic conductivity (K_{eff}) is dependent on the layer thickness, and each layer affects the hydraulic conductivity of the layer beneath it. Layers containing lower hydraulic conductivities are weighted more when calculating the K_{eff}. Therefore, Darcy's law accounts the effect of one layers hydraulic conductivity on the hydraulic conductivity of an adjacent layer, where the effective hydraulic conductivity of the total soil profile is not averaged but weighted accordingly.

However, Earth processes and material properties are vastly dynamic; therefore, when considering unsteady flow (i.e. flux changes with time) or soil non-uniformity, the hydraulic head may not decrease linearly along the direction of flow (Hillel, 1998). Limitations of Darcy's law exist when considering different scales of the flow system, whether it is microscopic or macroscopic.

Hydraulic conductivity is highly sensitive to the texture and structure of the porous media, and can range from 10^{-2} to 10^{-4} m/s in coarse-textured (and/or highly structured/cracked soils) to as low as 10^{-8} to 10^{-10} m/s in compacted, structureless clay soils (Dane and Topp, 2002). Generally there are three types of hydraulic conductivity values, saturated hydraulic conductivity (K_s), field-saturated hydraulic conductivity (K_{fs}), and unsaturated hydraulic conductivity (K_{unsat}).

Saturated hydraulic conductivity is measured in a porous medium where all pores are saturated. Field-saturated hydraulic conductivity measures saturated hydraulic conductivity via infiltration into an initially unsaturated or partially saturated soil (Reynolds et al., 1983). This parameter recognizes that air is typically entrapped in a porous medium when the medium is "saturated" by infiltrating water, especially in the case of downward infiltration under ponded conditions (Dane and Topp, 2002). Field-saturated hydraulic conductivity is often considered more appropriate for the vadose zone or unsaturated zone because most natural infiltration processes and anthropogenic processes (rainwater infiltration, drip irrigation, wastewater disposal via leach field, etc.) result in air entrapment within the porous medium (Bouwer, 1978). We investigate saturated and field-saturated hydraulic conductivity within this study.

2.3.2. Vadose Zone Field Methods

As previously mentioned, many investigations related to the vadose are dependent on the theory of fluid flow and transport. Saturated and field saturated

water flow parameters describe or quantify the ability of a porous media (e.g. soil or rock) to transmit water when the porous medium is under saturated or nearly saturated conditions (Dane and Topp, 2002). The magnitudes of these flow parameters are dependent on grain size distribution, roughness, tortuosity, shape, and permeability of the material (Dane and Topp, 2002).

In the vadose zone, saturated and field-saturated flow parameters are generally estimated using various ring infiltrometer and borehole (well) permeameter methods (Dane and Topp, 2002). Saturated and field-saturated water flow parameters can be highly variable, both temporally and spatially, and with coefficients of variation as high as 400% (e.g. Warrick and Nielsen, 1980).

2.3.2.1. Summary of Techniques

A ring infiltrometer is a thin-walled, open-ended, cylinder made of plastic or metal (Dane and Topp, 2002). Various cylinder arrangements are possible, but generally a single-ring or double-ring (or concentric-ring) arrangements are commonly used. The double-ring (or concentric-ring) infiltrometer has an inner measuring ring and an adjacent outer cylindrical buffer-ring. Both the single-ring and double-ring (or concentric-ring) infiltrometers are used primarily for measuring cumulative infiltration I(L), infiltration rate, q=dI/dt(L T^{-1}), and field-saturated hydraulic conductivity, K_{fs}(L T^{-1}). For most field investigations, the cylinders range from 10cm to 50cm in diameter, and 5 cm to 20 cm at length (Dane and Topp, 2002). The cylinders are driven into the soil, generally 3cm to 10cm, and

a head of water is ponded within the cylinder (Figure 10). Details of apparatus and procedure for the single and double-ring (concentric-ring) infiltrometer can be found in Methods of Soil Analysis Part 4 (section 3.4.3.2), by Dane and Topp (2002).

It is observed in both theory and experimentation, that infiltration rate through a ring or cylinder infiltrometer is initially large and decreases with time to reach quasi-steady state; where the time to reach quasi-steady state is decreased as the diameter of the cylinder decreases (Youngs, 1987, 1991a). Problems in obtaining a quasi-steady state of infiltration arise in areas with large natural variability of soils causing erratic changes in infiltration (Dane and Topp, 2002). Quasi-steady state infiltration via a ring infiltrometer can be expressed using the Reynolds and Elrick (1990) relationship (Equation 2):

$$\frac{q_s}{K_{fs}} = \frac{Q}{(\pi a^2 K_{fs})} = \left[\frac{H}{C_1 d + C_2 a}\right] + \left\{\frac{1}{[\alpha^*(C_1 d + C_2 a)]}\right\} + 1 \qquad \text{(Equation 2)}$$

where q_s(L T^{-1}) is quasi-steady state infiltration rate, Q(L^3 T^{-1}) is the corresponding quasi-steady flow rate, a(L) is ring radius, H(L) is the steady depth of ponded water in the ring, d(L) is the depth of ring insertion into the soil, α^*(L^{-1})soil macroscopic capillary length, $C_1 = 0.316\pi$ and $C_2 = 0.187\pi$ are dimensionless quasi-empirical constants that apply for d ≥ 3 cm and H ≥ 5 cm (Reynolds and Elrick, 1990; Youngs et al., 1995).

The Amoozemeter, or compact constant head permeameter (CCHP), is a common field instrument for estimating *in-situ* saturated hydraulic conductivity in

the vadose zone. As we previously discussed, we refer to the estimation of saturated hydraulic conductivity as field-saturated hydraulic conductivity, when measuring K_s via infiltration in to an initially unsaturated soil. The procedure for estimating K_{fs} using the Amoozemeter (or CCHP) is determined using the constant-head well permeameter technique, also known as the borehole permeameter method (see Amoozegar and Warrick, 1986; Reynolds and Elrick, 1986). A detailed description of the procedure can be found in a number of publications (e.g. Amoozegar and Warrick, 1986). A variety of constant head well permeameter designs exist; however, we focus on the Amoozemeter (CCHP) design, because this particular instrument is used in one of our infiltration experiments to estimate K_{fs} in order to compare estimates obtained using the newly proposed infiltration TLSFT technique.

The Amoozemeter is a single unit comprised of five sections: four constant-head tubes, a four-liter main water reservoir, a one-liter flow measuring reservoir, water dissipating unit, and a base with a three way valve (Figure 11). At the base of each constant-head tube is an air tight seal. Two small diameter air tubes are installed in each constant-head tube through a rubber stopper. One air tube (referred to as the "bubble tube") extends to approximately 5 mm above the bottom of the constant-head tube. The other tube, referred to as the "air tube", only extends into the air void above the water level in the constant-head tube. Each air tube is connected though flexible plastic tubing to a quick release connector to allow for quick and easy connections to the adjacent bubble tube to serially connect the

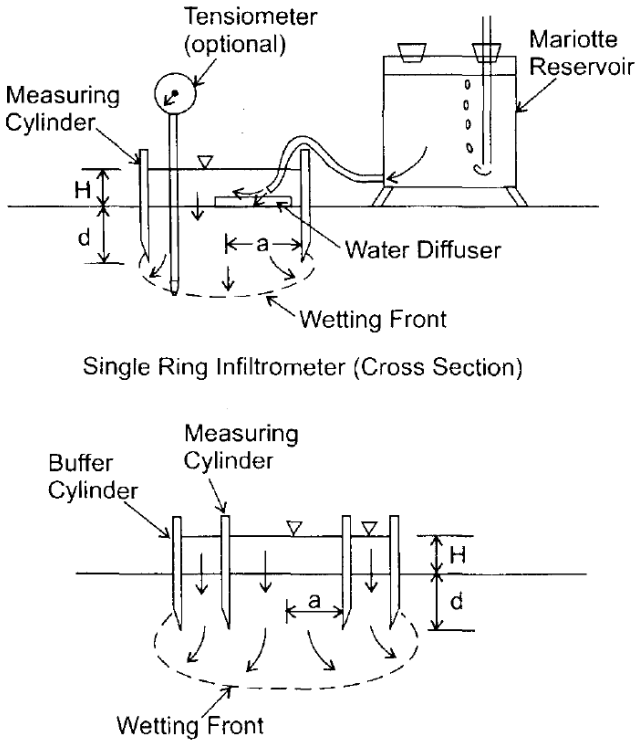

Figure 11: Schematic representation of a single ring infiltrometer (top panel) and a double-ring or concentric ring infiltrometer (bottom panel). Image from Methods of Soil Analysis Part 4, section 3.4.3.2a. Dane and Topp (2002)

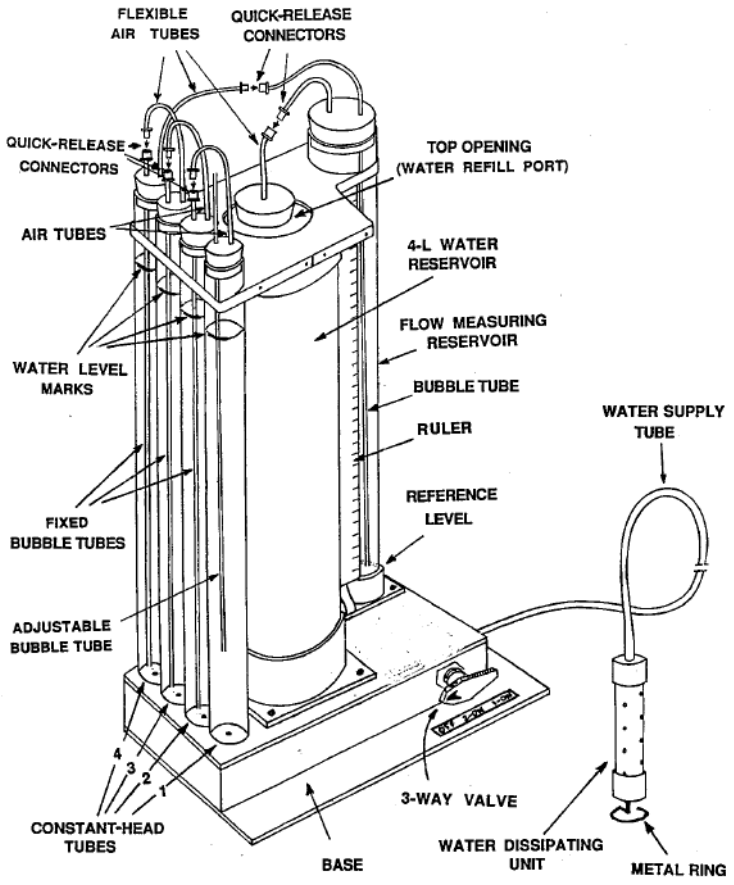

Figure 12: Schematic representation of the Amoozemeter components. Image from CCHP Manual (Ksat Inc.)

constant-head tubes to one another and to the flow measuring reservoir as needed. The bubble tubes inside the #2, #3, and #4 tubes are fixed and the bubble tube inside constant-head tube #1 is adjustable based on the ponding head level desired by the user.

Measurements are noted of augured depth from the soil surface of the hole and the Amoozemeter is stabilized near the augur hole. Given the final depth of the hole and placement of Amoozemeter at the surface, the bubble tube is adjusted to the appropriate height and the number of constant-head tubes are then determined (Figure 12). Once the reservoirs are filled, the valve is opened and all air bubbles will flow through the whole unit. Records of the number of constant-head tubes are recorded, as well as the height of water in augured hole, and adjusted height of bubble tube. These parameters are needed for later calculation of K_{fs} (Figure 13).

The initial reading off the flow measuring reservoir is noted and once the valve is opened and water is flowing out of the unit, the elapsed time is recorded. Bubbles from the bubble tube will slow and become steady as steady state infiltration is reached, which is generally reached when three consecutive reading of the water drop/time in the measuring reservoir are approximately the same. As the flow measuring reservoir drains, periodic readings from the drop in water level off of the flow measuring reservoir are recorded along with the time of measurement taken. The increments of measurement times are specified by the user. Depending on the soil type, the water in the reservoir can take from 30min to 10 hours to drain.

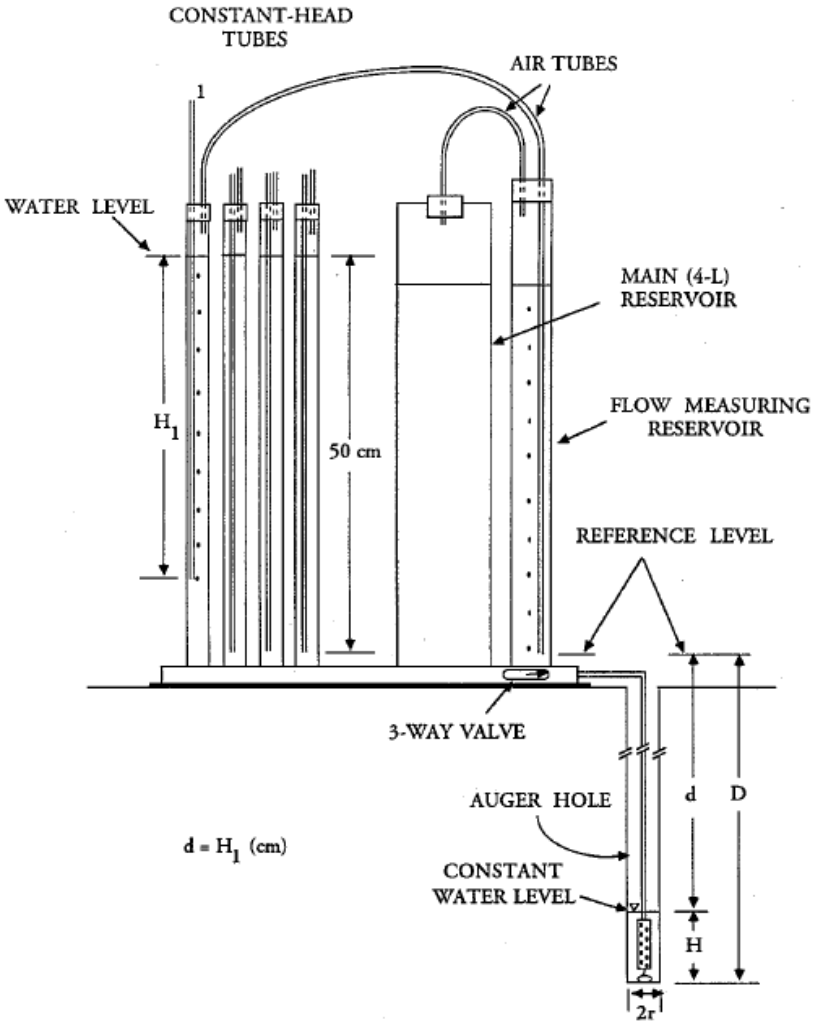

Figure 13: Schematic representation of the Amoozemeter components and parameters recorded for later calculating *in-situ* K_{sat}. Image from CCHP Manual (Ksat Inc.)

To calculate field-saturated hydraulic conductivity (or K_{sat} as referred to in the manual), outflow is first calculated using the following form of Darcy's law equation and data collected in the field (Equation 3):

$$Q = \frac{dA}{T} \qquad \text{(Equation 3)}$$

where Q(L^3/t) is the outflow volume per unit time, d(L) is the drop in water level, and A(L^2) is the area of the reservoir cylinder which is 105 cm^2 for both reservoirs (i.e. valve is turned to "2 on"), and T(t) elapsed time since previous reading. In the second step of obtaining an estimate of field-saturated hydraulic conductivity, we transform Q into K_{sat} using Glover's solution (Amoozegar, 1989) (Equation 4):

$$K_{sat} = Q\left\{\frac{\left[sinh^{-1}\left(\frac{H}{r}\right)-\left(\left(\frac{r}{H}\right)^2+1\right)^{\frac{1}{2}}+\left(\frac{r}{H}\right)\right]}{2\pi H^2}\right\} \qquad \text{(Equation 4)}$$

where Q(L^3/t) is outflow volume per unit time, H(L) is constant head in borehole, r(L) is borehole radius, $sinh^{-1}$ is the hyperbolic sine function, and π is pi.

2.3.2.2. Limitation of Techniques

One of the simplest single-ring and concentric-ring infiltrometer analyses for K_{fs} assumes $K_{fs} = q_s$. This assumption results in the overestimation of K_{fs} by varying degrees depending on the magnitudes of the different parameters (Dane and Topp, 2002). A direct determination of K_{fs} can be determined by solving for K_{fs} from Equation 5. The α* parameter must be estimated from the soil texture and structure

from a table, or by measuring it using independent methodology. Bouwer (1966, 1986) provides an additional (Equation 5) analysis applying the Green and Ampt (1911) equation to one-dimensional vertical flow within and below the measuring cylinder:

$$\frac{q_s}{K_{fs}} = \left(\frac{H}{L_f}\right) + \left[\frac{1}{\alpha^* L_f}\right] + 1 \qquad \text{(Equation 5)}$$

where L_f(L) is the depth from the infiltration surface to the wetting front. As with Equation 7, the α* parameter must be selected from a table or measured independently (Dane and Topp, 2002). However, Equation 8 also overestimates K_{fs} under quasi-steady flow by the lateral flow divergence in the pressure and capillarity terms (Dane and Topp, 2002).

Furthermore, numerical simulations, laboratory and field tests show the ineffectiveness of the buffer ring in the concentric-ring infiltrometer because quasi-steady infiltration rate from the measuring cylinder is still substantially influenced by flow divergence (Dane and Topp, 2002). Physical sources of measurement error in both single-ring and concentric-ring infiltrometers include compaction of soils during the insertion of the rings, short circuit flow along the walls of the cylinder, siltation of the infiltration surface, and gradual plugging of soil pores (Dane and Topp, 2002).

Limitations of the Amoozemeter (CCHP) or constant head well permeameter method include smearing, siltation, or compaction of the soil within the

measurement zone can result in unrepresentative K_{fs} values. Additionally, the time required to reach quasi-steady flow for the well-permeameter is determined by the permeability of the soil or material, antecedent water content in the soil or material, the radius of the well, and depth of water ponding (Dane and Topp, 2002). Generally, equilibration time increases with decreasing soil permeability, decreasing antecedent soil moisture, increasing well radius, and increasing depth of water ponding (Reynolds and Elrick, 1986).

Both the ring infiltrometer and constant head well permeameter methods estimate hydraulic conductivity by a single point location. If a short-circuit structure is present in the vicinity of infiltration, the hydraulic conductivity estimate erroneously high. In contrast, if a clay lens exists below the point of infiltration, the field site is classified as an erroneously low hydraulic conductivity soil.

3. MONITORING SURFACE INFILTRATION FROM A CONSTANT FLUX APPLICATOR USING TIME-LAPSE SEISMIC FIRST ARRIVAL TOMOGRAPHY

This chapter is based on a paper that is in preparation by Rachel Elizabeth Storniolo, David P. Gaines, Gregory S. Baker, Ed Perfect, and Jaehoon Lee to be submitted to GEOPHYSICS. Note: Some material covered in this chapter is repeated from within the previous introduction and background chapters in order to exist in a stand-along publishable format.

Abstract

Determining hydrogeologic parameters in the vadose zone using conventional hydrologic instrumentation and methods can be problematic due to their inability to locate heterogeneities and anisotropic features in the subsurface. Fluid movement is critical in evaluating rainwater infiltration rates, contaminant transport, drip irrigation efficiency, and monitoring reservoirs. Current methods used to quantify fluid transport in the vadose zone generally use measurements collected at the surface during an *in-situ* infiltration experiment. The point-source surface measurements are unable to provide a visual characterization of the spatial distribution and geometry of the migrating wetting front generated from surface infiltration. An *in-situ* surface infiltration experiment was conducted simultaneously with the collection of surface seismic data at the East Tennessee Research and Education Center (ETREC) plot B-4. Time-lapse seismic first-arrival tomography (TLSFT) is able to resolve the changes in seismic *P*-wave velocities as a result of water infiltration from the surface. We develop a new methodology for

imaging the migration of a wetting front in the vadose zone generated from a surface infiltration experiment. A constant flux applicator was used to infiltrate water into the subsurface while simultaneously collecting seismic first-arrival data at the surface. The *P*-wave velocity tomograms generated from TLSFT data were able to resolve the ellipsoidal velocity perturbations at different time-steps during the infiltration experiment. The velocity tomograms are a proxy for the relative saturation changes in the subsurface as the migrating wetting front travels through the upper 0 m – 2 m of the vadose zone. Imaging the development of a wetting front using the spatial and temporal variations of seismic first-arrival travel time data is a useful and relatively non-invasive method to obtain a visual characterization of wetting front geometry and distribution. Results from the infiltration experiment using the TLSFT method yielded five time-lapse *P*-wave velocity tomograms imaging a migrating wetting front generated from infiltration at the surface. Imaging a migrating wetting front using the TLSFT infiltration method can be used to identify and locate anisotropic or structural features in the subsurface that may dominate fluid transport.

3.1. Introduction

Fluid flow in the near surface is of interest to a variety of engineering and environmental problems (i.e. hazard prevention and best management practices of in the fields of agriculture, building construction, waste management, and managing resources). The rate or transport of fluid is essential for investigating infiltration

and irrigation rates, characterizing reservoirs, evaluating contaminant fate and transport, monitoring subsurface waste disposal, and preventing floods and landslides.

3.1.1. Motivation

Current infiltration methods provide quantitative values of fluid flow in the vadose zone; however, they are often unable to capture heterogeneous or anisotropic features in the subsurface that may be dominating subsurface fluid migration. Therefore, there is a need for determining anisotropy and geometry of fluid migration in the vadose zone that is non-invasive, practical for use under a variety of conditions, and able to provide a comprehensive understanding of subsurface flow characteristics and potential governing structures.

3.1.2. Objective

We use time-lapse seismic first-arrival tomography (TLSFT) to monitor an infiltration experiment, using *P*-wave velocity perturbations as a proxy for the relative changes in saturation as the wetting font advances in the subsurface. As the wetting front advances with time and space, a series of TLSFT data are collected to observe the distribution and geometry of the fluid.

3.2. Background

Seismic first-arrival tomography (SFT) is a geophysical method that provides a velocity model or tomographic profile of the subsurface using measured travel-

time information collected at the surface. As a seismic source is generated, compressional waves (*P*-waves) propagate through the subsurface and later return to surface where sensors (or geophones) record their arrival times. Seismic first-arrival tomography measure positional changes in *P*-wave velocities as they interact with changing material properties in the subsurface. The *P*-wave velocities speed or slow depending on subsurface materials and the arrival-times are measured at the surface. Compressional waves (*P*-waves) are used because they are the fastest traveling waves, therefore the first to arrive on the seismographs.

The seismic velocity tomograms are the result of forward and inverse modeling of seismic ray-paths and their observed arrival-times. Seismic first-arrival tomograms can be computed using various algorithms, but the simplified processing work flow begins with picking first arrival times from a seismograph and developing an initial forward model. Finally, by iterative processes, the initial model is compared against the travel-time data and updated until a specified convergence (e.g. Schuster and Quintus-Bosz, 1993; Zhang and Toksoz, 1998). Tomographic reconstruction of *P*-wave arrival times vary based on examination of the ray-tracing scheme details, development of initial model, and how the model is updated. Time-lapse simply refers to the process of collecting SFT profiles at different time-steps to observe temporal variations in the velocity tomograms.

The effect of saturation and pore fluids on seismic velocity has been a petrophysical subject of interest for decades in many theoretical (Gassman, 1951;

Biot, 1956) and experimental investigations (Murphy 1982). In more recent decades, the application of seismic methods to near-surface and hydrogeological problems have become an emerging interest in the field in geophysics (Bachrach and Nur, 1998; Steeples and Miller, 1998; Zimmer et al, 2007). Seismic refraction and reflection methods have been successful at mapping the water table (Haeni, 1986; Bachrach and Nur, 1998), investigating shallow fluid flow and saturation effects (Bachrach and Nur, 1998), and locating perched water bodies (Gaines, 2011).

As water content varies in the vadose zone, seismic *P*-wave velocities are affected by the changes in the material's density and effective bulk modulus (Figure 14). The Gassman equation provides an understanding of the petrophysical relationship between water saturation and seismic *P*-wave velocity. The mathematical relationships between density, effective bulk modulus, and saturation have been documented (Domenico, 1974; Mavko et al., 1995; Bachrach and Nur, 1998) and are further investigated in laboratory experiments (George et al., 2009).

The effect on *P*-wave velocities with changing saturation can be broadly categorized into two groups, the linear and non-linear domain (Domenico, 1974; Mavko et al., 1995; Bachrach and Nur, 1998). Following the Gassman equation, the linear domain is a variably saturated porous medium (i.e. above the water table) where saturation values are below a 99% saturation threshold, and result in a

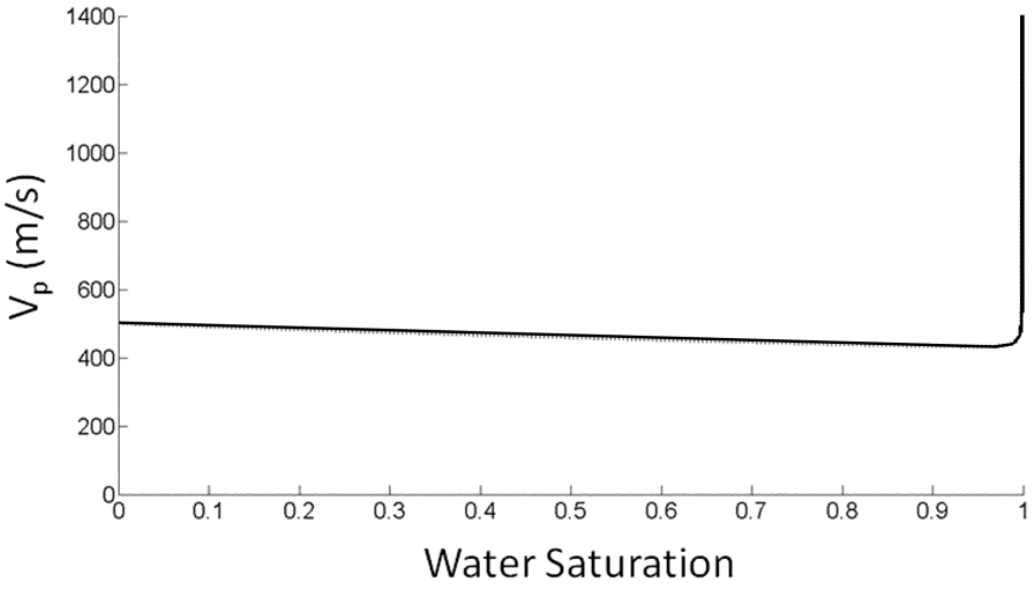

Figure 14: A graph showing the relationship between *P*-wave velocity and water saturation according to the Gassman equation.

gradual decrease in *P*-wave velocity with increasing saturation. The non-linear domain is characterized by a rapid increase in *P*-wave velocity between the 99% - 100% saturation range. George et al. (2009) has demonstrated in recent laboratory experiments that the change in seismic *P*-wave velocity is less abrupt than previous theoretical predictions. This discovery introduces difficulty in establishing a direct relationship between specific saturation values and the corresponding *P*-wave velocity in various soil environments.

Hydraulic parameters such as saturated and field-saturated hydraulic conductivity characterize or quantify the ability of a porous material to transmit water when the material is saturated or nearly saturated (Dane and Topp, 2002). The magnitudes of these parameters are dependent on soil properties, such as grain size distribution, roughness, tortuosity, shape, and permeability of the porous medium (Dane and Topp, 2002).

Characterizing and quantifying fluid flow in the vadose zone is commonly obtained via *in-situ* surface infiltration experiments using various ring or pressure infiltrometers, as well as borehole or well permeameter methods. A quantitative calculation of hydraulic conductivity and/or other fluid flow parameters are obtained using these methods; however, the geometry and spatial distribution of the water as it infiltrates into the subsurface is unknown due to the difficulty of imaging the a migrating wetting front in the vadose zone non-destructively.

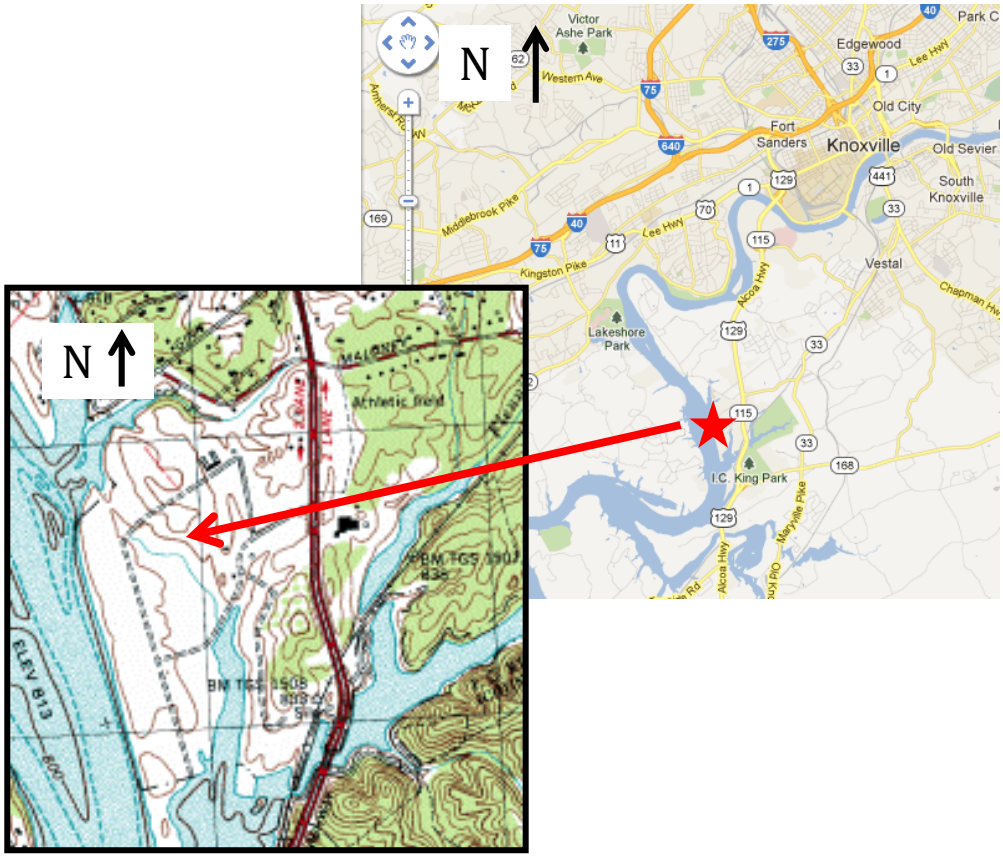

Figure 15: A Google™ image of Knoxville, TN with a topographic map inset showing the general location of the B-4 plot at ETREC where the TLSFT infiltration experiment was conducted. The topographic image is obtained from www.TNGIS.org.

3.3. Experiment Site Description

The infiltration experiment and collection of surface TLSFT data were carried out at the Tennessee Agricultural Experiment Station, East Tennessee Research and Education Center (ETREC) Plot B-4 (Figure 15). The ETREC is located approximately two miles south of The University of Tennessee main campus in Knoxville, Tennessee. The field site is also referred to as the Environmental Hydrology and Geophysics Teaching and Research Site and is commonly used for upper-level undergraduate and graduate hydrogeology field courses, in addition to TINGS (Tennessee Intensive Near-Surface Geophysics Study) course.

The region lies within the Valley and Ridge Province associated with the Appalachian Mountain Range, where alluvium deposits are composed of weathered materials originating from shales, limestones, sandstones, and metamorphosed micaceous rocks (Roberts, 1955). The B-4 plot is located approximately 150 m east of the Tennessee River on the lowest lying river terrace. The site contains soil from the Sequatchie series based on soil surveys from Elder and Springer (1963) and Leao (2009). The Sequatchie series (S_A) is comprised of very deep, well drained, moderately permeable soils that formed in loamy alluvium.

The water table is at approximately 2 m at depth from nearby water wells. The variable soil conditions across the ETREC site, ranging from residual soils atop Ordovician sedimentary bedrock (near the highway), to the loamy textures

developed from alluvial deposits (near the river), are common to east Tennessee and important for forestry and agriculture.

3.4. Data Collection

The infiltration experiment and seismic data acquisition were conducted in the early fall of 2010 using a constant flux applicator as the infiltration device (Gaines, 2011). A plastic barrel was filled with approximately 200 liters (0.2 m^3) of water and placed at the center of the surface seismic profile. The seismic profile ran 24 m in length, where geophones were planted at every 0.5 m along the profile, acting as receivers recording the vertical component of seismic compressional waves. The geophones recorded at a 40 Hz bandwidth. The seismic source was manually controlled by driving a sledge hammer onto a metal strike-plate. Twelve shot points were taken at 2 m increments along the profile beginning at 0 m and ending at 22 m laterally on the profile. The 48 geophones recorded the arrival-times of *P*-waves along the profile. Time zero began when the acquisition board was triggered by the pressure of the sledge hammer making contact with the metal strike-plate. The data were stacked variably (2-4 stacks at each shot-point) according to the signal-to-noise ratio observed upon data collection. The SFT data were collected simultaneously with an infiltration experiment using a constant flux applicator.

The experiment was designed to monitor the *P*-wave seismic velocity response of a wetting front advancing though the subsurface spatially and

temporally. A total of 170 L (0.17 m^3) of water was discharged over a period of 112 minutes. The total 200 L (0.2 m^3) could not be fully discharged into the subsurface due to the location of the outflow spigot which was approximately 15 cm from the base of the barrel. The volume of water was measured when filling the barrel (0.2 m^3) and the approximate volume of water remaining in the barrel after infiltration was recorded. The difference between the two was the total volume of water infiltrated during the experiment (0.17 m^3). The water was infiltrated into an augured well (or cylindrical borehole) with a 0.05 m diameter and to a depth of 0.5 m. The rate of infiltration was not tightly controlled; therefore a single discharge value and volume were used for estimating the total infiltration outflow volume and rate (0.17 m^3/112 min). Runoff or ponding at the surface was observed during the experiment due to the faster infiltration rate relative to the soil's ability to intake the water.

The data were collected on the same day at approximately 30 minutes intervals; in which infiltration began at time zero and a "baseline" or background velocity profile was collected prior to infiltration. A total of six (including "baseline") surface seismic surveys were collected. The five profiles collected concurrently with infiltration were acquired at the following times; 45 min, 75 min, 120 min, 140 min, and 180 min. The concurrent infiltration time-steps; 45 min, 75 min, 120 min, 140 min, and 180 min, produced distinct low-velocity perturbations relative to the baseline profile.

3.5. Methods and Analysis

First-arrival times were manually selected in SeisImager Pickwin95™ software for each shot-point within each of the six seismic profiles. The travel-time data was imported into Rayfract™ for tomographic inversion modeling. The initial smooth 1-D model was generated by back-projecting traveltime residuals and solving the eikonal equation to determine raypaths (Lecomte et al., 2000). The initial model was then updated using measured travel times and iterating until convergence (Schuster and Quintus-Bosz, 1993). The smooth 1-D initial gradient model was generated using the background or baseline profile travel time data. The resulting initial gradient model provided an accurate location of the water table at a depth of two meters and gradual increase of velocity with depth structure (Figure 16). The background initial gradient model was then used in all concurrent infiltration profiles as the initial gradient model. In other words, the travel times for each of the respective concurrent infiltration profiles were used to update the baseline initial model iteratively until convergence, producing the final 2-D velocity model (Figure 17).

A trend-analysis was applied to the five seismic *P*-wave tomograms collected during the infiltration experiment (Figure 18). The trend-analysis resulted in the separation of the regional and local components. The regional component represents the subsurface before infiltration begins, in other words the background or "baseline" profile. The local component represents the change in velocity due to

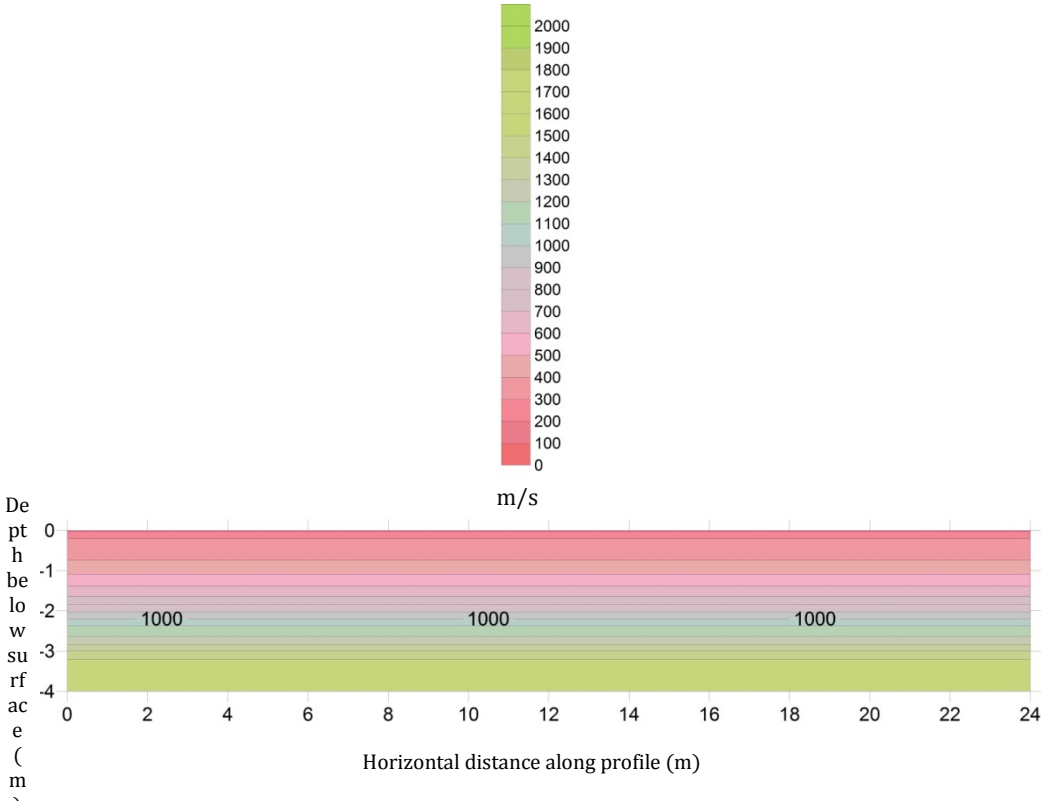

Figure 16: Initial smooth gradient velocity model from the background (baseline) profile. The water table is shown at approximately 2 m. The profile unit is *P*-wave velocity in meters per second, with a contour interval of 100m/s.

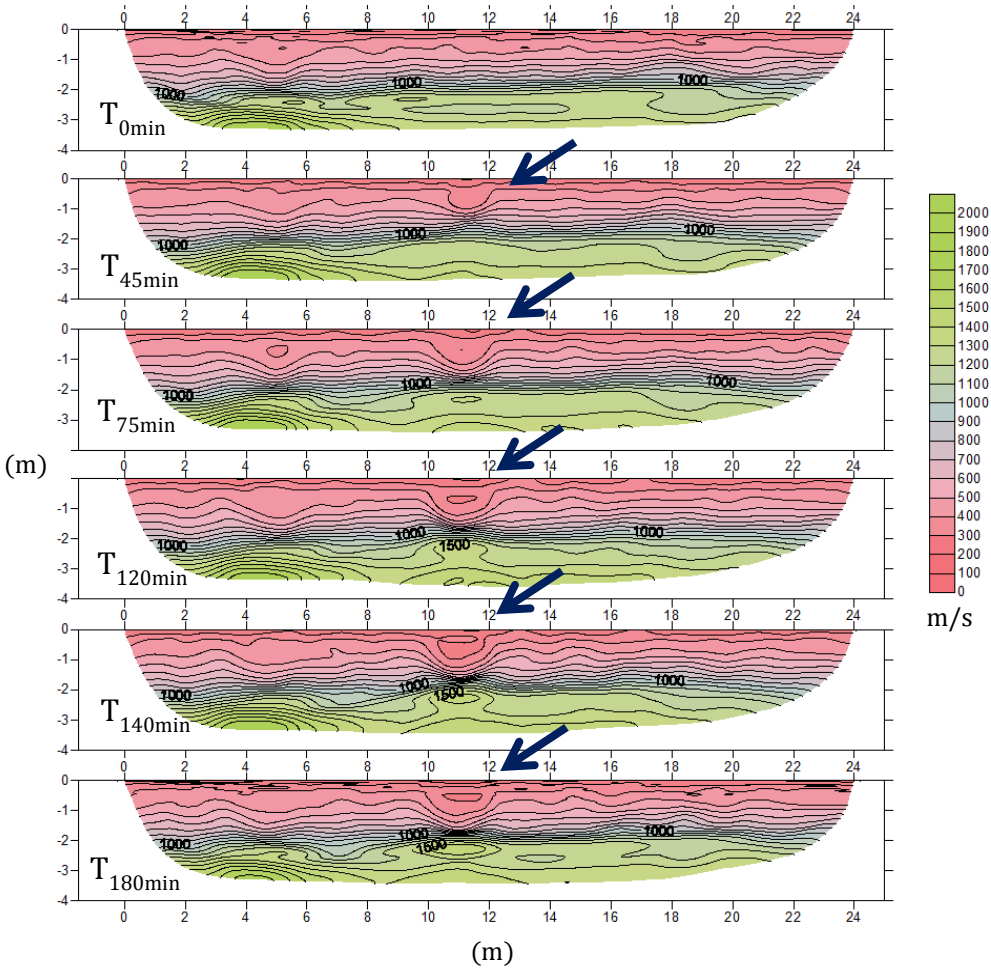

Figure 17: The six *P*-wave velocity tomograms from the first constant flux applicator TLSFT infiltration experiment. The first panel is the baseline profile prior to infiltration and the following profiles are collecting after infiltration has begun at T_{45min}, T_{75min}, T_{120min}, T_{140min}, and T_{180min}. The unit is measured in *P*-wave velocity in meters per second with a contour interval of 100 m/s. The blue arrows identify the low-velocity anomalies associated with water infiltration from the surface.

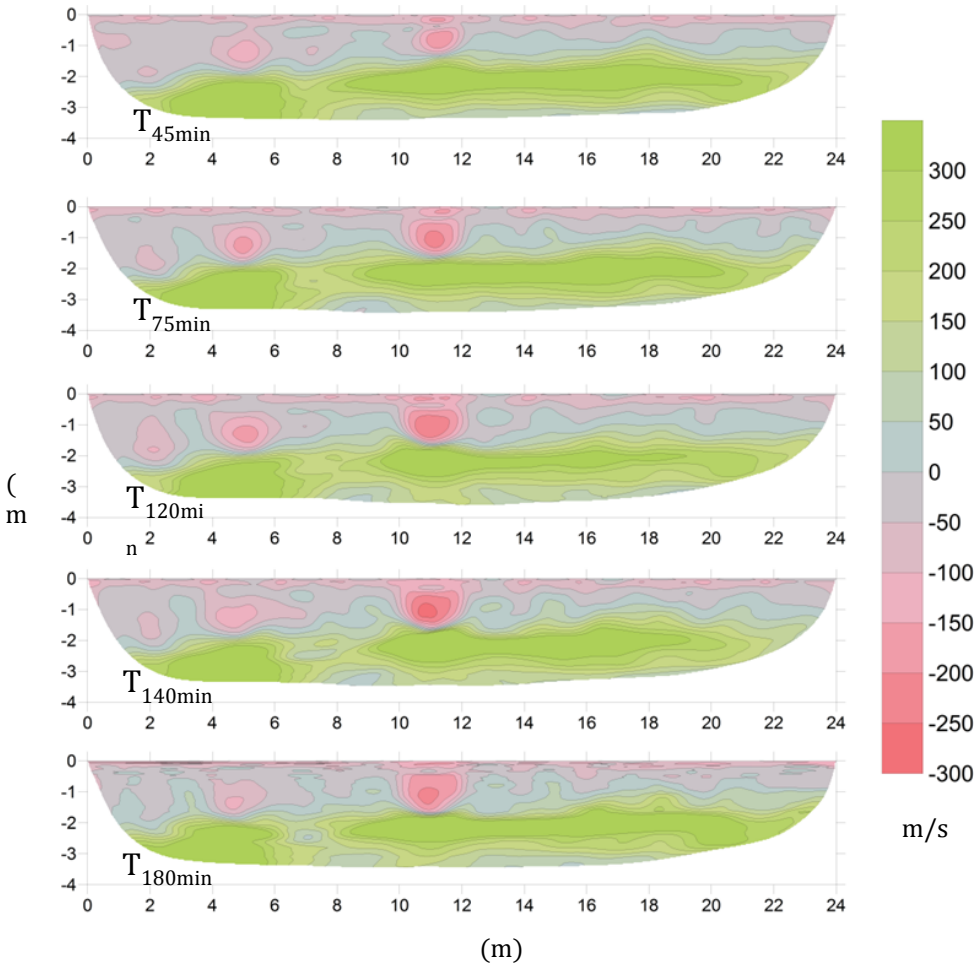

Figure 18: The five TLSFT profiles for the first constant flux applicator experiment and with a trend analysis applied. The trend analysis is the difference between the baseline profile and each of the post-infiltration profiles (post-infiltration – baseline). The ellipsoidal velocity perturbation is identified at the same lateral location at which infiltration occurs at the surface. The *P*-wave velocity ranges in each tomogram from -300 m/s to 300 m/s.

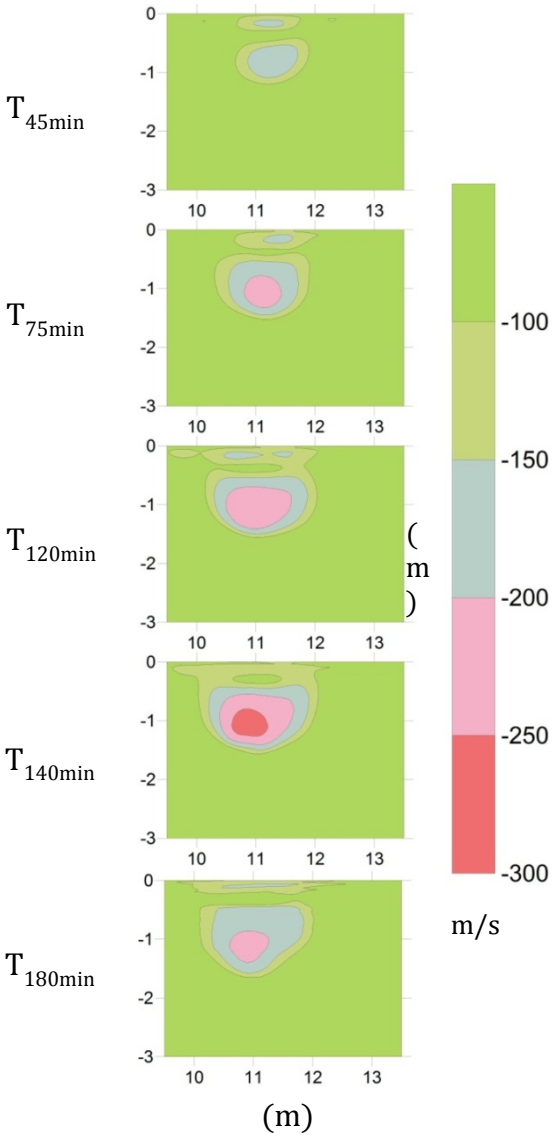

Figure 19: Discrete *P*-wave velocity profiles centered on the area of infiltration for the first constant flux applicator experiment with the velocity interval constrained to be from -300 m/s to -100 m/s and a contour interval of 50 m/s. A trend analysis has been applied to each of the profiles.

relative saturation changes in the subsurface from infiltration (i.e. wetting front). The trend-analysis aided in producing isolated velocity perturbations that were only attributed to the infiltration experiment. The result is an ellipsoidal velocity anomaly in the shape of the wetting front.

3.5. Results

The *P*-wave velocity tomograms are constrained to show only the area of velocity perturbations due to infiltration which is 9.5 m to 13.5 m laterally and from 0 to 3 m at depth. The largest range in the *P*-wave velocity perturbations observed in the tomograms after infiltration are from -100 m/s to -300 m/s (Figure 19). Due to the non-unique nature of tomographic inversion modeling and more broadly geophysical inversion modeling, we investigate the *P*-wave velocity perturbations over a range of velocity scales and contour intervals to observe the changes in visual characteristics of wetting front geometry and distribution with variable *P*-wave velocity constraints (Figures 20 - 24). We begin with the velocity range of -300 m/s to -100m/s because this range isolates the *P*-wave velocity anomaly without the presence of background noise which occurs with velocities greater than -100 m/s. The minimum velocity is set at -300 m/s because velocities less than this threshold are not observed in the infiltration area. From the initial interval we investigate ranges from -150 m/s to -300m/s, and -200 m/s to -300 m/s with contour intervals at 25 m/s and 50 m/s. The greatest *P*-wave

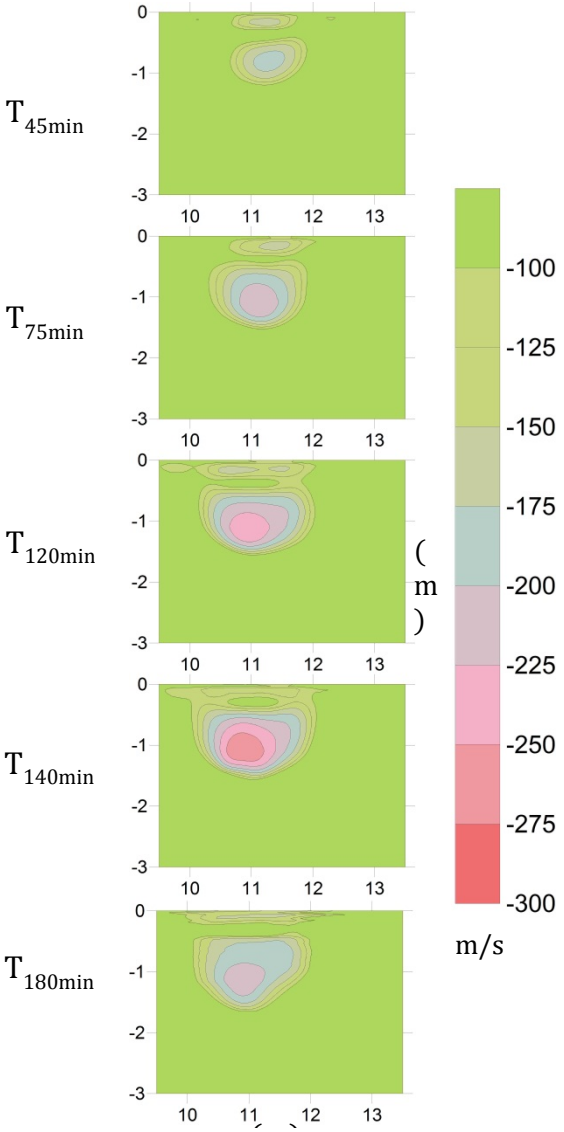

Figure 20: Discrete *P*-wave velocity profiles centered on the area of infiltration for the first constant flux applicator experiment with the velocity interval constrained to be from -300 m/s to -100 m/s and a contour interval of 25 m/s. A trend analysis has been applied to each of the profiles.

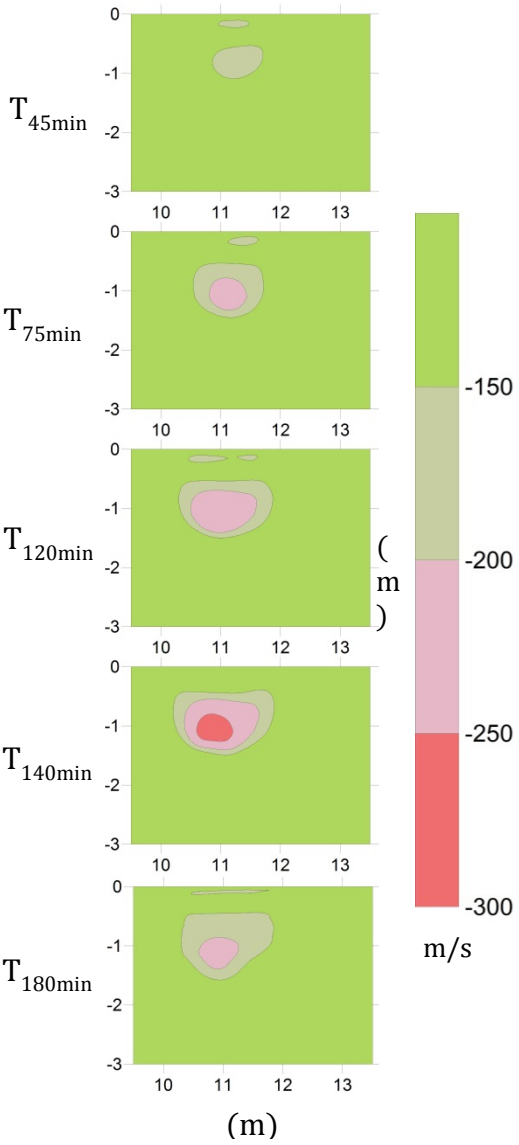

Figure 21: Discrete *P*-wave velocity profiles centered on the area of infiltration for the first constant flux applicator experiment with the velocity interval constrained to be from -300 m/s to -150 m/s and a contour interval of 50 m/s. A trend analysis has been applied to each of the profiles.

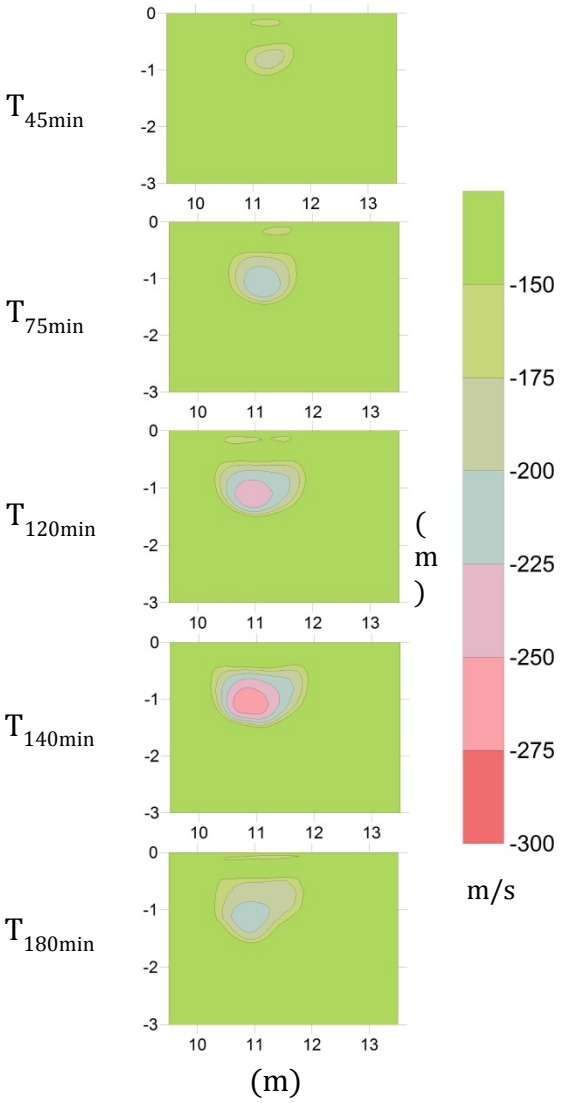

Figure 22: Discrete *P*-wave velocity profiles centered on the area of infiltration for the first constant flux applicator experiment with the velocity interval constrained to be from -300 m/s to -150 m/s and a contour interval of 25 m/s. A trend analysis has been applied to each of the profiles.

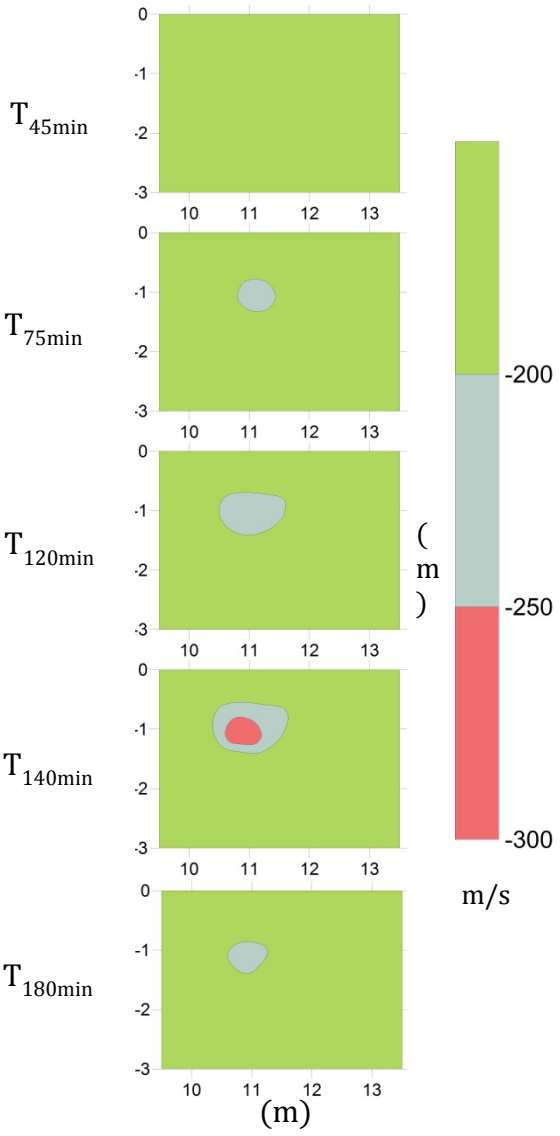

Figure 23: Discrete *P*-wave velocity profiles centered on the area of infiltration for the first constant flux applicator experiment with the velocity interval constrained to be from -300 m/s to -200 m/s and a contour interval of 50 m/s. A trend analysis has been applied to each of the profiles.

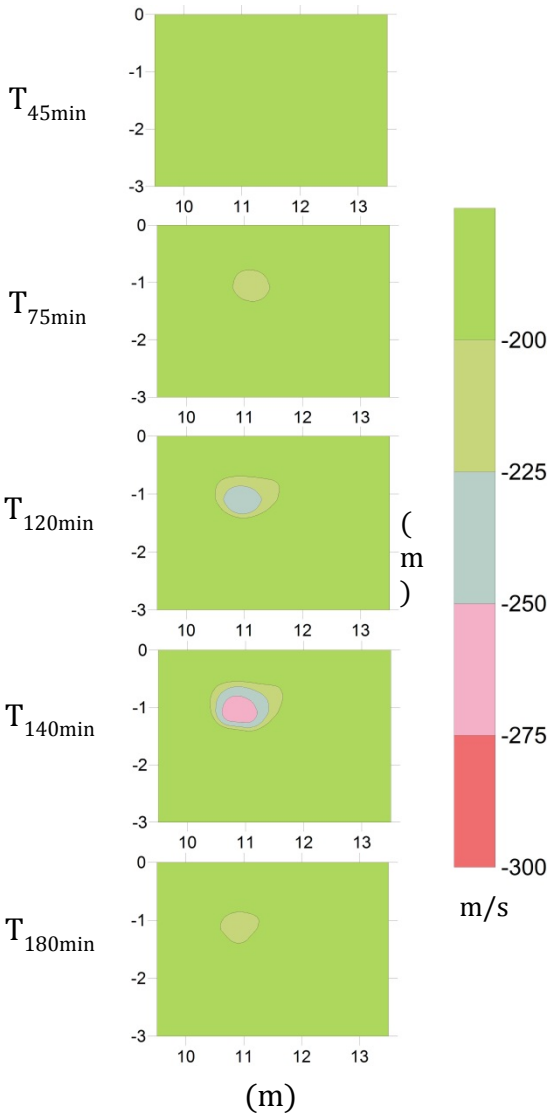

Figure 24: Discrete *P*-wave velocity profiles centered on the area of infiltration for the first constant flux applicator experiment with the velocity interval constrained to be from -300 m/s to -200 m/s and a contour interval of 25 m/s. A trend analysis has been applied to each of the profiles.

velocity anomaly is observed with a velocity interval from -300 m/s to -100m/s where the contour intervals of 25 m/s and 50 m/s provide additional information regarding *P*-wave velocity distribution within the wetting front (see Figure 19 and Figure 20).

The smallest *P*-wave velocity perturbation is observed with the velocity range of -200 m/s to -300 m/s, where the first time-step of 45 minutes is unable to resolve a wetting front or velocity changes relative to the adjacent material within this velocity range (see Figure 23 and Figure 24). With infiltration ending at the surface around 112 minutes, the time-step displaying the greatest anomaly in each of the previously mentioned velocity scales is the 140 minute time-step. In contrast, the smallest wetting front or *P*-wave velocity perturbation is observed at the 45 minute time-step.

3.6. Discussion and Conclusion

TLSFT is successful in imaging a migrating wetting front at five time-intervals during a surface infiltration experiment using a constant flux applicator. The *P*-wave velocity perturbations used as a proxy for relative changes in saturation (i.e. the advancing wetting front) provide an image characterizing the spatial and temporal distribution of the wetting front. The TLSFT method is a qualitative means of visualizing a migrating wetting front through the vadose zone. This method provides an understanding of subsurface structures and anisotropic features that control fluid flow that current methods investigating fluid movement in the vadose

zone are unable to provide. Furthermore, this method may be desirable over the current methods for quantifying fluid flow due to the methods ability to visually characterize the wetting front geometry and distribution. The *in-situ* surface infiltration methods (e.g. Amoozemeter or ring infiltrometer) which calculate fluid flow parameters based on measurements collected at the surface obtain a quantitative calculation of fluid flow, but they are unable to provide an understanding of how the wetting front advances spatially and with what geometry.

As with any method, there are both advantages and limitations relative to other methods. The advantage of using TLSFT to image a migrating wetting front from surface infiltration are the two-dimensional velocity profiles that can provide additional understanding of the subsurface by identifying any heterogeneous and/or anisotropic features that may be present at the site. An additional advantage of the TLSFT infiltration method to image a wetting front is that it is relatively non-invasive and robust. The planting of geophones and auguring a hole at the site of infiltration are the only means of disturbing the subsurface. As with most methods, auguring a hole is standard and only extends to approximately 0.5 m at depth. The geophones planted at the surface only penetrate the upper 0.10 m of the soil profile. These soil disturbances are far less invasive compared to drilling a well or auguring a large soil column for laboratory analysis.

A limitation of the TLSFT method using a constant flux applicator is the large volume of water required for infiltration to produce an observable seismic *P*-wave

velocity response. Additionally, determining which range of *P*-wave velocities and at which contour interval to define the boundary of the wetting front will require further investigations. There is however, a small range of velocities associated with the wetting front (200 m/s) when compared to range of the velocities that are observed within the profile, which is 2000 m/s at the deepest part of the profile.

In conclusion, the TLSFT method using a constant flux applicator is successful in imaging a migrating wetting front in the vadose zone. Using the proposed TLSFT infiltration method, estimates of anisotropy and qualitative assessments of the fluid migration can be used for a variety of disciplines. The visual characterization of wetting front geometry and distribution can be used for a wide variety of applications which require an understanding of fluid movement in the vadose zone to address problems such as waste disposal, construction of man-made structures (e.g. bridges and highways), natural resource management, and a multitude of other agricultural and engineering investigations.

4. CALCULATING FIELD-SATURATED HYDRAULIC CONDUCTIVITY IN THE VADOSE ZONE USING SURFACE TIME-LAPSE SEISMIC FIRST-ARRIVAL TOMOGRAPHY

This chapter is based on a paper that is in preparation by Rachel Elizabeth Storniolo, Gregory S. Baker, Ed Perfect, and Jaehoon Lee to be submitted to the Vadose Zone Journal. Note: Some material covered in this chapter is repeated from within the previous introduction and background chapters in order to exist in a stand-along publishable format.

Abstract

Quantifying and characterizing fluid migration in the vadose zone is critical in addressing a variety of engineering and agricultural problems. Furthermore, the distribution of a fluid as it migrates into the subsurface is considered equally important in characterizing the fluid flow. Two infiltration experiments were conducted at the B-4 plot of the East Tennessee Research and Educational Center (ETREC), one using a constant flux applicator and one using a constant head permeameter. The constant flux applicator infiltration experiment was conducted in order to obtain time-variant images of a migrating wetting front generated by surface infiltration using time-lapse seismic first-arrival tomography (TLSFT). The constant head permeameter (Amoozemeter) infiltration experiment was conducted to obtain hydraulic conductivity values for the quantitative assessment of fluid flow at the site. An initial infiltration experiment using a constant flux applicator at the ETREC B-4 plot determined that the TLSFT infiltration method is successful in resolving *P*-wave velocity perturbations in the shape of a wetting front at different

time-steps (see Chapter 3). Additional TLSFT infiltration experiments were conducted to image the migrating wetting front and use the geometry of the resulting ellipsoidal *P*-wave velocity anomaly to calculate hydraulic conductivity. The objective of calculating hydraulic conductivity using TLSFT during an infiltration experiment is to quantitatively compare the TLSFT infiltration method to a commonly used *in-situ* surface infiltration method (e.g. Amoozemeter). Geometry of the wetting front and surface infiltration parameters (i.e. volume and outflow rates) were used to empirically calculate field-saturated hydraulic conductivity. A constant flux applicator was used to infiltrate water into the subsurface while concurrently collecting TLSFT data. Changes in seismic *P*-wave velocities were observed in the area of infiltration and are used as a proxy for relative changes in saturation from a migrating wetting front generated from surface infiltration. The volume of water infiltrated, outflow rate of infiltration, and wetting front geometry at different time-steps during the constant flux applicator infiltration experiment were recorded and later used to calculate field-saturated hydraulic conductivity. A constant head permeameter (Amoozemeter) infiltration experiment was also performed at the B-4 plot to calculate field-saturated hydraulic conductivity. The constant head permeameter method is a popular instrument used to calculate field-saturated hydraulic conductivity *in-situ*. The field-saturated hydraulic conductivity calculations from the TLSFT infiltration method and constant head permeameter method were obtained for a means of quantitative comparison between the two. This aided in investigating the ability of the TLSFT infiltration method to provide

computable values for rate of transport, in addition to the visual characterization of the migrating fluid. In addition to the success of imaging the migrating wetting front, the TLSFT infiltration method using a constant flux applicator produced K_{fs} calculations that are within one to two orders of magnitude to those K_{fs} values calculated using the Amoozemeter infiltration experiment as well as known K_s values of the Sequatchie soil series. The quantitative calculations of K_{fs} using the TLSFT infiltration method with a constant flux applicator were employed for comparison to standard methods that investigate fluid-flow in the vadose zone. Although the K_{fs} calculations using the TLSFT method were within one to two orders of magnitude of the Amoozemeter calculations and K_s of the Sequatchie series, the range of calculated K_{fs} using the TLSFT infiltration method are reasonable ranges when considering the spatial and temporal variability of soil type, water saturation, and consequently K_{fs} at a single site. The TLSFT method for quantification purposes will require refining to obtain more accurate K_{fs} values.

4.1. Introduction

Characterizing and understanding vadose zone parameters and processes are critical for identifying and resolving problems in the near surface. Investigating the shallow subsurface using geophysical techniques has become an increasingly popular means of exploring and assessing vadose zone properties and mechanisms due to its non-destructive nature. Seismic first-arrival tomography (SFT) is a common geophysical technique that is both robust and applicable for a variety of

hydrological investigations (e.g. locating perched water tables, identifying karst features, and locating the water table).

4.1.1. Motivation

Time-lapse seismic first-arrival tomography (TLSFT) has been used to successfully image a migrating wetting front in the vadose zone (see Chapter 3). A second set of infiltration experiments were performed to demonstrate the method's ability to reproduce an image of a migrating wetting front using a smaller volume of water infiltrated, in addition to calculating field-saturated hydraulic conductivity as a means of quantifying fluid migrating using the TLSFT infiltration method. Quantitative values representing fluid flow in the vadose zone, such as hydraulic conductivity are valuable for calculating variables such as residence times in reservoirs, as well as seepage rates from dams and waste retention ponds. While there is a need for obtaining quantitative assessments of fluid flow in the vadose zone, these variables or parameters are often calculated using surface measurements that may not provide a comprehensive understanding of fluid flow and distribution in the subsurface. For example, if a clay lens or vertical fracture exists at a site, surface measurements used to calculate hydraulic conductivity are dominated by these structures and the result is a misrepresentation of the sites effective hydraulic conductivity.

4.1.2. Objective

Two separate infiltration experiments were conducted to obtain values of calculated field-saturated hydraulic conductivity. The first infiltration experiment used a constant flux applicator to infiltrate water into the subsurface, while TLSFT data was collected simultaneously. The geometry of the ellipsoidal *P*-wave velocity perturbations observed in each of the time variant velocity profiles were used to empirically calculate field-saturated hydraulic conductivity using formulae presented by Schwartzman and Zur (1987). The constant flux applicator was refined from previous investigations (see Chapter 3) by detailing the volume infiltrated and outflow rate of water during the experiment, in addition to reducing the overall volume of water infiltrated.

A second infiltration experiment was conducted using a constant head permeameter (Amoozemeter) to infiltrate water while simultaneously collecting TLSFT data. The calculation of hydraulic conductivity was the priority of the Amoozemeter infiltration experiment; TLSFT data collected during the Amoozemeter experiment were not expected to produce observable velocity perturbations due to the overall small volume of water infiltrated.

The Amoozemeter is a compact constant head permeameter (CCHP) field instrument used for the *in-situ* measurement of saturated hydraulic conductivity via surface infiltration. The Amoozemeter is considered to be a common instrument and standard method employed by a variety of scientific disciplines to obtain *in-situ*

measurements of saturated hydraulic conductivity. To clarify, we consider saturated hydraulic conductivity that is measured via infiltration into an initially unsaturated soil, to be referred to as field-saturated hydraulic conductivity based on Reynolds et al. (1983).

4.2. Background

The use of geophysical techniques to investigate and characterize near-surface processes is advantageous to many invasive or destructive methods (e.g. drilling wells for pump tests and auguring cores for laboratory analysis). We use seismic first-arrival tomography to provide a velocity model of the vadose zone using measured travel-time information collected at the surface. First, a seismic source is generated where compressional waves (*P*-waves) propagate through the subsurface and later return to surface where sensors (or geophones) record their arrival times. Seismic first-arrival tomography measures positional changes in *P*-wave velocities as they encounter boundaries (e.g. water table) and/or varying material properties (e.g. changes in porosity or water saturation) in the subsurface. The *P*-wave velocities speed or slow depending on subsurface materials and the arrival-times are measured at the surface. Compressional waves (*P*-waves) are used because they are the fastest traveling waves, therefore the first to arrive on the seismographs.

The generalized processing procedure for various tomographic algorithms begins with picking the first arrivals off a seismograph and developing an initial forward model. The initial model is then iteratively updated with the measured

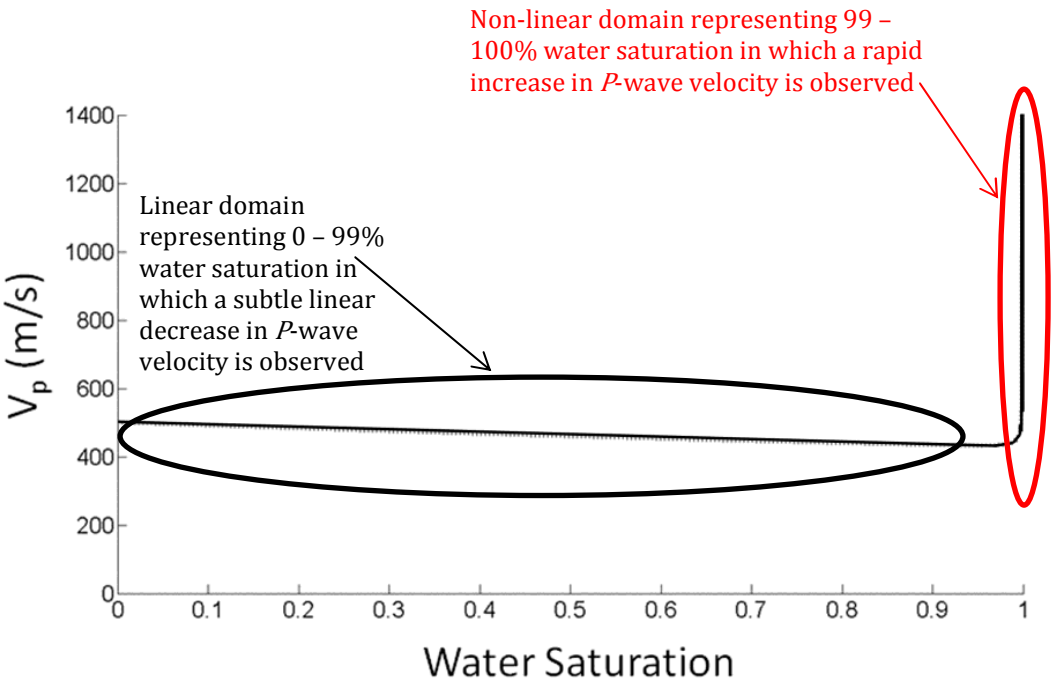

Figure 25: A graph displaying *P*-wave velocity and water saturation relationship according to the Gassman equation containing short descriptions for the linear and non-linear domains.

travel-time data until they meet a specified convergence criteria (e.g. Schuster and Quintus-Bosz, 1993; Zhang and Toksoz, 1998). The collection of surface seismic data at different time-steps allows us to observe the effect of temporal and spatial variations in seismic *P*-waves as water infiltrates downward from the surface, generating a wetting front in the localized region of infiltration.

The response of seismic velocity to pore fluids and percent saturation has been a petrophysical subject of interest for decades in many theoretical (Gassman, 1951; Biot, 1956) and experimental investigations (Murphy, 1982). In recent decades, seismic methods are becoming widely utilized in investigating near-surface problems (Bachrach and Nur, 1998; Steeples and Miller, 1998; Zimmer et al., 2007). In regards to hydrogeology, seismic reflection and refraction methods have been successful in locating and mapping the water table (Haeni, 1986; Bachrach and Nur, 1998; Chapter 3), locating perched water bodies (Gaines, 2011), and monitoring temporal and spatial variations of *P*-wave velocities during a infiltration event (Gaines, 2011; Chapter 3).

Water content variations in the vadose zone affect the soil's density and effective bulk modulus; therefore, producing changes in seismic *P*-wave velocity (Figure 25). The mathematical relationship between density, effective bulk modulus, and saturation have been documented (Domenico, 1974; Mavko et al., 1995; Bachrach and Nur, 1998) and later investigated in laboratory experiments (George et al., 2009). The effect of saturation on *P*-wave velocity is somewhat complex but can be broadly categorized into two domains, the linear and non-linear

(Domenico, 1974; Mavko et al., 1995; Bachrach and Nur, 1998). For our experiment, we only observe saturation values below a 99% threshold which are associated with the linear domain following the Gassman equation. The linear domain is comprised of a variable saturated porous media (i.e. soil in the vadose zone) and result in a gradual *P*-wave velocity decrease with increasing saturation.

The most common variable used to quantify fluid flow is hydraulic conductivity. Darcy's Law describes the steady-state transmission of water through a variably-saturated granular porous media (Equation 6):

$$q = K\Delta H/L \qquad \text{(Equation 6)}$$

where q(L/T) is the flux density or simply flux (i.e. the volume of water flowing through a unit cross-sectional area per unit time *t*), K(L/T) is (saturated) hydraulic conductivity, and ΔH/L is the head drop per unit distance in the direction of flow known as the hydraulic gradient.

When saturated hydraulic conductivity is measured by infiltration into an initially unsaturated soil, it is commonly referred to as field-saturated hydraulic conductivity (Reynolds et al., 1983). This is due to the recognition of the fact that air is usually entrapped in the porous medium when "saturated" by infiltrating water, particularly in the case of downward infiltration under ponded conditions. Consequently, the water content of the porous medium at field saturation is lower than that of complete or true saturation (Hillel, 1980).

Field-saturated hydraulic conductivity is often considered more appropriate in vadose zone applications. The concept of field-saturated hydraulic conductivity follows more natural and human-induced infiltration processes (e.g., rainwater infiltration, drip and sprinkler irrigation, and waste water disposal) where air can become entrapped in the porous media (Bouwer, 1978). There are several methods to obtain *in-situ* estimates of saturated and field-saturated hydraulic conductivity in the vadose zone.

The compact constant head permeameter (i.e. Amoozemeter) is a popular instrument used to obtain calculations of saturated hydraulic conductivity. Additional methods include various ring or pressure infiltrometers as well as borehole or well permeameter methods (Dane and Topp, 2002).

4.3. Experiment Site Description

The constant flux applicator and constant head permeameter infiltration experiments, along with TLSFT data acquisition, were conducted at the East Tennessee Research and Education Center (ETREC) plot B-4 (Figure 26). The ETREC is located approximately two miles south of The University of Tennessee's main campus in Knoxville, Tennessee. The general region lies within the Valley and Ridge Province consisting of northwest trending ridges and rock exposures from the Cambrian, Ordovician, and Silurian geologic systems (Roberts, 1955). The alluvium deposits are composed of weathered materials originating from shales, limestones, sandstones, and metamorphosed micaceous rock (Roberts, 1955).

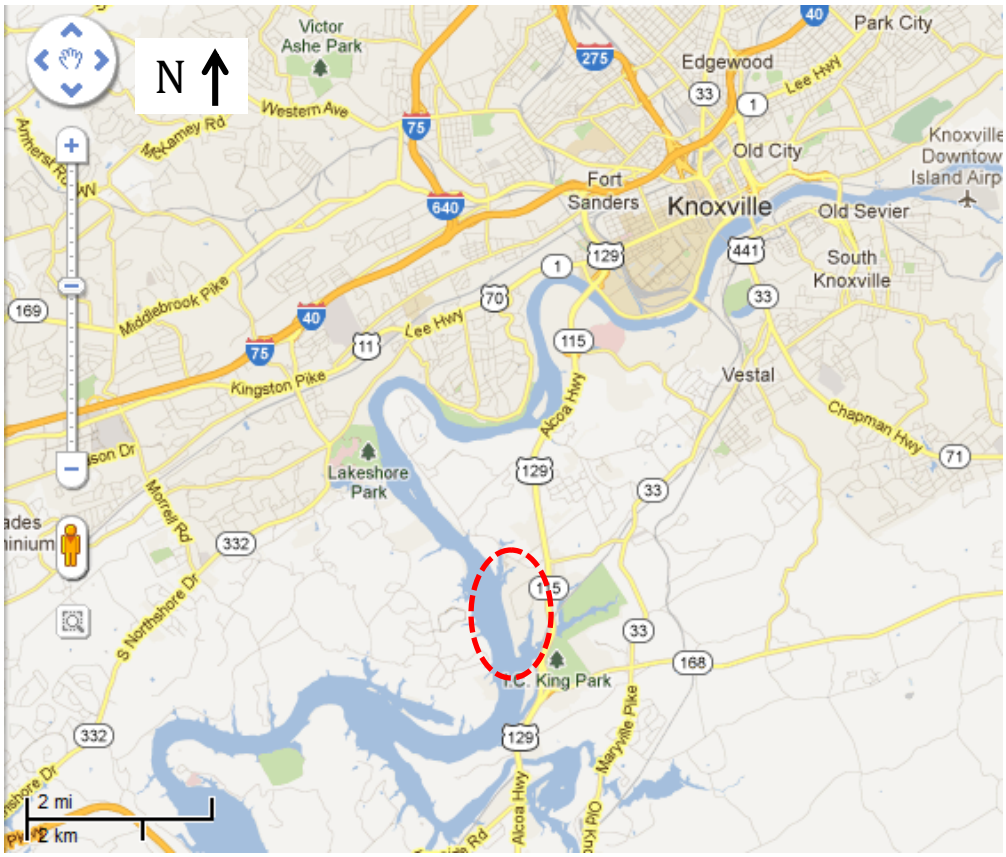

Figure 26: Google Earth ™ image of Knoxville, TN and the relative location of the EATREC B-4 plot location outlined by the red dotted circle.

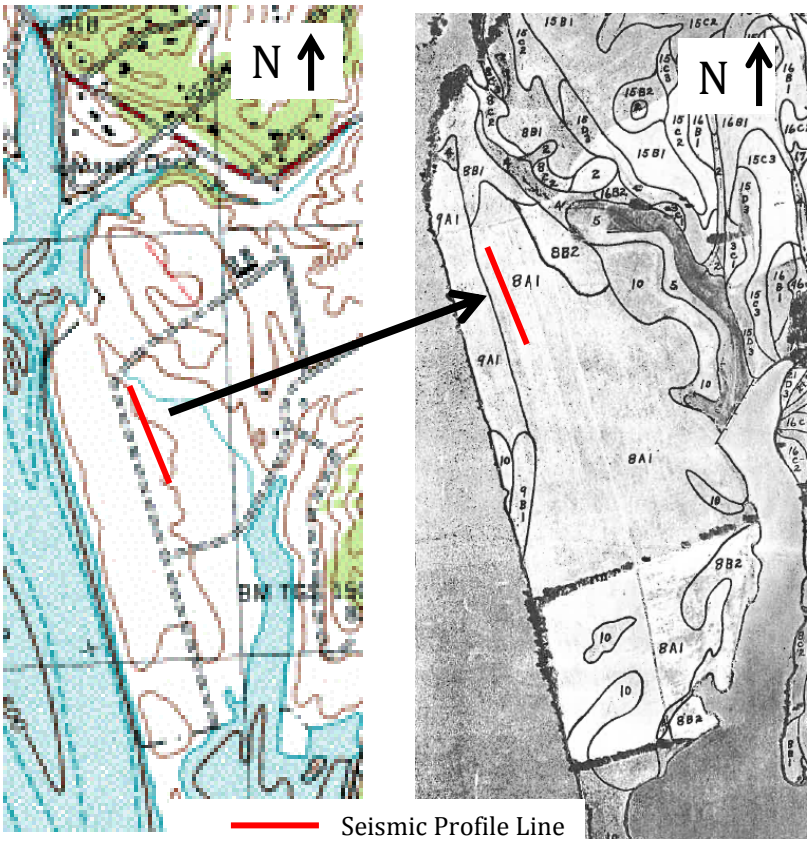

Figure 27: Topographic map (left image) and soil map (right image) showing the location of the ETREC B-4 plot. The seismic profile line is approximated by the red line. The topographic image is obtained from www.TNGIS.org and the soil map was created by Elder and Springer, 1963.

The B-4 plot is located on the t-1 alluvial terrace of the Tennessee River, where the average water table depth is at 2 m. The site contains soil from the Sequatchie series (8A1), based on soil survey conducted in 1963 by Elder and Springer and more recently by Leao, 2009 (Figure 27). The Sequatchie series (S_A) is comprised of very deep, well drained, moderately permeable soils that formed in loamy alluvium. The initial constant flux applicator infiltration experiment (see Gaines, 2011; Chapter 3) was conducted in the early fall of 2010 at this exact location.

4.4. Data collection

The constant flux applicator and Amoozemeter infiltration experiments, along with TLSFT data acquisition, were conducted in the summer of 2012. The acquisition and processing of the surface seismic data for the constant flux applicator and Amoozemeter infiltration experiments were identical, unless otherwise noted. The surface seismic data was collected along a 24 m profile transect, where a total of 48 geophones were planted at 0.5 m increments (beginning at 0 m and ending at 23.5 m). The geophones record vertical ground displacement and at a frequency bandwidth of 40 Hz. A sledge hammer and metal strike-plate were used for generating a seismic source at each shot-point along the profile. A total of 13 shot points were collected at 2 m increments along the profile, beginning at -0.5 m and ending at 23.5 m. Time zero began when the acquisition board was triggered by the pressure of the sledge hammer making contact with the metal strike-plate. The geophones then record the arrival times of seismic *P*-waves along the profile. At each shot point, the data were stacked variably (averaging 3

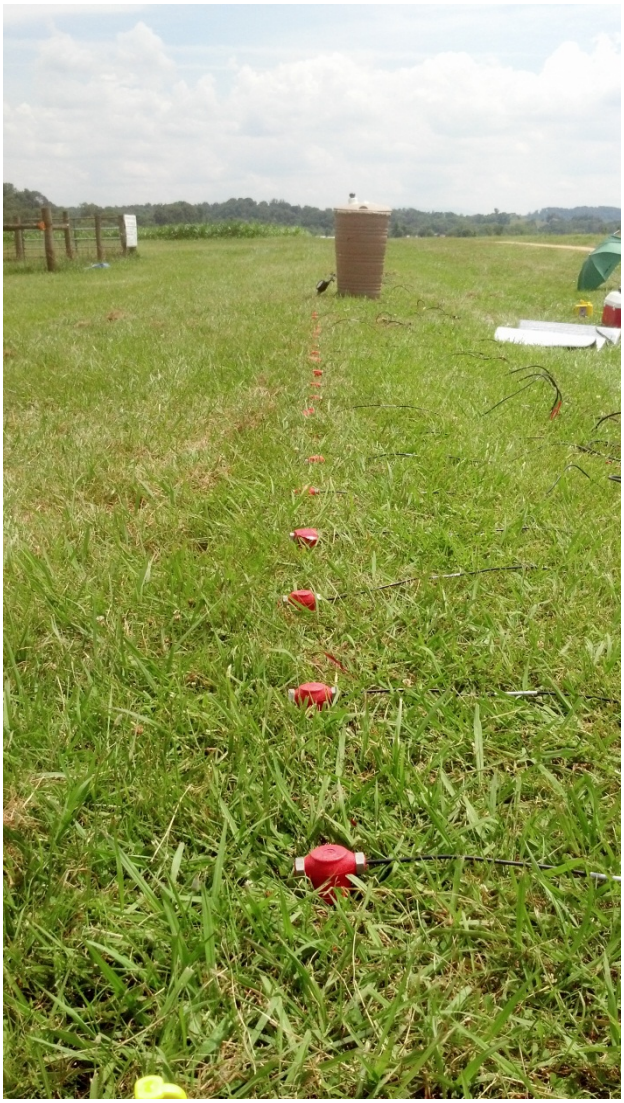

Figure 28: Photograph of the profile transect at the B-4 plot with seismic equipment employed for the second constant flux applicator infiltration experiment. The red geophones can be seen in the foreground and the green plastic barrel is located in the middle of the profile transect.

Figure 29: Photograph of the second constant flux applicator apparatus used for the infiltration experiment. The plastic barrel was centered along the profile transect, and the hose was used to infiltrate water into augured well.

Table 1: Infiltration parameters recorded in the field at each time-step for the constant flux applicator infiltration experiment.

INFILTRATION FIELD PARAMETERS FOR CONSTANT FLUX APPLICATOR		
Time (minutes)	Qutflow, q (m^3/s)	Cumulative Volume, V (m^3)
15	2.98E-05	0.025
45	2.79E-05	0.075
75*	2.73E-05	0.106
105*	2.73E-05	0.106
135*	2.73E-05	0.106

* Note infiltration has ended at these time-steps therefore we average of outflow rate (q) during the experiment. We average the q values in order to calculate K_{fs} using Schwartzman and Zur (1987).

stacks at each shot point location) depending on signal-to-noise ratio observed during data collection.

The constant flux applicator (modified plastic rain barrel) was used to infiltrate water. The barrel was filled with approximately 130 L (0.130 m^3) of water and placed at the center of the 24 m profile transect (Figure 28). A flow meter was fastened to the hose outlet at the bottom of the plastic barrel in order to periodically measure outflow volume during infiltration (Figure 29). The constant flux applicator was located laterally along the profile at 12 m (i.e. at the center of the 24 m profile transect). For the infiltration of water, a cylindrical hole was augured with a diameter of 0.05 m and to a depth of 0.5 m. The rate of infiltration was controlled by periodically observing the outflow volumes off the flow meter. A total of 106 L was infiltrated over a period of 64 minutes. Moderate ponding at the surface began to occur at approximately 30 minutes after infiltration (i.e. time=0) due to the higher rate of outflow discharge relative to the soil's ability to uptake the water. The flow meter was fastened to the outflow spigot at the base of the constant flux applicator apparatus. The cumulative volume (V) and outflow (q) rates were measured in the field and recorded at each time-step (Table 1). At each time-interval throughout the experiment, the outflow water volume was recorded and outflow rate was calculated by dividing the outflow volume per unit time. At the time-steps after infiltration had ended (T_{75min}, T_{105min}, and T_{135min}), the volume

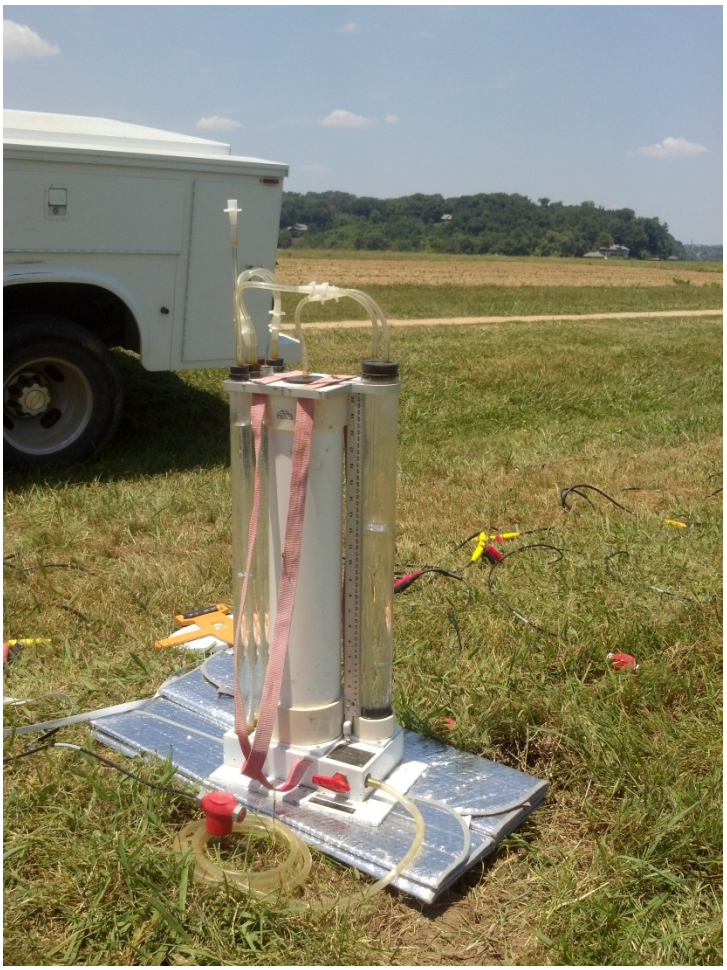

Figure 30: A photograph of the Amoozemeter (CCHP) employed in the field at the center of the profile transect at the ETREC B-4 plot.

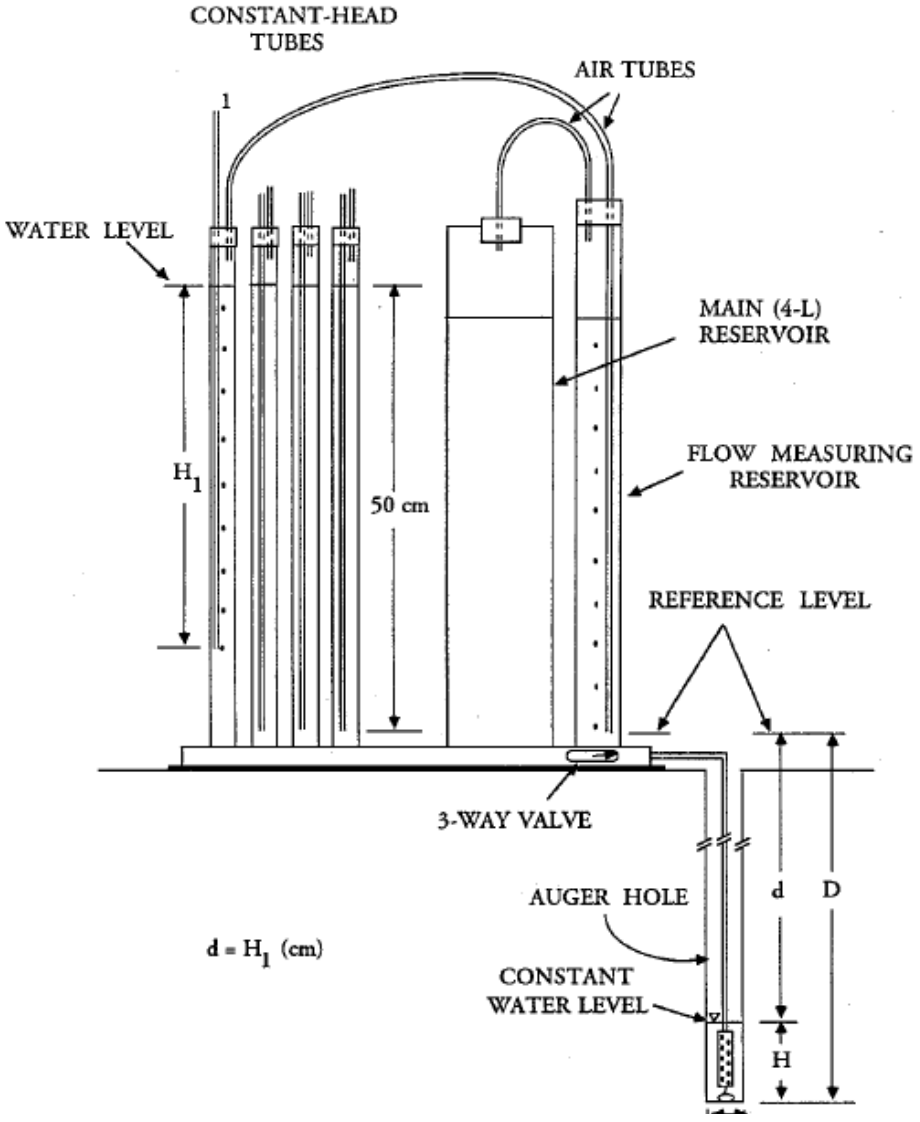

Figure 31: Schematic representation of the Amoozemeter (CCHP) components and parameters measured and recorded in the field. The measurements and recorded values are later used for calculating K_{sat} (K_{fs}). Image from CCHP Manual (Ksat Inc.)

recorded was the cumulative volume infiltrated and the outflow rates were an average of the calculated outflow rates obtained during infiltration (see Table 1).

A compact constant head permeameter (CCHP), widely known as the Amoozemeter, was used to estimate *in-situ* saturated hydraulic conductivity at the ETREC B-4 plot (Figure30). As previously mentioned, we use the term field-saturated hydraulic conductivity when saturated hydraulic conductivity is measured via infiltration into in an initially unsaturated soil. The Amoozemeter is a constant head well permeameter method that is based on quasi-steady infiltration obtained by ponding a head of water in a cylindrical borehole or "well" augured into the vadose zone (Reynolds et al., 1983, 1985; Amoozegar, 1989).

The Amoozemeter requires a two-step technique: (1) obtain quasi-steady state flow from cylindrical auger hole under constant head of water in the field, and (2) use field data to calculate field-saturated hydraulic conductivity. The parameters collected in the field were: augured well depth (D), ponded head height in augured well (H), height of water in constant head bubbling tube (H_1), diameter of augured hole (2r), change in water level in flow measuring reservoir, and time(Figure 31).

The Amoozemeter was placed in the center of the surface seismic profile transect at a lateral location of 12 m. The instrument was leveled and a 0.05 m diameter cylindrical well was augured to a depth of 0.5 m. The water level in the bubbling tube (H_1) was adjusted to 0.37 m, which corresponded to the ponded head level (H) in the augured hole at 0.15 m, which accounted for a reference level of 0.02

cm. The area (A) of the cylindrical flow measuring reservoir was known and volume was calculated by multiplying area, A, with the drop in water level from the flow measuring reservoir. Elapsed time was recorded along with periodic readings from the change in water level in the flow measuring reservoir. The volume change calculated per unit time yielded the outflow discharge (Q) into the augured well. A field notebook contains records of elapsed time, drop in water level in flow measuring reservoir, and the calculation of Q at each time step recorded.

The two constant head tube chambers obtained a quasi-steady state discharge rate which was approximately $7x10^{-7}$ m^3/s (0.0052 m^3/hr). To calculate field-saturated hydraulic conductivity (or K_{sat} as referred to in manual), first the outflow was calculated using the following form of Darcy's equation (Equation 7) with the data collected in the field:

$$Q = \frac{dA}{T} \qquad \text{(Equation 7)}$$

where $Q(L^3/t)$ is the outflow per unit time, d(L) is the drop in water level, and $A(L^2)$ is the area of the reservoir cylinder which is 105 cm^2 for both reservoirs (i.e. valve is turned to "2 on"), and T(t) elapsed time since previous reading.

In the second step of obtaining an estimate of field-saturated hydraulic conductivity, using Glover's solution (Equation 8) we transformed Q into K_{sat} (Amoozegar, 1989):

$$K_{sat} = Q\left\{\frac{\left[sinh^{-1}\left(\frac{H}{r}\right)-\left(\left(\frac{r}{H}\right)^2+1\right)^{\frac{1}{2}}+\left(\frac{r}{H}\right)\right]}{2\pi H^2}\right\} \qquad \text{(Equation 8)}$$

where Q(L^3/t) is outflow per unit time, H(L) is constant head in borehole, r(L) is borehole radius, and $sinh^{-1}$ is the hyperbolic sine function, and π is pi.

The Amoozemeter was employed in the field for two days (32 hr) where periodic increments of time had elapsed in which the instrument was not discharging water into the augured hole. In other words, the reservoir had emptied in the middle of the night and was not able to be refilled until the morning. In such case, the emptied reservoir was refilled and with time quasi-steady state was able to be reinstated. Over the period of 32 hours approximately 0.015 m^3 (15 L) of water was discharged into the subsurface.

Surface seismic data was collected prior to constant head permeameter infiltration experiment, as the baseline or background profile. An additional three TLSFT profiles were collected during the 32 hours of infiltration. The baseline TLSFT profile (CH_B) was acquired prior to infiltration. The three profiles collected during the Amoozemeter infiltration experiment were CH1 at T_{410min} (6 hr 50 min), CH2 at $T_{1320min}$ (22 hr), and CH3 at $T_{1920min}$ (32 hr).

4.5. Methods and Analysis

A total of six TLSFT profiles were collected on the same day during the constant flux applicator infiltration experiment. The first was a background or baseline profile collected prior to infiltration. Five subsequent profiles were

collected at approximately 30 minute intervals after infiltration began to monitor the seismic *P*-wave velocity response to surface infiltration. The five seismic profiles representing time after the commencement of infiltration were acquired at the following time-steps; 15 min, 45 min, 75 min, 105 min, and 135 min.

First-arrival times were manually selected off of the seismographs acquired in the field. Travel time data was then imported into Rayfract™ for tomographic inversion modeling. Using the first-arrival times, an initial smooth 1-D model was generated by back-projecting traveltime residuals and solving the eikonal equation to determine raypaths (Lecomte et al., 2000). The initial gradient model was updated iteratively using measured travel times until convergence (Schuster and Quintus-Bosz, 1993).

The smooth 1-D initial gradient model was generated using the first-arrival times of the baseline profile. The initial gradient model was a simplified representation of the velocity structure of the field site, showing a gradual increase in velocity with depth as well as an accurate location of the water table outlined by a red dotted line (Figure 32). The depth of the water table was located by identifying the rapid increase in *P*-wave velocity due to the values of saturation approaching 100%.

The interactive WET algorithm in Rayfract™ Software was used to generate the final 2-D velocity profiles for each of the five-time steps collected after infiltration had begun. The initial baseline gradient model was used as the initial model for each of the five subsequent (infiltration) velocity profiles. The first-

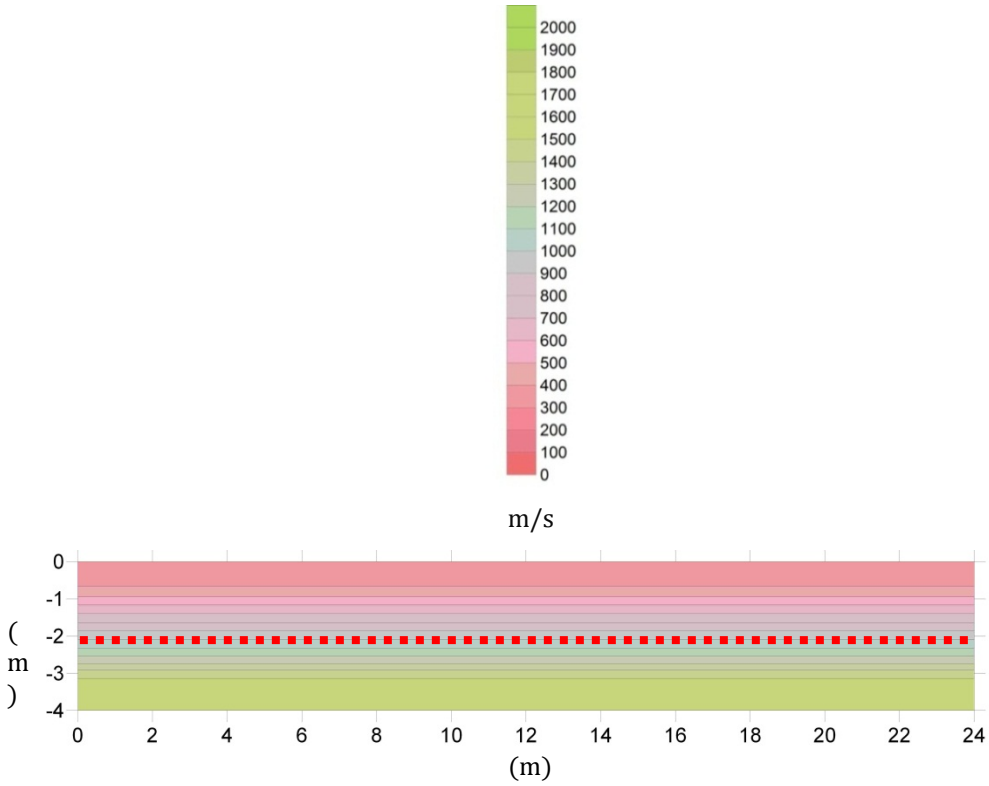

Figure 32: Initial gradient velocity model of baseline profile for the TLSFT infiltration experiment with the location of the water-table highlighted by a red dotted line. The unit is *P*-wave velocity in meters per second with a contour interval of 100 m/s.

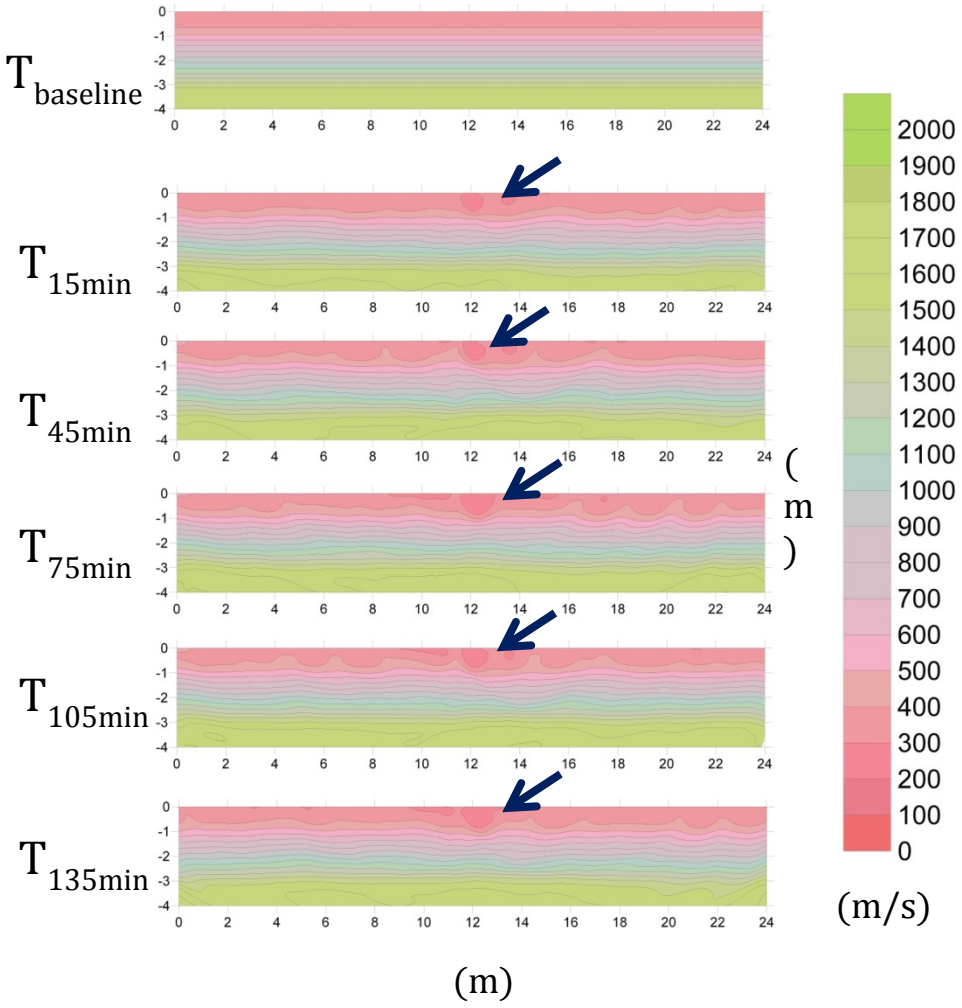

Figure 33: The six *P*-wave velocity tomograms of the second constant flux applicator TLSFT infiltration experiment at the ETREC B-4 plot. The first panel is the baseline profile prior to infiltration and the following profiles were collecting after infiltration has begun. The unit is measured in *P*-wave velocity in meters per second with a contour interval of 100 m/s. The blue arrows identify the low-velocity anomalies associated with water infiltration from the surface.

arrival times from each of the respective five profiles were used with the baseline gradient model to iteratively update until a specified convergence to produce the final 2-D velocity profiles (Figure 33). The use of the baseline gradient model and the initial model for each subsequent profile will slightly reduce processing artifacts, as well as enhance the changes in velocity with respect to the baseline as the infiltration experiment progresses with time.

In contrast to the first constant flux applicator experiment conducted in the fall of 2010, the constant flux applicator TLSFT infiltration profiles did not require a trend analysis to isolate the ellipsoidal velocity perturbation (i.e. wetting front) at each time-step. The velocity scales for each of the five time-steps were adjusted to a velocity range of 100 m/s to 300 m/s which was the observed velocity range of the ellipsoidal perturbations. This eliminated background noise from the velocity profiles not associated with infiltration. Additionally, the area for each of the profiles was constrained to show only the area of infiltration (i.e. 11 m to 13 m laterally and to a depth of 2 m) to display images of the isolated wetting front at each time-step (Figure 34). The objective of quantitatively comparing the TLSFT infiltration method (using the constant flux applicator), with standard methods used to investigate fluid flow in the vadose zone, required the extraction of the wetting front geometry from the velocity profiles to calculate field-saturated hydraulic conductivity using empirical formulae.

First we addressed the question of which velocity contour to use in defining the boundaries of the wetting front. The boundaries of the isolated velocity

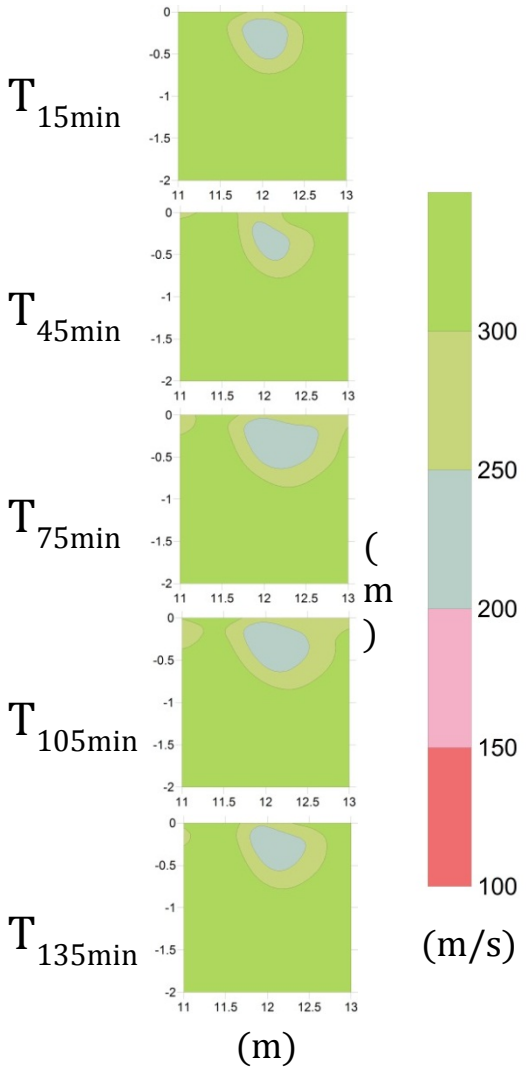

Figure 34: Discrete *P*-wave velocity profiles at the area of injection for the second constant flux applicator TLSFT infiltration experiment. The velocity profiles do not have any trend analysis applied and the velocity interval is constrained to show only the velocity perturbations observed within the area of infiltration 100 m/s to 300 m/s.

perturbations were later used to measure width and depth of wetting front for the calculation of K_{fs}. The velocity perturbation was observed from 100 m/s to 300 m/s (pre- trend analysis) in the first TLSFT constant flux applicator experiment conducted in the fall of 2010 as well as the TLSFT constant flux applicator experiment in the summer of 2012.

Using a contour interval of 50 m/s, two isolated ellipsoidal velocity perturbations were observed at 250 m/s and 200 m/s velocity contours. The boundaries of the 250 m/s and 200 m/s velocity contours were used for determining width and depth of wetting front. We derived additional width and depth values from the empirical formulae presented by Schwartzman and Zur (1987) to compare with our observations. We back-calculated the expected width (Equation 9) and depth (Equation 10) for each time-step in the constant flux applicator infiltration TLSFT experiment using infiltration parameters observed in the field and known saturated hydraulic conductivity of the Sequatchie soil series at the site (Leao, 2009).

The equations derived from Schwartzman and Zur (1987) describe the empirical relationship between wetted width, d(L), volume of water, $V(L^3)$, emitter discharge (or outflow rate), $q(L^3/T)$, and wetted depth, z(L), for the given soil hydraulic conductivity, $K_s(LT^{-1})$ as follows:

$$d = 1.82V^{0.22}\left(\frac{K_s}{q}\right)^{-0.17} \quad \text{(Equation 9)}$$

$$z = 2.54V^{0.63}\left(\frac{K_s}{q}\right)^{0.45} \quad \text{(Equation 10)}$$

Table 2: Measurements of wetting front width and depth, as well as calculations of K_{fs} and change in water saturation ($\Delta\theta$) for each time-step during the constant flux applicator TLSFT infiltration experiment. The width and depth are measured from the 250 m/s and 200 m/s velocity contours. The "back-calculated" width and depth values are calculated using Schwartzman and Zur (1987) formulae.

CONSTANT FLUX APPLICATOR INFILTRATION TIME-STEPS		Width, d (m)	Depth, z (m)	Δθ Width	Δθ Depth	K_{fs}
15 minutes	back-calculated	1.090	0.126	0.040	> ϕ	5.79E-06
Cummulative Volume, V = 0.027 m^3	$V_{250\ m/s}$	0.895	0.737	0.072	0.129	7.01E-05
Outflow, q =2.98E-05 m^3/s	$V_{200\ m/s}$	0.526	0.484	0.354	> ϕ	2.24E-04
45 minutes	back-calculated	1.350	0.247	0.059	> ϕ	5.79E-06
Cummulative Volume, V = 0.076 m^3	$V_{250\ m/s}$	0.863	0.789	0.226	0.295	7.87E-05
Outflow, q =2.79E-05 m^3/s	$V_{200\ m/s}$	0.411	0.389	> ϕ	> ϕ	3.54E-04
75 minutes	back-calculated	1.446	0.308	0.067	> ϕ	5.79E-06
Cummulative Volume, V = 0.106 m^3	$V_{250\ m/s}$	1.442	0.853	0.068	0.327	1.76E-05
Outflow, q =2.73E-05 m^3/s	$V_{200\ m/s}$	0.874	0.568	0.304	> ϕ	5.23E-05
105 minutes	back-calculated	1.446	0.308	0.067	> ϕ	5.79E-06
Cummulative Volume, V = 0.106 m^3	$V_{250\ m/s}$	1.474	0.863	0.063	0.315	1.67E-05
Outflow, q =2.73E-05 m^3/s	$V_{200\ m/s}$	0.737	0.568	> ϕ	> ϕ	8.76E-05
135 minutes	back-calculated	1.446	0.308	0.067	> ϕ	5.79E-06
Cummulative Volume, V = 0.106 m^3	$V_{250\ m/s}$	1.053	0.779	0.174	> ϕ	4.15E-05
Outflow, q =2.73E-05 m^3/s	$V_{200\ m/s}$	0.642	0.484	> ϕ	> ϕ	1.12E-04

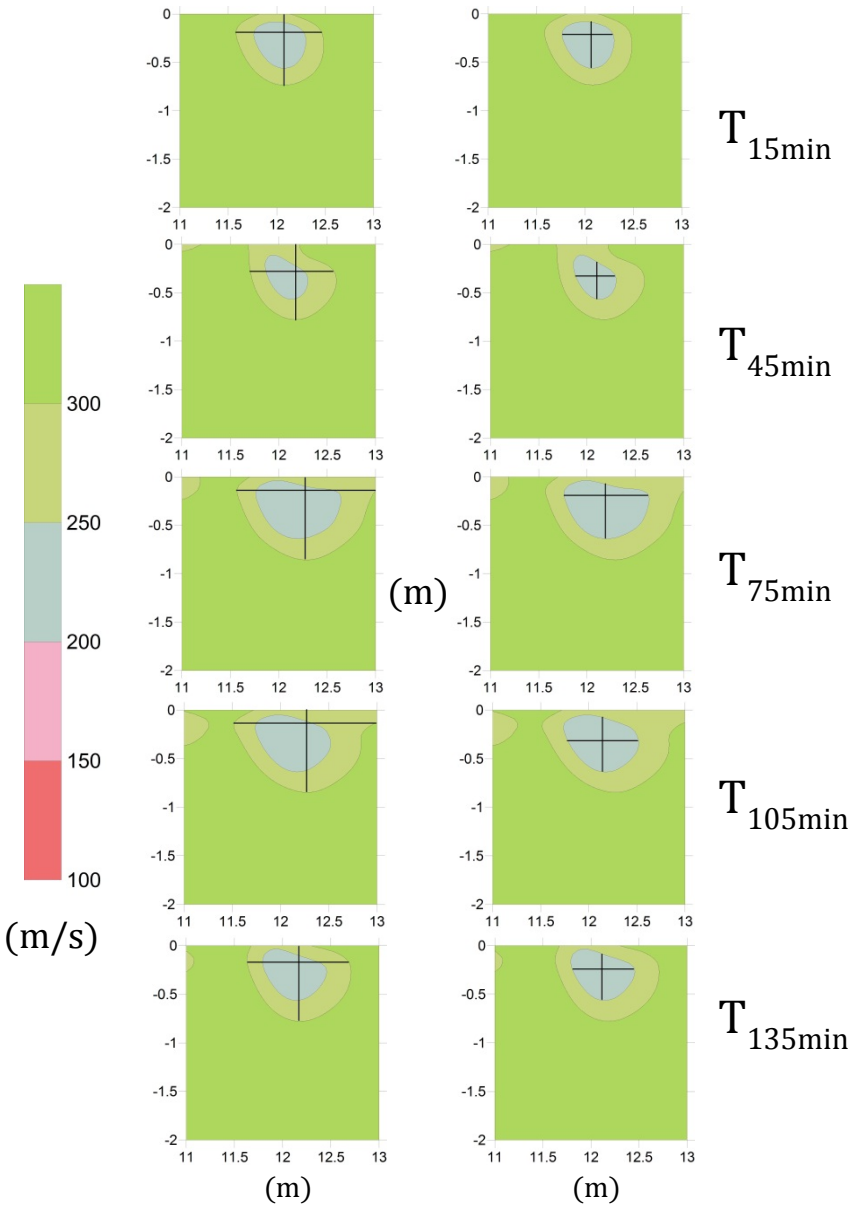

Figure 35: TLSFT profiles with a velocity range of 100 m/s to 300 m/s containing lines that represent the measured wetting front width and depth for the 250 m/s velocity contour (left panel) and 200 m/s velocity contour (right panel).

The saturated hydraulic conductivity for the undisturbed Sequatchie series (Leao, 2009) was used for the K_{fs} in the back-calculation of width and depth (see Equation 7 and Equation 8). The volume (V) and outflow (q) rates were measured in the field and recorded at each time-step (see Table 1). The back-calculated width (d) and depth (z) were calculated for each time-step (using Equation 9 and Equation 10) using the field parameters recorded (q and V) and the saturated hydraulic conductivity of the Sequatchie series (Table 2). The back-calculated width was consistently greater than the measured width from both the 250 m/s ($V_{250\ m/s}$) and 200 m/s ($V_{200\ m/s}$) velocity contours. The back- calculated depth was consistently less than $V_{250\ m/s}$ and $V_{200\ m/s}$ measurements.

The wetted width for the $V_{250\ m/s}$ and $V_{200\ m/s}$ were measured at the greatest lateral extent of the wetting front, and the wetted depth was measured from the surface to the greatest vertical extent of the wetting front (Figure 35). These values were measured at each of the five TLSFT time-steps for both the 250 m/s and 200 m/s velocity contours.

The saturation of the soil was not measured at the site prior to infiltration therefore, we investigate the relative change in saturation ($\Delta\theta$) in the infiltration region by calculating the spherical volume of the wetting fronts based on the width and depth dimensions for the back-calculated, $V_{250m/s}$, and $V_{200m/s}$ (see Table 2). We use the general equation for the volume of a sphere (i.e. $4/3\ \pi r^3$) where the width (width/2) and depth (depth/2) are used as the radius. The relative change in

saturation is then calculated by dividing the cumulative volume at each respective time-step by the calculated volume of the sphere (see Table 2). We use the porosity (ϕ) value of 0.385 based on Leao (2009), where calculated values of $\Delta\theta$ that are greater than 0.385 are denoted as $> \phi$.

The Schwartzman and Zur (1987) formulae were designed to predict wetted width and depth of a wetting front generated by an emitter at the surface that was constantly discharging water into an initially unsaturated soil at a constant rate. The width and depth dimensions using Schwartzman and Zur (1987) are desirable for applications in drip irrigation. Although, all parameters in our experiment did not satisfy the assumptions and constraints made by the experiment detailed in Schwartzman and Zur (1987), we were limited by the number of field parameters collected and will discuss the assumptions violated and their effect on our results in the discussion and conclusions section.

The field-saturated hydraulic conductivity was calculated using the wetting front geometry measured from the five TLSFT profiles at the 250 m/s and 200 m/s velocity contours, in addition to the outflow discharge rates measured in the field at each time-step. A combined equation is provided by Schwartzman and Zur (1987), in which Equation 9 and Equation 10 are reduced by eliminating the volume term, and using both wetted width and depth and its relation to outflow rate and hydraulic conductivity (Equation 11):

$$d = 1.32 z^{0.35} q^{0.33} {K_s}^{-0.33} \qquad \text{(Equation 11)}$$

The field-saturated hydraulic conductivity was calculated using the Schwartzman and Zur (1987) combined equation because it incorporates both wetting front width and depth, as opposed to only the wetting front width or depth.

4.5. Results

For the constant flux applicator TLSFT infiltration experiment, the combined field-saturated hydraulic conductivity was calculated (see Equation 11) using the measured wetted width (d), depth (z), and outflow rates (q), at the T_{15min}, T_{45min}, T_{75min}, T_{105min}, and T_{135min} TLSFT velocity profiles, respectively. This is done for each of the five TLSFT velocity profiles using the velocity contours of 250 m/s and 200 m/s as the boundaries for measured width and depth are used (see Table 2 and Figure 35).

In the Amoozemeter infiltration experiment, we calculated the field-saturated hydraulic conductivity using the field parameters collected during infiltration and the equations provided in the Amoozemeter manual (see Equation 7 and Equation 8). The K_{fs} estimations over the 32 hour period of data collection were averaged to be 4.9×10^{-6} m/s. As expected, the Amoozemeter TLSFT profiles show no observable velocity perturbations in the shape of an ellipsoidal wetting front or bulb (Figure 36). Therefore, K_{fs} estimates using the equations derived from Schwartzman and Zur (1987) could not be applied to the Ammozemeter TLSFT profiles.

The calculated combined K_{fs} from the TLSFT infiltration method at both the $V_{250m/s}$ and $V_{200m/s}$ velocity contours, K_{fs} from the Amoozemeter experiment, and the

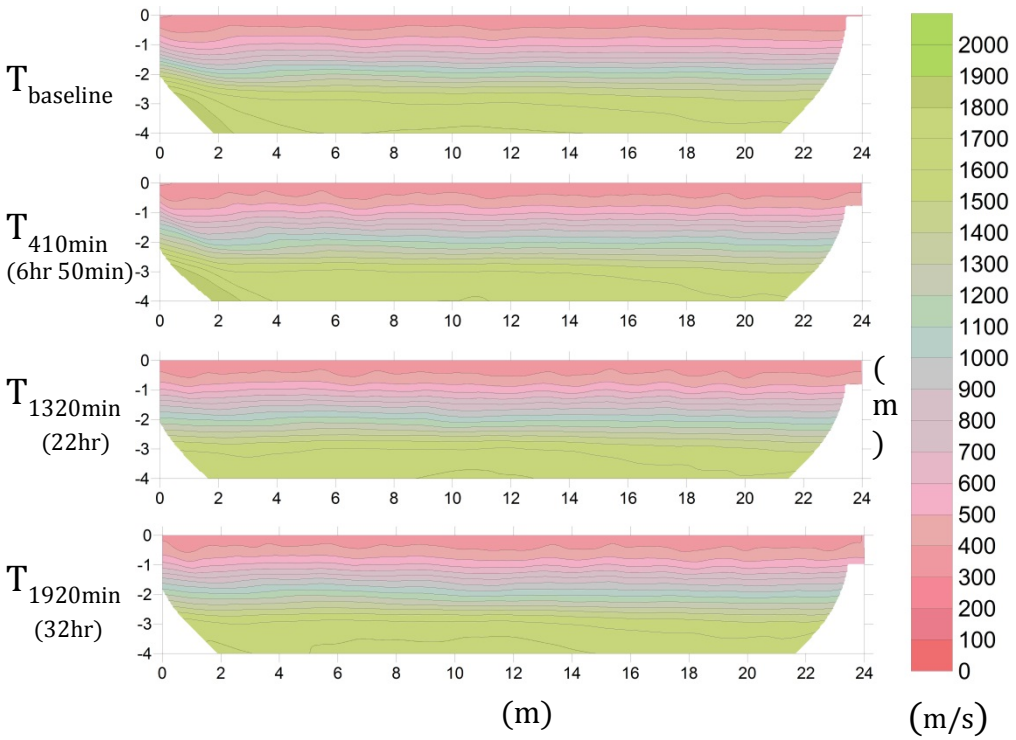

Figure 36: The three *P*-wave velocity tomograms of the Amoozemeter TLSFT infiltration experiment at the ETREC B-4 plot. The first panel is the baseline profile prior to infiltration and the following profiles are collecting after infiltration has begun. The unit is measured in *P*-wave velocity in meters per second with a contour interval of 100 m/s. There are no obvious velocity perturbations from to the infiltration experiment due to the small volume of water infiltrated.

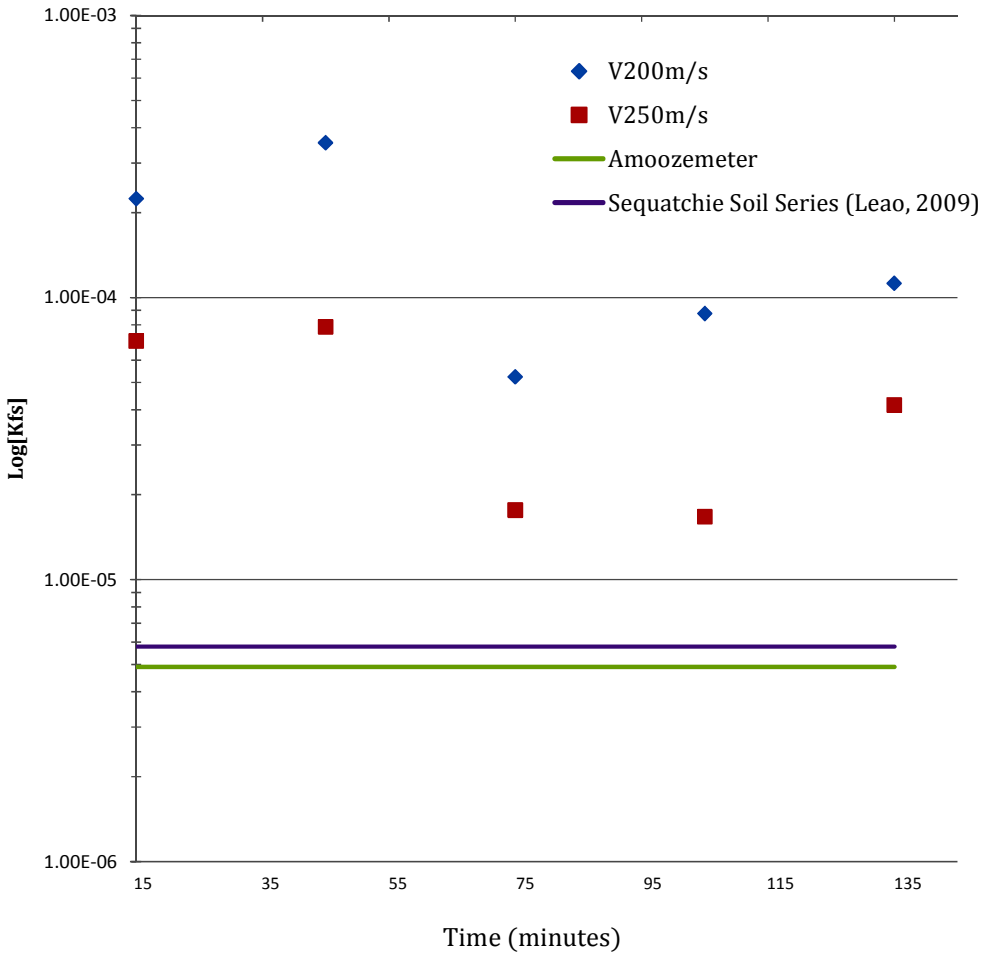

Figure 37: Log [Kfs] plotted versus time from the Sequatchie series, Amoozemeter method, and the TLSFT infiltration method where dimensions are measured from 250 m/s and 200 m/s velocity

K_s of the Sequatchie series all range between 4.9 x 10^{-6} m/s to 3.54 x 10^{-4} m/s (Figure 37).

4.6. Discussion and Conclusion

The proposed constant flux applicator TLSFT infiltration method was successful in imaging a migrating wetting front at five time-steps during an infiltration experiment, in addition to producing calculations of K_{fs} at the ETREC B-4 plot at each of the five time-steps for two different velocity contours ($V_{250m/s}$ and $V_{200m/s}$). The results from the constant flux applicator TLSFT infiltration experiment yielded K_{fs} calculations that are within one to two orders of magnitude of Amoozemeter K_{fs} calculated average and the Sequatchie soil series saturated hydraulic conductivity (Leao, 2009). The K_{fs} calculations from the $V_{250m/s}$ velocity contour are within one order of magnitude of the Amoozemeter and Sequatchie series K_{fs}, while the the K_{fs} of the $V_{200m/s}$ velocity contour falls within two orders of magnitude.

Again, we consider the measured parameter K_{sat} obtained using the Amoozemeter instrument to be synonymous with K_{fs} because the saturated hydraulic conductivity was measured via infiltration into an initially unsaturated soil (Reynolds et al., 1983). The Amoozemeter K_{fs} calculations are one to two orders of magnitude lower than the K_{fs} values calculated using the wetting front geometry from the constant flux applicator TLSFT infiltration experiment. These differences are attributed to a number of differences between the two infiltration experiments themselves, in addition to the discrepancies associated with the proposed

methodology for calculating K_{fs} using wetting front geometry. A major difference in the constant flux applicator infiltration experiment and the Amoozemeter experiment is the outflow rate into the augured hole. The constant flux applicator infiltrated an outflow rate of water with an average of 2.72×10^{-5} m^3/s, where the Amoozemeter infiltrated an outflow rate of water at 7×10^{-7} m^3/s. Additionally, the height of ponded water in the augured well during the constant flux applicator infiltration experiment was 0.5 m, where the height of the ponded head level in the Amoozemeter experiment was 0.15 m. The higher outflow rate from the constant flux applicator, in addition to the greater ponded head level from the constant flux applicator infiltration experiment both attribute to the higher K_{fs} calculations.

It was expected that the smaller wetting front geometry ($V_{200m/s}$) would produce smaller K_{fs} values using the Schwartzman and Zur (1987) combined formula, however, this is not what the results indicate. The $V_{200m/s}$ wetting front geometry produces K_{fs} estimates approximately one order of magnitude greater than those of the $V_{250m/s}$ velocity contour (see Table 2, Figure 37, and Figure 38). We conduct a sensitivity analysis to investigate the response of the empirical formulae presented by Schwartzman and Zur (1987) to changing wetting front width, depth, volume, and outflow discharge rates. For the calculation of K_{fs} using wetting front geometry, we use only the combined K_{fs} (Equation 11), however, Equation 9 and Equation 10 could be used to calculate K_{fs} where only the width or depth dimensions are used respectively. Therefore, we include the horizontal K_{fs} (Equation 9) and vertical Kfs (Equation 10) in the sensitivity analysis to determine

whether the combined (Equation 11) is the most robust of the three equations to calculate K_{fs} using wetting front geometry. The sensitivity analyses show the combined K_{fs} to have the most consistent relationship between variable width, depth, and outflow discharge rates to K_{fs}. The sensitivity analysis of the horizontal K_{fs} equations show the least consistent and most variable K_{fs} values with changing width, depth, and outflow discharge rates. The sensitivity to changing width, depth, and outflow discharge for the vertical K_{fs} equation falls between the horizontal and vertical K_{fs} equations. Tables and graphs detailing the sensitivity analysis are within the appendix section.

The calculations used to generate K_{fs} from the wetting front geometry and outflow rate from constant flux applicator cannot be used as absolute estimates of K_{fs} due to the violation of several assumptions and constrictions of the Schwartzman and Zur (1987) formulae used to empirically relate, wetted width and depth, emitter discharge, and wetted volume. The first violation our method makes is the assumption that the soil is initially unsaturated at the B-4 plot. The saturation values prior to infiltration were not obtained and realistically are not completely unsaturated. The crude estimates of relative saturation calculated using the spherical volume of the wetting front and volume of water infiltrated concur. Additionally, Schwartzman and Zur (1987) consider the wetted width, depth, and volume to be 100% saturated. The TLSFT infiltration profiles all contain low-velocity anomalies in the area of infiltration (wetting front), therefore they have not yet reached the threshold of >99% saturation based on relationship between *P*-

wave velocity and saturation described by the Gassman equation. Although the area of infiltration using the constant flux applicator is most likely very saturated, air-filled pores in the soil are present based on the changes in *P*-wave velocities observed.

In conclusion, the TLSFT infiltration method using a constant flux applicator is very useful in producing an isolated image of a migrating wetting front through the vadose zone. The visual characterization of the geometry and distribution of the fluid from the migrating wetting front is valuable to a variety of disciplines that attempt to investigate fluid movement in the subsurface. The ability to image migrating water can be considered more useful compared to a quantitative value that may not be representative of field site as a whole, due to the inability to observe the fluid migration from the surface measurements obtained.

The quantitative calculations of K_{fs} using the TLSFT infiltration method with a constant flux applicator were investigated for comparison to standard methods that explore fluid migration in the vadose zone (i.e. Amoozemeter). Although the K_{fs} calculations using the TLSFT method were within one to two orders of magnitude of the Amoozemeter calculations and K_s of the Sequatchie series, the method needs refining to reduce the amount of assumptions violated (i.e. initial saturation values, wetted volume saturation values, etc).

5. CONCLUSIONS AND RECOMMENDATIONS

Time-lapse seismic first-arrival tomography (TLSFT) is a successful method for monitoring two different infiltration events using a constant flux applicator. Ellipsoidal low-velocity perturbations are generated by the relative changes in saturation as water is infiltrated from the surface. The TLSFT infiltration method provides a visual characterization of fluid migration through the subsurface both temporally and spatially. This allows one to image the wetting front geometry and distribution of infiltrated water volume as it advances through the vadose zone. The advantage in imaging the migrating wetting is the potential for locating anisotropy and/or heterogeneities that may be influencing localized fluid flow.

The hydraulic conductivity values using the TLSFT infiltration method with the constant flux applicator compared with the K_{fs} values of the Amoozemeter experiment and K_s of the Sequatchie soil series (Leao, 2009) have differences that are on the order of one to two magnitudes depending on the velocity contour used in defining the wetting front boundary. The differences between the K_{fs} values for the TLSFT infiltration method and the Amoozemeter are in part attributed to a number of differences between the infiltration experiments themselves. A major difference in the constant flux applicator infiltration experiment and the Amoozemeter experiment is the outflow rate into the augured well, which was 2.72 x 10^{-5} m^3/s using the constant flux applicator, and $7x10^{-7}$ m^3/s for the Amoozemeter experiment. Furthermore, the height of ponded water in the augured well during the constant flux applicator infiltration experiment (0.50 m) was 0.35 m greater than that of the Amoozemeter ponded height (0.15 m). The greater outflow rate

from the constant flux applicator, in addition to the greater ponded head level from the constant flux applicator infiltration experiment both attribute to the higher K_{fs} calculations using the TLSFT infiltration experiment.

It should also be noted that the infiltration for the second constant flux applicator experiment (2012) ended at 64 minutes, therefore the outflow discharge values used for the purpose of calculating K_{fs} at the three time-steps after infiltration ceased were averaged and used for calculating K_{fs}, at those particular time-steps.

In addition to differences in the infiltration experiment, the TLSFT infiltration method to calculate K_{fs} with the combined formula from Schwartzman and Zur (1987) violates many assumptions and controls that were used by Schwartzman and Zur (1987) in their experimentation. This ultimately affects the calculated K_{fs} values. These violations include an initially unsaturated porous media and a fully saturated wetting front. The saturation values prior to infiltration were not obtained and realistically are not completely unsaturated. Additionally, Schwartzman and Zur (1987) consider the wetted width, depth, and volume to be 100% saturated. The TLSFT infiltration profiles all contain low-velocity anomalies in the area of infiltration (wetting front), therefore they have not yet reached the threshold of >99% saturation based on relationship between *P*-wave velocity and saturation described by the Gassman equation. Although the area of infiltration using the constant flux applicator is most likely very saturated, air-filled pores in the soil are present based on the *P*-wave velocities observed.

The TLSFT velocity profiles for the second constant flux applicator experiment did not require a trend-analysis to isolate the migrating wetting front. An analysis of TLSFT data collection and the need for a trend-analysis in the time-lapse velocity tomograms after infiltration begins should be investigated. The need for a trend-analysis may be closely related to the quality of seismic data collected (i.e. signal-to-noise ratio).

The second constant flux applicator TLSFT infiltration experiment contained some noise in the seismic data collected. This is attributed to a phenomenon we refer to as "ringing", which occurs when the hammer strikes the plate at an oblique angle, creating a ringing sound that interferes with producing a clean seismic transmission. In the first infiltration experiment, we had field assistants that have been involved with a number of seismic surveys where their experience resulted in generating a clean contact between the sledge hammer and metal plate, which produced in cleaner seismic records (Figure 38). Due to the lack of available experienced field assistants in the summer months, the person generating the seismic source at each shot point was not as experienced in generating a clean contact. As a result, several shot points contained the "ringing" phenomena in the seismographs (Figure 39).

The presence of the noise results in less accurate first arrival picks. Although, the velocity profiles in the second constant flux applicator TLSFT infiltration experiment is able to resolve the ellipsoidal low-velocity anomaly, when the trend analysis is applied, the small velocity variations due to the noise in the

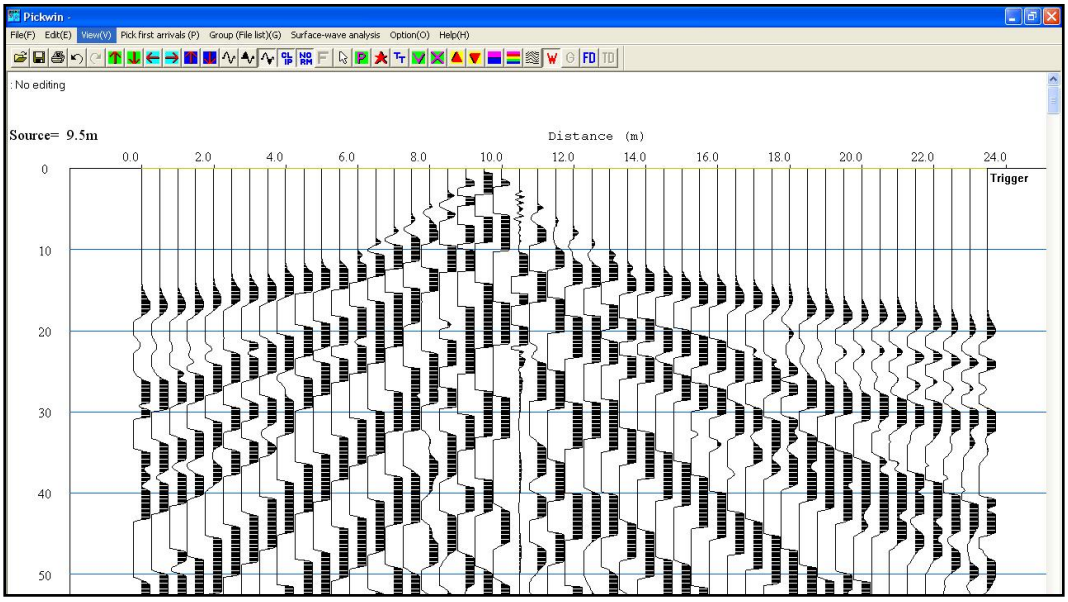

Figure 38: Example of a seismic record from a clean contact between the hammer and metal plate.

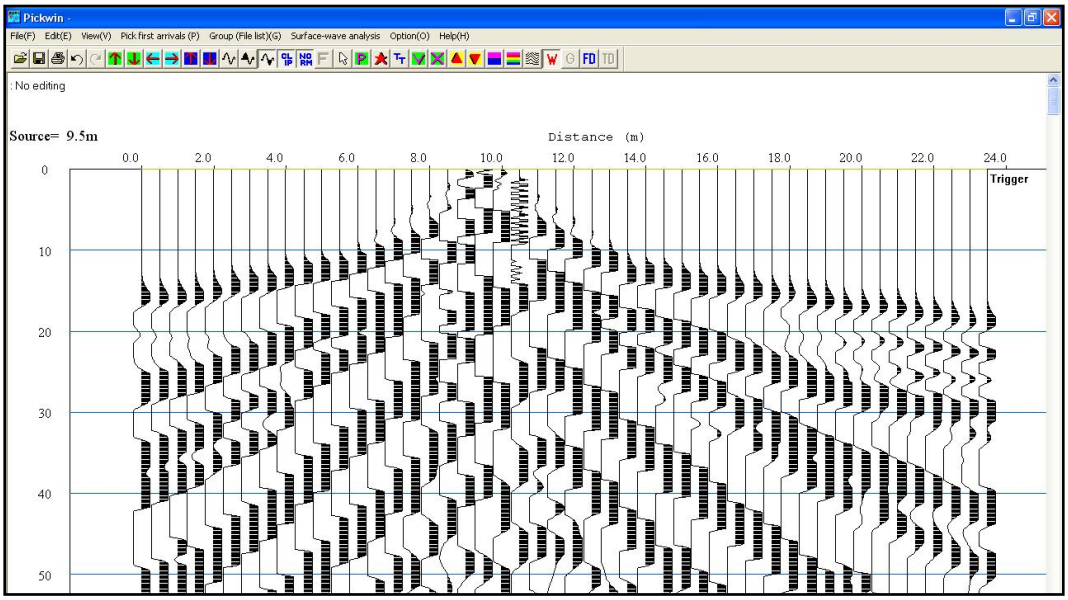

Figure 39: Example of a noisy seismic record resulting from "ringing", as the oblique contact between the sledge hammer and metal plate introduces noise into the seismic record.

first-arrival picks generated areas of anomalous velocity perturbations. We chose to use the velocity tomograms in the second constant flux applicator TLSFT infiltration experiment without the trend analysis, but with a comparable range of velocities to isolate the anomaly due to the infiltration event. The velocity scale for the second constant flux applicator TLSFT infiltration experiment is the positive range of velocities (100 m/s to 300 m/s) used in the first TLSFT infiltration experiment (-300 m/s to -100 m/s) with the trend analysis applied.

Furthermore, the sensitivity analyses show the empirical formulae presented by Schwartzman and Zur (1987) to be highly variable when using wetting front width, depth, and outflow discharge rates outside a relatively small range in values (e.g. wetting front width between 2 m and 3.5 m), where K_{fs} values increase or decrease rapidly outside these ranges. Tables and graphs detailing the sensitivity analysis are within the appendix section.

For the future, the infiltration experiments should be conducted simultaneously with other geophysical techniques to determine whether TLSFT is the most robust geophysical tool for imaging a migrating wetting front. Additional geophysical methods like ground penetrating radar (GPR) and electrical resistivity tomography (ERT) have been used to investigate hydrologic investigations and should be considered in the future for imaging a migrating wetting front. The acquisition of TLSFT, GPR, and ERT collectively during a single infiltration experiment would be ideal to compare the methods ability while all under the same field and infiltration conditions.

Future investigations using the TLSFT infiltration method to image a migrating wetting front and further calculate hydraulic conductivity should first determine saturation content in the field prior to infiltration. Having saturation values prior to infiltration will provide more options to calculate hydraulic conductivity that are more accurate than the empirical formulae used in chapter 4. The multitude of assumptions violated by the application of TLSFT infiltration wetting front geometry for calculating K_{fs} restrict the credibility of the values calculated using formulae provided by Schwartzman and Zur (1987).

In the future, testing the TLSFT infiltration method at a variety of sites to investigate the range of soil textures in which this method can be applied to is necessary to determine the extent or limitation of its application. Additionally, conducting a TLSFT infiltration event at a site where tensiometer(s) are installed within the soil profile can provide information regarding the relationship between relative soil moisture content (or tension) and seismic *P*-wave velocity as well as the initial saturation values. This would aid in the development of a numerical model for calculating hydraulic conductivity using the TLSFT method, for both the horizontal and vertical directions. Having the hydraulic conductivity in the vertical and horizontal directions would provide a quantitative evaluation of anisotropy, to support the visual characterization of anisotropy. Furthermore, if the TLSFT data is acquired over a long profile (e.g. 96 geophones and a 48 m profile length), several constant flux applicators could be positioned along the profile and the spatial data collected in the area would be increased significantly. Varying the geometry of the

seismic profile could also provide additional information about subsurface anisotropy or soil structure, such as collecting two seismic profiles orientated in a cross (i.e. two perpendicular lines intersecting each other at their centers) which would add another dimension to geometry and water distribution of the wetting front migration.

The time-steps used in each of the TLSFT infiltration experiments (approximately 30 minutes) were in part a product of the acquisition time of surface seismic data. The seismic data required approximately 10-15 minutes to collect the 12 to 13 shot points along the 24 m profile. Due to the relationship between infiltration rate (I) and time (Equation 12):

$$I = \frac{1}{\sqrt{time}} \qquad \text{(Equation 12)}$$

we are unable to capture the greatest variability in infiltration rates, which occur at the beginning of the experiment. Acquiring the TLSFT data at earlier times in the infiltration experiment may provide a greater understanding of vadose zone fluid flow within this interval of time where fluid flow is rapidly changing.

In conclusion, the TLSFT infiltration method using a constant flux applicator is a robust, relatively non-invasive, *in-situ* technique to visually characterize the geometry and water distribution of a migrating wetting front in the vadose zone by providing images of the subsurface at varying times throughout an infiltration experiment. The ability to image the wetting front using positional variations of seismic *P*-wave velocity in the area of infiltration can expose anisotropic features or soil structures that may be dominating fluid flow. The hydraulic conductivity

calculations using the TLSFT infiltration method and equations provided by Schwartzman and Zur (1987) provide an additional quantitative characterization of the vadose zone fluid properties, however this method needs refining in several aspects to be applicable across a variety of sites while still providing an accurate range of values.

REFERENCES

Aki, K., Christoffersson, A., and E. S. Huesbye, 1977, Determination of 3-Dimensional Seismic Structure of Lithosphere: Journal of Geophysical Research, v. 82, p. 277-296.

Amoozegar, A., and A. W. Warrick, 1986, Hydraulic conductivity of saturated soils: field methods, p. 758-763. In: A. Klute (ed.) Methods of soil analysis. Part I. Argon. Monogr. 9. ASA and SSSA, Madison, WI.

Amoozegar, A., 1989, A Compact Constant-head Permeameter for Measuring Saturated Hydraulic Conductivity of the Vadose Zone: Soil Science Society of America Journal, v. 53, p. 1356-1361.

Ankeny, M. D., Kaspar, T. C., and R. Horton, 1988, Design for an Automated Tension Infiltrometer: Soil Science Society of America Journal, v. 52, p. 893-896.

Ankeny, M. D., Ahmed, M., Kaspar, T. C., and R. Horton, 1991, Simple Field Method for Determining Unsaturated Hydraulic Conductivity: Soil Science Society of America Journal, v. 55, p. 467-470.

Bachrach, R., and A. Nur, 1998, High-resolution shallow-seismic experiments in sand, Part I: Water table, fluid flow, and saturation: Geophysics, v. 63, p. 1225-1233.

Basile, A., Coppola, A., De Mascellis, R., and L. Randazzo, 2006, Scaling Approach to Deduce Field Unsaturated Hydraulic Properties and Behavior from Laboratory Measurements on Small Cores: Vadose Zone Journal, v. 5, p. 1005-1016.

Biot, M. A., 1956, Theory of Propagation of Elastic Waves in a Fluid-Saturated Porous Solid: Journal of the Acoustical Society of America, v. 28, p. 168-178.

Bouwer, H., 1966, Rapid field measurement of air entry value and hydraulic conductivity as significant parameters in flow system analysis: Water Resources Research, v. 1, p. 729-738.

Bouwer, H., 1986, Intake rate: cylinder infiltrometer, p. 825-844. In: A. Klute (ed.) Methods of Soil Analysis. Part I. 2nd ed. Argon. Monogr. 9. ASA and SSSA, Madison, WI.

Bouwer, H., 1978, Groundwater Hydrology. McGraw-Hill, Toronto.

Bresler, E., 1978, Analysis of Trickle Irrigation with Application to Design Problems: Irrigation Science, v. 1, p. 3-13.

Cattermole, M., 1958, Geologic map of the Knoxville Quadrangle: The Geological Survey, Map GQ-115, scale 1:24, 000.

Corey, A. T., 1977, Mechanics of Heterogeneous Fluids in Porous Media: Water Resources Publications, Fort Collins, CO.

Dane, J. H., and C. Topp, 2002, Methods of Soil Analysis: Soil Science Society of America Book Series, v. 1-5.

Darcy, H., 1856, "Les Fontaines Publique de la Ville de Dijon." Dalmont, Paris.

Domenico, S. N., 1974, Effect of Water Saturation on Seismic Reflectivity of Sand Reservoirs Encased in Shale: Geophysics, v. 39, p. 759-769.

Elder, J. A., SCS, and M. E. Springer, 1963, Soil Map Plant Science Farm University of Tennessee, Knoxville, Tennessee: U. S. Department of Agriculture Soil Conservation Service Cooperating with University of Tennessee.

Elrick, D. E., and W. D. Reynolds, 1992, Methods for Analyzing Constant-Head Well Permeameter Data: Soil Science Society of America Journal, v. 56, p. 320-323.

Foti, S., and R. Lancelotta, 2004, Soil Porosity from Seismic Velocities: Geotechnique, v. 54, p. 551-554.

Gaines, D. P., 2011, *Advances in First-arrival Tomography.* (Doctoral Dissertation): Retrieved from Author. University of Tennessee at Knoxville.

Garambois, Senechal, S. P., and H. Perroud, 2002, On the use of combined geophysical methods to assess water content and water conductivity of near-surface formations: Journal of Hydrology, v. 259, p. 32-48.

Gardner, W. R., 1960, Dynamic aspects of water availability to plants: Soil Science, v. 89, p. 63-73.

Gassmann, F., 1951, Uber die elastizitat poroser median: Vier. Der natur Gesellschaft, v. 96, p. 1-23.

Gebrande, H., and H. Miller, 1985, Refraction seismology, in F. Bender ed., Applied geosciences II: Ferdinand Enke Publishing House, p. 226-260.

George, L. A., Dewoolkar, M.M., and D. Znidarcic, 2009, Simultaneous Laboratory Measurement of Acoustic and Hydraulic Properties of Unsaturated Soils: Vadose Zone Journal, v. 8, p. 633-642.

Green, W. H., and G. A. Ampt, 1911, Studies on soil physics. I. The flow of air and water through soils: Journal of Agricultural Science, v. 4, p. 1-24.

Haeni, F. P., 1986., Application of seismic-refraction techniques to hydrologic studies, United States Geological Survey.

Hillel, D., Krentos, V. D., and Y. Stylianou, 1972, Procedure and test of an internal drainage method for measuring soil hydraulic characteristics *in situ*: Soil Science, v. 114, p. 395-400.

Hillel, D., 1980a, "Fundamentals of Soil Physics." Academic Press, Toronto.

Hillel, D., 1980b, "Applications of Soil Physics." Academic Press, Toronto.

Hillel, D., 1998, "Environmental Soil Physics." Academic Press, Toronto.

Hubert, M. K., 1956, Darcy's law and the field equations of the flow of underground fluids: Transactions of the American Institute of Mining, Metallurgical and Petroleum Engineers, v. 207, p. 222-239.

Humphreys, E., and R. W. Clayton, 1988, Adaption of Back Projection Tomography to Seismic Travel Time Problems: Journal of Geophysical Research-Solid Earth and Planets, v.93, p. 1073-1085.

Jones, I. F., 2010, Tutorial: Velocity estimation via ray-based tomography: First Break, v. 28, p. 45-52.

Lay, T., and T. C. Wallace, 1955, "Modern global seismology." San Diego, Academic Press, xii, 521 p.

Leao, T.P., 2009, *Effects of Water Content and Salinity on Soil Electrical Properties at 50 MHz: Structural and Textural Interactions,* (Doctoral Dissertation): University of Tennessee at Knoxville.

Lecomte, I., Gjoystdal, H., Dahle, A., and O. C. Pedersen, 2000, Improving modeling and inversion in refraction seismics with a first-order Eikonal solver: Geophysical Prospecting, v. 48, p. 437-454.

Lumley, D. E., 2001, Time-lapse seismic reservoir monitoring: Geophysics, v. 66, p. 50-53.

Mavko, G., Chan, C., and T. Mukerji, 1995, Fluid Substitution- Estimating Changes in V-P without Knowing V-S: Geophysics, v. 60, p. 1750-1755.

McWhorter, D. B., Corey, A. T., and K. M. Adam, 1973, The elimination of trapped gas from porous media by diffusion: Soil Science, v. 116, p. 18-25.

Moncef, H., Hedi, D., Jelloul, B., and M. Mohamed, 2002, Approach for predicting the wetting front depth beneath a surface point source: Theory and numerical aspect, v. 51, no. 4, p. 347-360.

Mualem, Y., 1976, A new model for predicting the hydraulic conductivity of unsaturated porous media: Water Resources Research, v. 12, p. 513-522.

Murphy, W. F., 1982, *Effects of Microstructure and Pore Fluids on the Acoustic Properties of Granular Sedimentary Materials*: (Doctoral Dissertation). Stanford University.

Mubarak, I., Mailhol, J. C., Angulo-Jaramillo, R., Bouarfa, S., and P. Ruelle., 2009, Effect of temporal variability in soil hydraulic properties on simulated water transfer under high-frequency drip irrigation: Agriculture Water Management, v. 96, p. 1547-1559.

Neuman, S. P., 1975, Galerkin approach to saturated-unsaturated flow in porous media. In: Gallagher, R.H., Oden, J. T., Taylor, C., and Zienkiewicz, O. C., eds., "Finite Elements in Fluids, Vol. 1: Viscous Flow and Hydrodynamics." John Wiley, London.

Philip, J. R., 1955, Desperately seeking Darcy in Dijon: Soil Science Society of American Journal, v. 59, p. 319-324.

Pinder, F. G., and W. G. Gray, 1977, "Finite Element Simulation in Surface and Subsurface Hydrology." Academic Press, New York.

Reynolds, W. D., Elrick, D. E. and Topp, G. C., 1983, A Reexamination of the Constant Head Well Permeameter Method for Measuring Saturated Hydraulic Conductivity Above the Water Table: Soil Science, v. 136, p. 250.

Reynolds, W. D., Elrick, D. E., and Clothier, B. E., 1985, The constant head well permeameter: Effect of Unsaturated Flow: Soil Science, v. 139, p. 172.

Reynolds, W. D. and D. E. Elrick, 1985, *In-situ* measurement of field-saturated hydraulic conductivity, sorptivity and the α-parameter using the Guelph permeameter: Soil Science, v. 136, p. 172-180.

Reynolds, W. D. and D. E. Elrick, 1986, A method for simultaneous in situ measurement in the vadose zone of field-saturated hydraulic conductivity, sorptivity and the conductivity-pressure head relationship: Ground Water Monitoring and Remediation, v. 6, p. 84-95.

Reynolds, W. D. and D. E. Elrick, 1990, Ponded infiltration from a single-ring: 1 Analysis of steady flow: Soil Science Society of America Journal, v. 54, p. 1233-1241.

Richards, L. A., 1931, Capillary conduction of liquids in porous mediums: Physics, v. 1, p. 318-333.

Roberts, W., 1955, Soil Survey of Knox County, Tennessee: United States Department of Agriculture in cooperation with the Tennessee Agricultural Experimental Station and the Tennessee Valley Authority. Series 1942, no. 10.

Schuster, G. T., and A. Quintus-Bosz, 1993, Wavepath Eikonal Traveltime Inversion: Theory Geophysics, v. 58, p. 1314-1323.

Schwartzman M., and B. Zur, 1987, Emitter Spacing and Geometry of Wetted Soil Volume: Journal of Irrigation and Drainage Engineering, v. 112, no. 3, p. 242-253.

Sepaskhah, A. R. and H. Chitsaz, 2004, Validating the Green-Ampt Analysis of Wetted Radius and Depth in Trickle Irrigation: Biosystems Engineering, v. 89, no. 2, p. 231-236.

Sheehan, J., Doll, W. E., Watson, D., and W. Mandell, 2005a, Applications of seismic refraction tomography to karst cavities: U.S. Geological Survey Karst Interest group Proceedings, p. 29-38.

Sheehan, J.R., Doll, W. E., and W.E. Madell, 2005b, An evaluation of methods and available software for seismic refraction tomography analysis: Journal of Environmental and Engineering Geophysics, v. 10, p. 21-24.

Slichter, C. S., 1899, U.S.G.S. Annual Report: I9-22, p. 295-384.

Soil Survey Staff, Natural Resources Conservation Service, United States Department of Agriculture, 2008, Office of Soil Series Descriptions [online WWW]. Available URL: "https://soilseries.sc.egov.usda.gov/OSD_Docs/S/SEQUATCHIE.html" USDA-NRCS, Lincoln, NE. Accessed: 07-13-2012.

Solomon, D. K., Moore, G. K., Toran, L. E., Dreir, R. B., and W. M. McMaster, 1992, Status report. A hydrologic framework for the Oak Ridge Reservation: Environmental Science Division Publication, no. 3815, ORNL/TM-12026.

Spetzler, J., and R. Snieder, 2004, Tutorial: The Fresnel volume and transmitted waves: Geophysics, v. 69, p. 653-663.

Steeples, D. W., and R. D. Miller, 1998, Avoiding pitfalls in shallow seismic reflection surveys: Geophysics, v. 63, p. 1213-1224

Stephens, D. B., 1995, "Vadose Zone Hydrology." CRC Press. Boca Raton.

van Genuchten, M. Th., 1980, A closed form equation for predicting the hydraulic conductivity of unsaturated soils: Soil Science Society of America Journal, v. 44, p. 892-898.

Warrick, A. W., and D. R. Nielsen, 1980, Spatial variability of soil physical properties in the field. In: Hillel, D., ed., "Applications of Soil Physics." Academic Press, New York.

Woodward, M., and F. Rocca, 1989, *Wave equation tomography*: (Ph.D. Dissertation). Stanford University.

Youngs, E. G., 1987, Estimating hydraulic conductivity values from ring infiltrometer measurements: Journal of Soil Science, v. 38, p. 623-632.

Youngs, E. G., 1991a, Infiltration measurements- A review: Hydrology Proceedings, v. 5, p. 309-319.

Youngs, E. G., Leeds-Harrison, P. B., and D. E. Elrick, 1995, The hydraulic conductivity of low permeability soils used as landfill lining and capping material: analysis of pressure infiltrometer measurements: Journal of Soil Technology, v. 8, p. 153-160.

Zhang, J., and M. N. Toksoz, 1998, Nonlinear Refraction Traveltime Tomography: Geophysics, v. 63, p. 1726-1737.

Zimmer, M. A., Prasad, M., Mavko, G., and A. Nur, 2007, Seismic velocities of unconsolidated sands: Part 1 --- Pressure trends from 0.1 to 20 MPa: Geophysics, v. 72, p. E1-E13.

APPENDIX

SENSITIVITY ANALYSIS OF K_{FS} WITH CHANGING WIDTH (d)					
d (m)	z (m)	q (m^3/s)	V (m^3)	K_{fs} hoirzontal (m/s)	K_{fs} combined (m/s)
0.1	0.5	2.73E-05	0.106	3.86E+01	3.26E-02
0.2	0.5	2.73E-05	0.106	6.55E-01	3.98E-03
0.3	0.5	2.73E-05	0.106	6.03E-02	1.17E-03
0.4	0.5	2.73E-05	0.106	1.11E-02	4.88E-04
0.5	0.5	2.73E-05	0.106	2.99E-03	2.48E-04
0.6	0.5	2.73E-05	0.106	1.02E-03	1.43E-04
0.7	0.5	2.73E-05	0.106	4.13E-04	8.95E-05
0.8	0.5	2.73E-05	0.106	1.88E-04	5.97E-05
0.9	0.5	2.73E-05	0.106	9.41E-05	4.18E-05
1	0.5	2.73E-05	0.106	5.07E-05	3.04E-05
1.1	0.5	2.73E-05	0.106	2.89E-05	2.27E-05
1.2	0.5	2.73E-05	0.106	1.73E-05	1.75E-05
1.3	0.5	2.73E-05	0.106	1.08E-05	1.37E-05
1.4	0.5	2.73E-05	0.106	7.00E-06	1.10E-05
1.5	0.5	2.73E-05	0.106	4.66E-06	8.88E-06
1.6	0.5	2.73E-05	0.106	3.19E-06	7.31E-06
1.7	0.5	2.73E-05	0.106	2.23E-06	6.08E-06
1.8	0.5	2.73E-05	0.106	1.60E-06	5.11E-06
1.9	0.5	2.73E-05	0.106	1.16E-06	4.34E-06
2	0.5	2.73E-05	0.106	8.59E-07	3.72E-06
2.1	0.5	2.73E-05	0.106	6.44E-07	3.21E-06
2.2	0.5	2.73E-05	0.106	4.90E-07	2.78E-06
2.3	0.5	2.73E-05	0.106	3.77E-07	2.43E-06
2.4	0.5	2.73E-05	0.106	2.94E-07	2.14E-06
2.5	0.5	2.73E-05	0.106	2.31E-07	1.89E-06
2.6	0.5	2.73E-05	0.106	1.83E-07	1.68E-06
2.7	0.5	2.73E-05	0.106	1.47E-07	1.50E-06
2.8	0.5	2.73E-05	0.106	1.19E-07	1.34E-06
2.9	0.5	2.73E-05	0.106	9.65E-08	1.21E-06
3	0.5	2.73E-05	0.106	7.91E-08	1.09E-06
3.1	0.5	2.73E-05	0.106	6.52E-08	9.85E-07
3.2	0.5	2.73E-05	0.106	5.41E-08	8.94E-07
3.3	0.5	2.73E-05	0.106	4.51E-08	8.15E-07
3.4	0.5	2.73E-05	0.106	3.79E-08	7.44E-07
3.5	0.5	2.73E-05	0.106	3.19E-08	6.82E-07

Table A1: Sensitivity analysis table of K_{fs} with changing wetting front width (d) of the Schwartzman and Zur (1987) horizontal and combined equations.

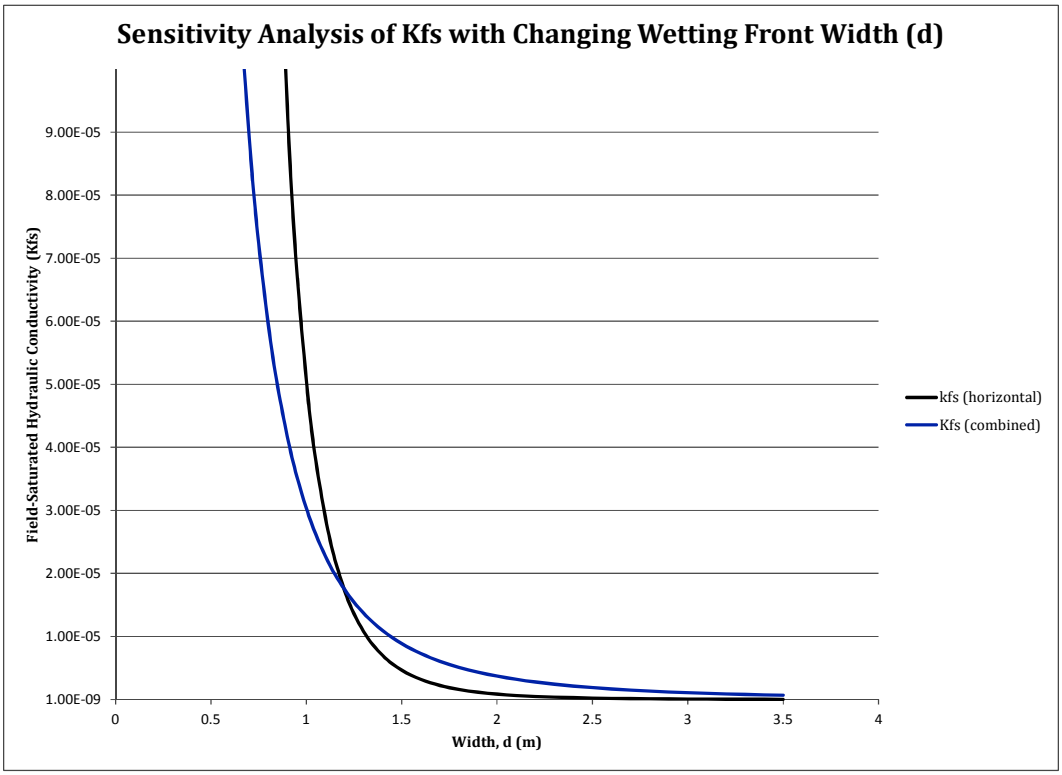

Figure A1: Sensitivity analysis graph of K_{fs} with changing wetting front width (d) for the Schwartzman and Zur (1987) horizontal and combined equations. The range in changing width values and constant values of depth, volume, and outflow discharge rates are detailed in Table A1.

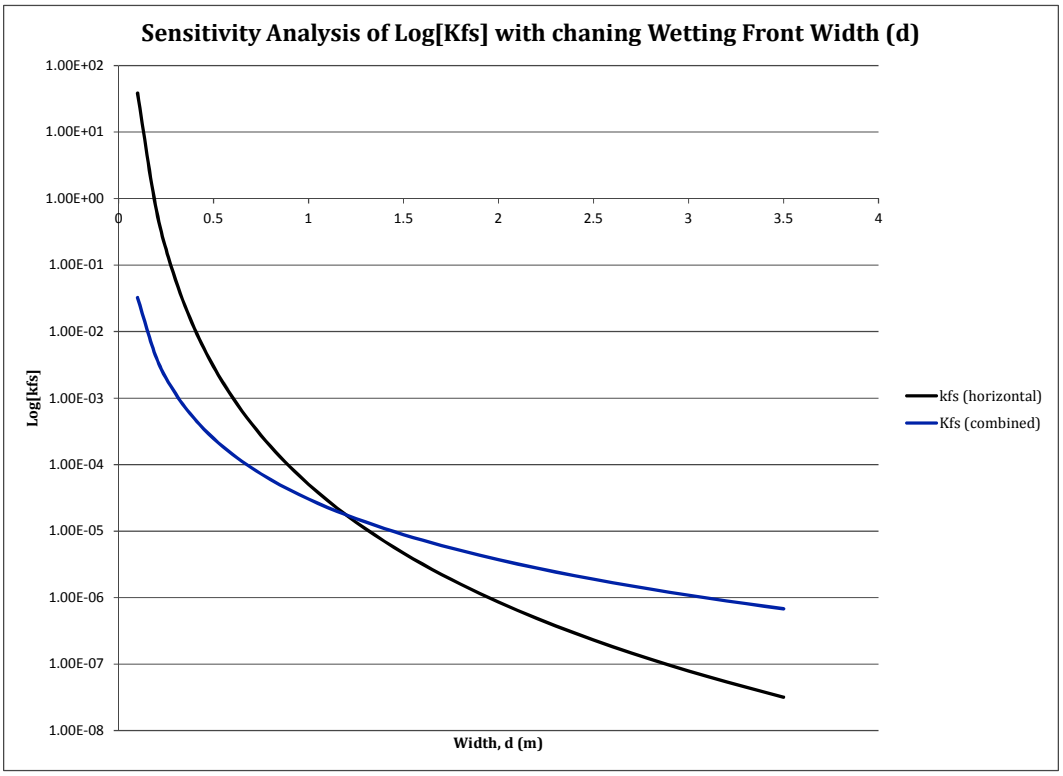

Figure A2: Sensitivity analysis graph of Log [K_{fs}] with changing wetting front width (d) for Schwartzman and Zur (1987) horizontal and combined equations. The range in changing width values and constant values of depth, volume, and outflow discharge rates are detailed in Table A1.

SENSITIVITY ANALYSIS OF K_{FS} WITH CHANGING DEPTH (z)					
d (m)	z (m)	q (m^3/s)	V (m^3)	K_{fs} vertical (m/s)	K_{fs} combined (m/s)
0.5	0.1	2.73E-05	0.106	4.77E-07	4.50E-05
0.5	0.2	2.73E-05	0.106	2.23E-06	9.38E-05
0.5	0.3	2.73E-05	0.106	5.48E-06	1.44E-04
0.5	0.4	2.73E-05	0.106	1.04E-05	1.96E-04
0.5	0.5	2.73E-05	0.106	1.71E-05	2.48E-04
0.5	0.6	2.73E-05	0.106	2.56E-05	3.01E-04
0.5	0.7	2.73E-05	0.106	3.60E-05	3.54E-04
0.5	0.8	2.73E-05	0.106	4.85E-05	4.08E-04
0.5	0.9	2.73E-05	0.106	6.30E-05	4.63E-04
0.5	1	2.73E-05	0.106	7.96E-05	5.17E-04
0.5	1.1	2.73E-05	0.106	9.84E-05	5.72E-04
0.5	1.2	2.73E-05	0.106	1.19E-04	6.28E-04
0.5	1.3	2.73E-05	0.106	1.43E-04	6.83E-04
0.5	1.4	2.73E-05	0.106	1.68E-04	7.39E-04
0.5	1.5	2.73E-05	0.106	1.96E-04	7.95E-04
0.5	1.6	2.73E-05	0.106	2.26E-04	8.52E-04
0.5	1.7	2.73E-05	0.106	2.59E-04	9.08E-04
0.5	1.8	2.73E-05	0.106	2.94E-04	9.65E-04
0.5	1.9	2.73E-05	0.106	3.32E-04	1.02E-03
0.5	2	2.73E-05	0.106	3.72E-04	1.08E-03
0.5	2.1	2.73E-05	0.106	4.14E-04	1.14E-03
0.5	2.2	2.73E-05	0.106	4.59E-04	1.19E-03
0.5	2.3	2.73E-05	0.106	5.07E-04	1.25E-03
0.5	2.4	2.73E-05	0.106	5.57E-04	1.31E-03
0.5	2.5	2.73E-05	0.106	6.10E-04	1.37E-03
0.5	2.6	2.73E-05	0.106	6.66E-04	1.43E-03
0.5	2.7	2.73E-05	0.106	7.24E-04	1.48E-03
0.5	2.8	2.73E-05	0.106	7.85E-04	1.54E-03
0.5	2.9	2.73E-05	0.106	8.49E-04	1.60E-03
0.5	3	2.73E-05	0.106	9.15E-04	1.66E-03
0.5	3.1	2.73E-05	0.106	9.84E-04	1.72E-03
0.5	3.2	2.73E-05	0.106	1.06E-03	1.78E-03
0.5	3.3	2.73E-05	0.106	1.13E-03	1.84E-03
0.5	3.4	2.73E-05	0.106	1.21E-03	1.89E-03
0.5	3.5	2.73E-05	0.106	1.29E-03	1.95E-03

Table A2: Sensitivity analysis table of K_{fs} with changing wetting front depth (z) of the Schwartzman and Zur (1987) vertical and combined equations.

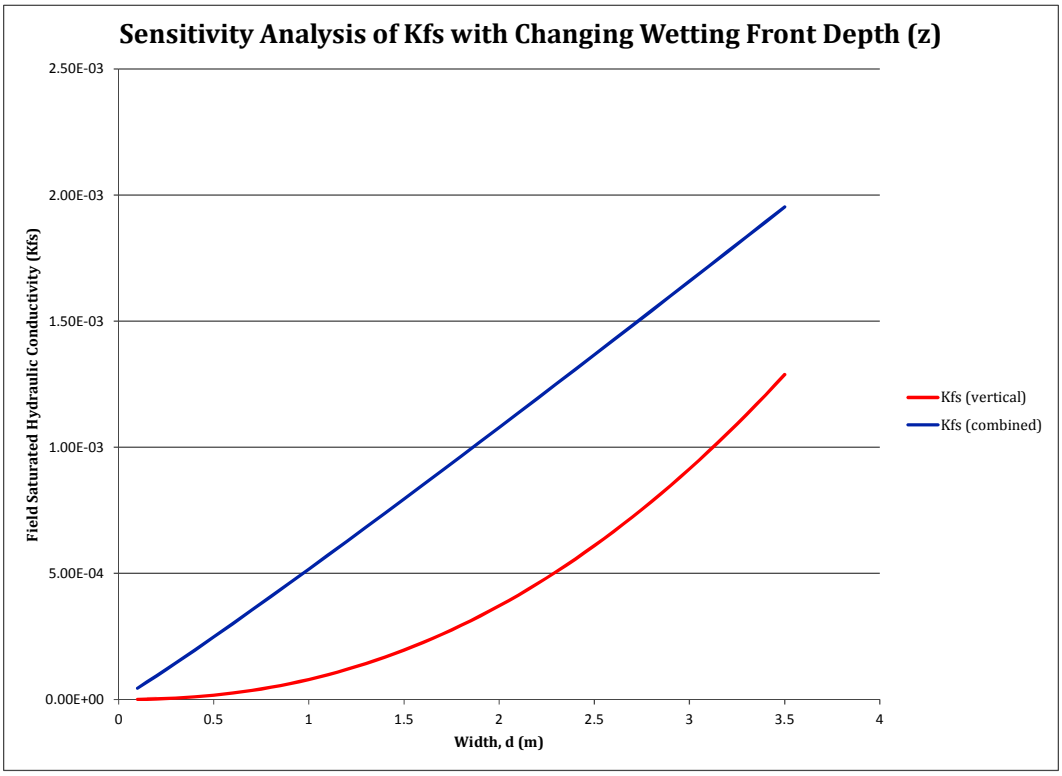

Figure A3: Sensitivity analysis graph of K_{fs} with changing wetting front depth (z) for the Schwartzman and Zur (1987) vertical and combined equations. The range in changing depth values and constant values of width, volume, and outflow discharge rates are detailed in Table A2.

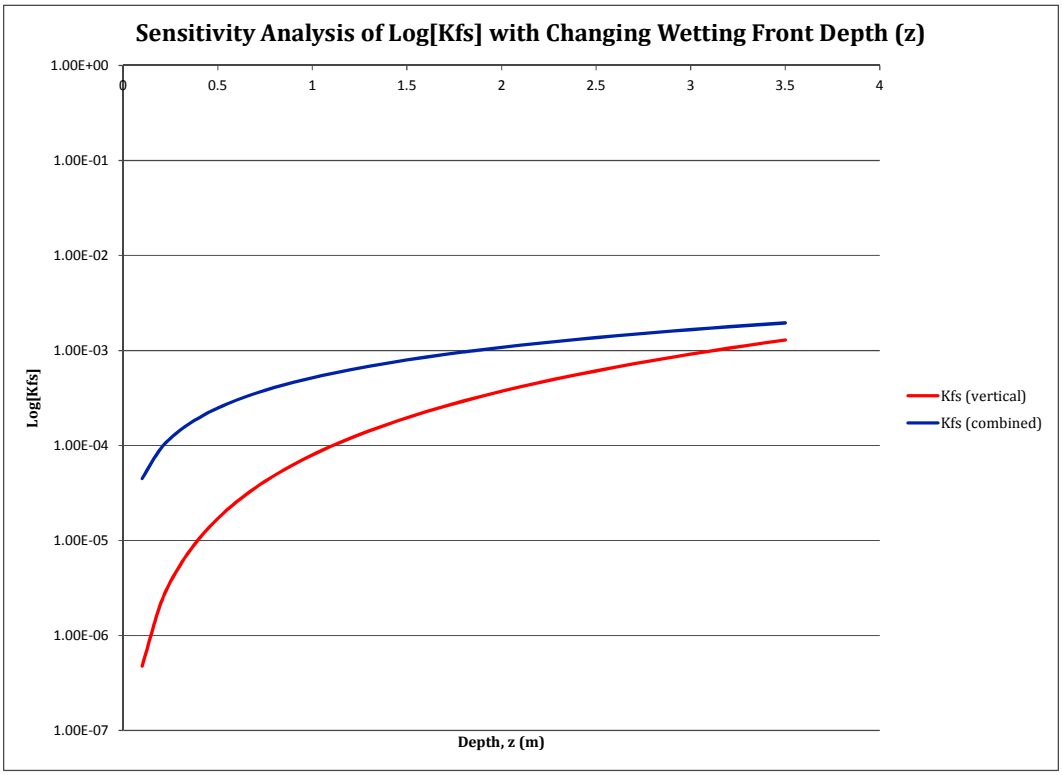

Figure A4: Sensitivity analysis graph of Log [K_{fs}] with changing wetting front depth (z) for the Schwartzman and Zur (1987) vertical and combined equations. The range in changing depth values and constant values of width, volume, and outflow discharge rates are detailed in Table A2.

SENSITIVITY ANALYSIS OF K_{FS} WITH CHANGING VOLUME (V)					
d (m)	z (m)	q (m^3/s)	V (m^3)	K_{fs} vertical (m/s)	K_{fs} horizontal (m/s)
0.5	0.5	2.73E-05	0.01	4.65E-04	1.41E-04
0.5	0.5	2.73E-05	0.02	1.76E-04	3.45E-04
0.5	0.5	2.73E-05	0.03	9.99E-05	5.83E-04
0.5	0.5	2.73E-05	0.04	6.68E-05	8.47E-04
0.5	0.5	2.73E-05	0.05	4.89E-05	1.13E-03
0.5	0.5	2.73E-05	0.06	3.79E-05	1.43E-03
0.5	0.5	2.73E-05	0.07	3.05E-05	1.75E-03
0.5	0.5	2.73E-05	0.08	2.53E-05	2.08E-03
0.5	0.5	2.73E-05	0.09	2.15E-05	2.42E-03
0.5	0.5	2.73E-05	0.1	1.85E-05	2.77E-03
0.5	0.5	2.73E-05	0.11	1.62E-05	3.13E-03
0.5	0.5	2.73E-05	0.12	1.43E-05	3.51E-03
0.5	0.5	2.73E-05	0.13	1.28E-05	3.89E-03
0.5	0.5	2.73E-05	0.14	1.16E-05	4.28E-03
0.5	0.5	2.73E-05	0.15	1.05E-05	4.68E-03
0.5	0.5	2.73E-05	0.16	9.59E-06	5.09E-03
0.5	0.5	2.73E-05	0.17	8.81E-06	5.51E-03
0.5	0.5	2.73E-05	0.18	8.13E-06	5.93E-03
0.5	0.5	2.73E-05	0.19	7.54E-06	6.36E-03
0.5	0.5	2.73E-05	0.2	7.02E-06	6.80E-03
0.5	0.5	2.73E-05	0.21	6.55E-06	7.24E-03
0.5	0.5	2.73E-05	0.22	6.14E-06	7.69E-03
0.5	0.5	2.73E-05	0.23	5.77E-06	8.14E-03
0.5	0.5	2.73E-05	0.24	5.44E-06	8.60E-03
0.5	0.5	2.73E-05	0.25	5.13E-06	9.07E-03
0.5	0.5	2.73E-05	0.26	4.86E-06	9.54E-03
0.5	0.5	2.73E-05	0.27	4.61E-06	1.00E-02
0.5	0.5	2.73E-05	0.28	4.38E-06	1.05E-02
0.5	0.5	2.73E-05	0.29	4.17E-06	1.10E-02
0.5	0.5	2.73E-05	0.3	3.98E-06	1.15E-02
0.5	0.5	2.73E-05	0.31	3.80E-06	1.20E-02
0.5	0.5	2.73E-05	0.32	3.63E-06	1.25E-02
0.5	0.5	2.73E-05	0.33	3.48E-06	1.30E-02
0.5	0.5	2.73E-05	0.34	3.34E-06	1.35E-02
0.5	0.5	2.73E-05	0.35	3.21E-06	1.40E-02

Table A3: Sensitivity analysis table of K_{fs} with changing cumulative infiltration volume (V) of the Schwartzman and Zur (1987) vertical, horizontal, and combined equations.

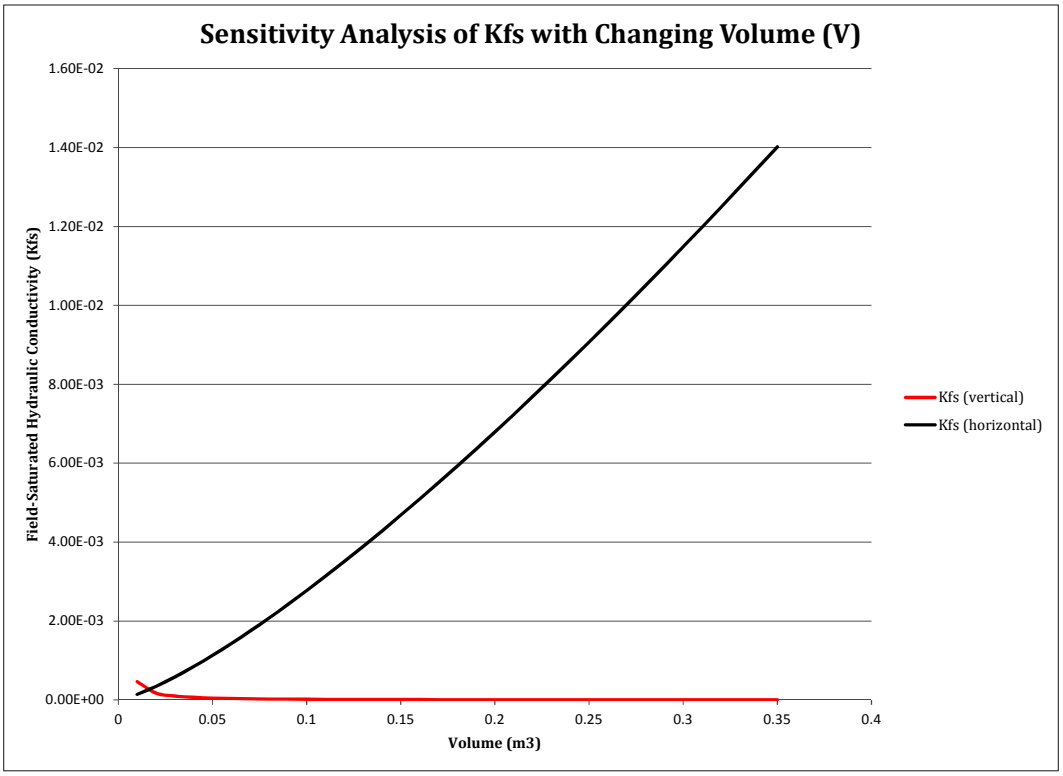

Figure A5: Sensitivity analysis graph of K_{fs} with changing cumulative infiltration volume (V) for the Schwartzman and Zur (1987) vertical and horizontal equations.

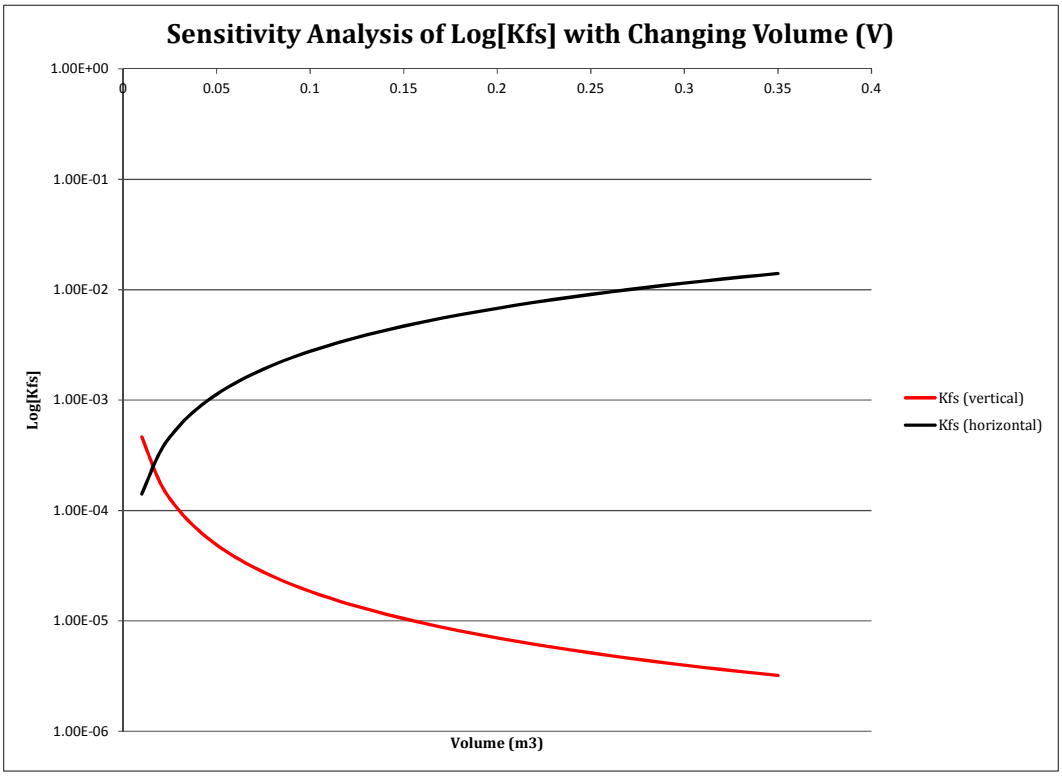

Figure A6: Sensitivity analysis graph of Log [K_{fs}] with changing cumulative infiltration volume (V) for the Schwartzman and Zur (1987) vertical and horizontal equations.

SENSITIVITY ANALYSIS OF K_{FS} WITH CHANGING OUTFLOW DISCHARGE (q)						
d (m)	z (m)	q (m3/s)	V (m^3)	K_{fs} vertical (m/s)	K_{fs} horizontal (m/s)	K_{fs} combined (m/s)
0.5	0.5	9.10E-07	0.106	5.69E-07	9.96E-05	8.27E-06
0.5	0.5	1.82E-06	0.106	1.14E-06	1.99E-04	1.65E-05
0.5	0.5	2.73E-06	0.106	1.71E-06	2.99E-04	2.48E-05
0.5	0.5	3.64E-06	0.106	2.28E-06	3.98E-04	3.31E-05
0.5	0.5	4.55E-06	0.106	2.84E-06	4.98E-04	4.13E-05
0.5	0.5	5.46E-06	0.106	3.41E-06	5.98E-04	4.96E-05
0.5	0.5	6.37E-06	0.106	3.98E-06	6.97E-04	5.79E-05
0.5	0.5	7.28E-06	0.106	4.55E-06	7.97E-04	6.61E-05
0.5	0.5	8.19E-06	0.106	5.12E-06	8.96E-04	7.44E-05
0.5	0.5	9.10E-06	0.106	5.69E-06	9.96E-04	8.27E-05
0.5	0.5	1.00E-05	0.106	6.26E-06	1.10E-03	9.09E-05
0.5	0.5	1.09E-05	0.106	6.83E-06	1.20E-03	9.92E-05
0.5	0.5	1.18E-05	0.106	7.40E-06	1.29E-03	1.07E-04
0.5	0.5	1.27E-05	0.106	7.96E-06	1.39E-03	1.16E-04
0.5	0.5	1.37E-05	0.106	8.53E-06	1.49E-03	1.24E-04
0.5	0.5	1.46E-05	0.106	9.10E-06	1.59E-03	1.32E-04
0.5	0.5	1.55E-05	0.106	9.67E-06	1.69E-03	1.41E-04
0.5	0.5	1.64E-05	0.106	1.02E-05	1.79E-03	1.49E-04
0.5	0.5	1.73E-05	0.106	1.08E-05	1.89E-03	1.57E-04
0.5	0.5	1.82E-05	0.106	1.14E-05	1.99E-03	1.65E-04
0.5	0.5	1.91E-05	0.106	1.19E-05	2.09E-03	1.74E-04
0.5	0.5	2.00E-05	0.106	1.25E-05	2.19E-03	1.82E-04
0.5	0.5	2.09E-05	0.106	1.31E-05	2.29E-03	1.90E-04
0.5	0.5	2.18E-05	0.106	1.37E-05	2.39E-03	1.98E-04
0.5	0.5	2.28E-05	0.106	1.42E-05	2.49E-03	2.07E-04
0.5	0.5	2.37E-05	0.106	1.48E-05	2.59E-03	2.15E-04
0.5	0.5	2.46E-05	0.106	1.54E-05	2.69E-03	2.23E-04
0.5	0.5	2.55E-05	0.106	1.59E-05	2.79E-03	2.31E-04
0.5	0.5	2.64E-05	0.106	1.65E-05	2.89E-03	2.40E-04
0.5	0.5	2.73E-05	0.106	1.71E-05	2.99E-03	2.48E-04
0.5	0.5	2.82E-05	0.106	1.76E-05	3.09E-03	2.56E-04
0.5	0.5	2.91E-05	0.106	1.82E-05	3.19E-03	2.65E-04
0.5	0.5	3.00E-05	0.106	1.88E-05	3.29E-03	2.73E-04
0.5	0.5	3.09E-05	0.106	1.93E-05	3.39E-03	2.81E-04
0.5	0.5	3.19E-05	0.106	1.99E-05	3.49E-03	2.89E-04

Table A4: Sensitivity analysis table of K_{fs} with changing outflow discharge (q) of the Schwartzman and Zur (1987) vertical, horizontal, and combined equations.

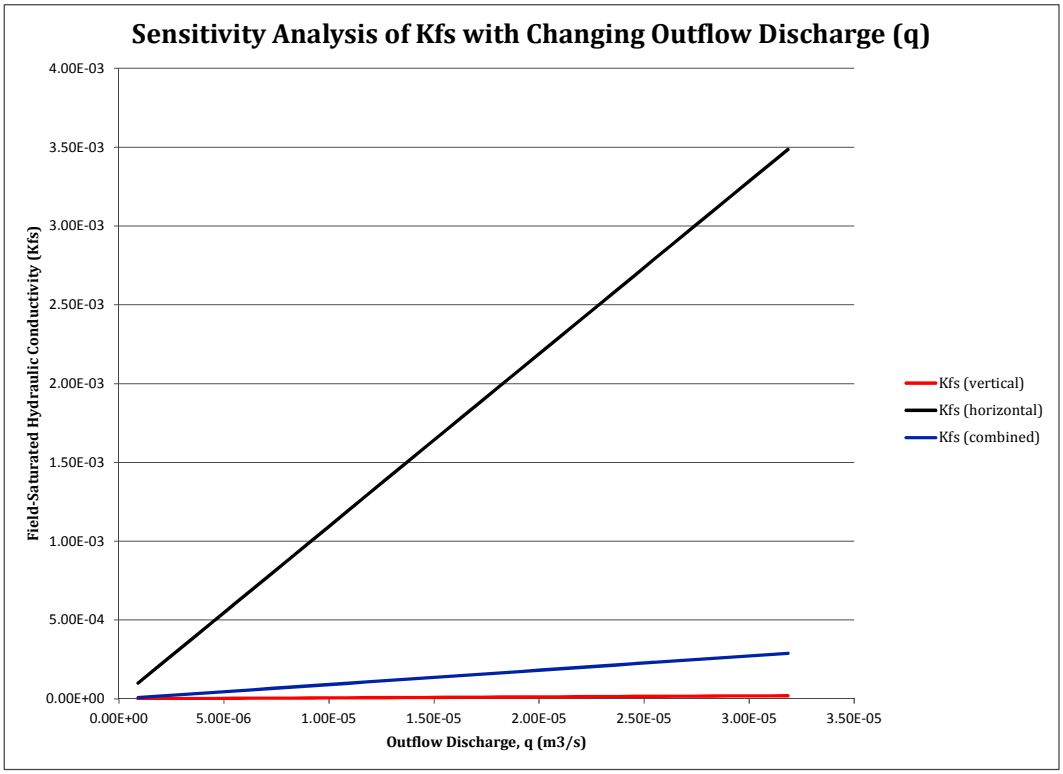

Figure A7: Sensitivity analysis graph of K_{fs} with changing outflow discharge (q) for the Schwartzman and Zur (1987) vertical, horizontal, and combined equations. The range in changing outflow discharge rates and constant values of width, depth, and volume are detailed in Table A4.

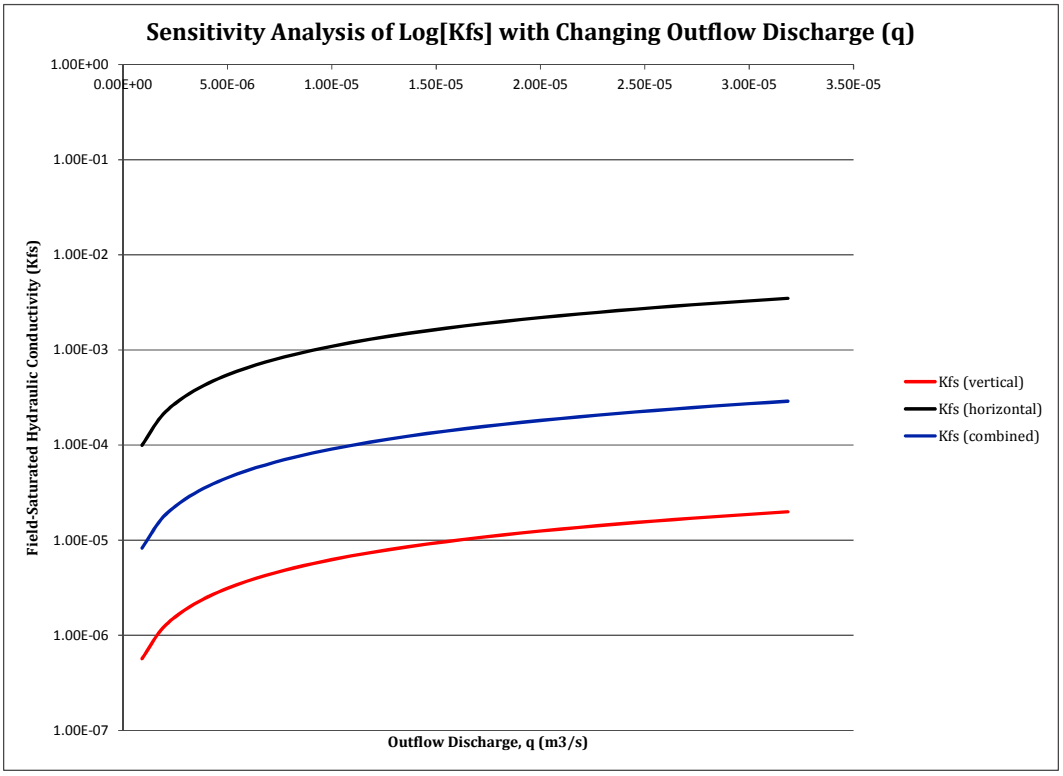

Figure A8: Sensitivity analysis graph of Log [K_{fs}] with changing outflow discharge (q) for the Schwartzman and Zur (1987) vertical, horizontal, and combined equations.

VITA

Rachel E. Storniolo was born in Philadelphia, PA and raised in North Atlanta, GA by her parents Denise A. Hannahan and Frank R. Storniolo. She graduated from Marist School in Atlanta in 2005 and began college at Appalachian State University. At Appalachian State University she found her passion for Geology, and graduated with a Bachelor of Science in Geology, minoring in Mathematics and Physics in the summer of 2010. After graduation, she immediately moved to Knoxville, TN to pursue a MS degree under Dr. Gregory S. Baker, researching near-surface geophysics and hydrology. After graduation from The University of Tennessee, she is moving to Houston, TX to begin a career in the Oil and Gas Industry.